

Copyright

by

Kwon Taek Oh

2012

**The Thesis Committee for Kwon Taek Oh  
Certifies that this is the approved version of the following thesis:**

**Velocity modeling to determine pore aspect ratios of the Haynesville  
Shale**

**APPROVED BY  
SUPERVISING COMMITTEE:**

**Supervisor:**

---

Kyle Spikes

---

Robert Tatham

---

Mrinal Sen

**Velocity modeling to determine pore aspect ratios of the Haynesville  
Shale**

**by**

**Kwon Taek Oh, B.E.**

**Thesis**

Presented to the Faculty of the Graduate School of

The University of Texas at Austin

in Partial Fulfillment

of the Requirements

for the Degree of

**Master of Science in Geological Sciences**

**The University of Texas at Austin**

**May 2012**

## **Dedication**

I dedicate this to my family, Jin A Jeon and Kyoung Yeon Oh, my friends, the scientific society, and, last but certainly not least, my parents and the Holy God.

## **Acknowledgements**

This work has benefited from my interaction with a large number of people that I wish to thank. First of all, I am greatly indebted to my advisor Dr. Kyle Spikes for his guidance and support during my graduate studies. I had lots of difficulty in studying geophysics at first as a chemical engineering background student. His dedication to my education and research as his student has made this work possible and he has guided me along the path that led to where I am today with his open mind. I would like to acknowledge the guidance I received from my committee members: Dr. Robert Tatham and Dr. Mrinal Sen. They have reviewed my thesis and suggested developmental ideas.

Furthermore, I would like to express my gratitude to my friends, Russell Carter and Meijuan Jiang who have been my officemates for two years since I entered the school. I am really thankful for all their discussions and suggestions that improved my understanding of “Exploration Geophysics” and their excellent mathematics and Matlab skills, but more importantly I really appreciated their close friendship. I am also very thankful to fellow students: Sharif Morshed, Alexander Lamb, Kumar Das, Yang Wang, Yang Xue, Yu Xia, Terence Campbell, Qi Ren, Sarah Coyle, Lauren Becker, Zeyu Zhao, Corey Joy, Yi Tao, and Mohammed Alhussain in Exploration Geophysics group. It was a really fun time to have studied with yours at the University of Texas at Austin.

Lastly, I would like to thank Dr. Ray Barrett at BP Inc. for providing the in-situ data, and also thank Dr. Ursula Hammes at The Bureau of Economic Geology for providing core analysis data of the Haynesville Shale. The Jackson School of Geosciences and the Exploration and Development Geophysics Education and Research (EDGER) Forum at The University of Texas at Austin supported this work.

## **Abstract**

# **Velocity modeling to determine pore aspect ratios of the Haynesville Shale**

Kwon Taek Oh, MSGeoSci

The University of Texas at Austin, 2012

Supervisor: Kyle Spikes

Worldwide interest in gas production from shale formations has rapidly increased in recent years, mostly by the successful development of gas shales in North America. The Haynesville Shale is a productive gas shale resource play located in Texas and Louisiana. It produces primarily through enhanced exposure to the reservoir and improved permeability resulting from horizontal drilling and hydraulic fracturing. Accordingly, it is important to estimate the reservoir properties that influence the elastic and geomechanical properties from seismic data.

This thesis estimates pore shapes, which affect the transport, elastic, and geomechanical properties, from wellbore seismic velocity in the Haynesville Shale. The approach for this work is to compare computed velocities from an appropriate rock physics model to measured velocities from well log data. In particular, the self-consistent approximation was used to calculate the model-based velocities. The Backus average was used to upscale the high-frequency well log data to the low-frequency seismic scale. Comparisons of calculated velocities from the self-consistent model to upscaled Backus-

averaged velocities (at 20 Hz and 50 Hz) with a convergence of 0.5% made it possible to estimate pore aspect ratios as a function of depth.

The first of two primary foci of this approach was to estimate pore shapes when a single fluid was emplaced in all the pores. This allowed for understanding pore shapes while minimizing the effects of pore fluids. Secondly, the effects of pore fluid properties were studied by comparing velocities for both patchy and uniform fluid saturation. These correspond to heterogeneous and homogeneous fluid mixing, respectively. Implementation of these fluid mixtures was to model them directly within the self-consistent approximation and by modeling dry-rock velocities, followed by standard Gassmann fluid substitution. P-wave velocities calculated by the self-consistent model for patchy saturation cases had larger values than those from Gassmann fluid substitution, but S-wave velocities were very similar.

Pore aspect ratios for variable fluid properties were also calculated by both the self-consistent model and Gassmann fluid substitution. Pore aspect ratios determined for the patchy saturation cases were the smallest, and those for the uniform saturation cases were the largest. Pore aspect ratios calculated by Gassmann fluid substitution were larger because the velocity is inversely related to the aspect ratio in this particular modeling procedure. Estimates of pore aspect ratios for uniform saturation were 0.051 to 0.319 with the average of 0.171 from the velocity modeling using the self-consistent model. For patchy saturation, the aspect ratios were 0.035 to 0.296 with a mean of 0.145. These estimated pore aspect ratios from the patchy saturation case within the self-consistent model are considered the most reasonable set of values I determined. This is because the most likely in-situ fluid distribution is heterogeneous due to the extremely low permeability of the Haynesville Shale. Estimated pore aspect ratios using this modeling help us to understand elastic properties of the Haynesville Shale. In addition, this may

help to find zones that correspond to optimal locations for fracturing the shale while considering brittleness and in-situ stress of the formation.

## Table of Contents

List of Tables .....	xii
List of Figures .....	xv
Chapter 1: Introduction .....	1
1.1 Motivation.....	1
1.2 Outline and Content.....	3
1.3 Geological Background .....	4
1.4 Micro-structural Image .....	7
1.5 Well data .....	8
1.6 References.....	15
Chapter 2: Theory .....	17
2.1 Effective medium theory.....	17
2.2 Self-consistent model.....	24
2.3 Fluid mixtures and saturation scales .....	32
2.4 Gassmann fluid substitution.....	36
2.5 Closing stress .....	39
2.6 summary.....	42
2.7 References.....	42
Chapter 3: Modeling methodology .....	44
3.1 Input data .....	44
3.1.1 Elastic property of composition .....	44
3.1.2 Composition data .....	45
3.1.3 Aspect ratio for mineral grains and pores .....	49
3.2 Velocity modeling for Pore shape estimation.....	51
3.3 References.....	53
Chapter 4: Modeling Results and Discussion .....	54
4.1 Pore shape estimates for fixed fluid properties.....	54
4.2 The effects of fluid property changes to velocities.....	64

4.2.1	Water saturation .....	64
4.2.2	Patchy and uniform saturation .....	66
4.2.3	Velocity comparison by SCM for various types of fluid distributions .....	68
4.2.4	Velocity comparison by Gassmann substitution for various types of fluids .....	73
4.2.5	Velocity Comparison between the self-consistent model and Gassmann fluid substitution.....	77
4.2.6	Discussion .....	81
4.3	Results of determined pore aspect ratios for various types of fluid distributions.....	82
4.3.1	Pore Aspect ratios by SCM for various types of fluid distributions .....	82
4.3.1.1	Results of XRD data .....	82
4.3.1.2	Results of interpolated data.....	83
4.3.1.3	Comparison of results for the self-consistent model.....	86
4.3.2	Pore aspect ratios by Gassmann substitution for various types of fluid distributions .....	92
4.3.2.1	Modeling procedure .....	92
4.3.2.2	Results of XRD data .....	93
4.3.2.3	Results of interpolated data.....	94
4.3.2.4	Comparison of results for Gassmann Substitution.....	96
4.3.3	Comparison of pore aspect ratios between the self-consistent model and Gassmann fluid substitution.....	100
4.3.4	Discussion .....	104
4.3.4.1	Determination of pore aspect ratios for pore fluid distributions.....	104
4.3.4.2	Difference of velocity modeling for P-wave velocities and pore aspect ratios.....	105
4.3.4.3	Relationship between parameters .....	106
4.4	References.....	111
Chapter 5:	Conclusion.....	112
5.1	summary and conclusions .....	112

5.2 limitations .....	114
5.3 possible future works .....	115
References.....	117
Vita .....	120

## List of Tables

Table 1.1: Well data and the range of reservoir properties of the well.....	15
Table 2.1: Average fractional (%) composition data of the Haynesville Shale.....	29
Table 3.1: Elastic properties of minerals and fluids used in this modeling. (Simmons and Birth, 1963; Carmichael, 1989; Mavko et al., 2009). .....	44
Table 3.2: Comparison of fractional (%) composition data between the Haynesville and the Bossier Shale, TX (Courtesy of Hammes, 2010).....	46
Table 3.3: Aspect ratios of minerals used in the modeling. ....	49
Table 4.1: The maximum, minimum and mean values of estimated pore aspect ratios and calculated effective elastic moduli for 20 Hz for the interpolated composition data. From the left, estimated pore aspect ratios, P-wave and S-wave velocities calculated from the Backus average, bulk moduli, shear moduli, P-wave and S-wave velocities calculated from the self-consistent model, differences of P-wave and S-wave velocities between the Backus average and the self-consistent model, respectively. ....	54
Table 4.2: The maximum, minimum and mean values of estimated pore aspect ratios and calculated effective elastic moduli for 50 Hz for the interpolated data. ....	54
Table 4.3: Calculated maximum, minimum and mean values of bulk moduli and densities of fluids for fixed fluid, the patchy and uniform saturation.	67
Table 4.4: Bulk and shear moduli, P-wave and S-wave velocities calculated by the self-consistent model for dry pores, fixed fluids, the patchy and uniform saturation.....	70

Table 4.5: Bulk and shear moduli, P-wave and S-wave velocities calculated using by Gassmann fluid substitution for the patchy and uniform saturation cases. ....	75
Table 4.6: Comparison of bulk and shear moduli, P-wave and S-wave velocities calculated by both the self-consistent model and Gassmann substitution for dry pores, fixed fluids, the patchy and uniform saturation.....	78
Table 4.7: The maximum, minimum and mean values of estimated pore aspect ratios and calculated effective elastic moduli of the XRD data for dry pores, patchy and uniform saturation by the velocity modeling for 50 Hz for the Haynesville shale. From the left, estimated pore aspect ratios, P-wave and S-wave velocities calculated from the Backus average, bulk and shear moduli, P-wave and S-wave velocities calculated from the self-consistent model, differences of P-wave and S-wave velocities between the Backus average and the self-consistent model, respectively. ....	83
Table 4.8: The maximum, minimum and mean values of estimated pore aspect ratios and calculated effective elastic moduli of the interpolated data for dry pores, patchy and uniform saturation by the velocity modeling for 50 Hz for the Haynesville shale. From the left, with the same data as shown in Table 4.7. ....	84
Table 4.9: Comparisons of the maximum, minimum and mean values of estimated pore aspect ratios of (a) the XRD data (b) the interpolated data for dry pores, patchy and uniform saturation by velocity modeling (for 50 Hz) for the Haynesville shale ( $Asp_{patchy} < Asp_{dry} < Asp_{uniform}$ ).86	

Table 4.10: The maximum, minimum and mean values of estimated pore aspect ratios and calculated effective elastic moduli of the XRD data for patchy and uniform saturation by Gassmann-derived velocities for 50 Hz for the Haynesville shale. From the left, estimated pore aspect ratios, P-wave and S-wave velocities calculated from the Backus average, bulk and shear moduli, P-wave and S-wave velocities calculated from the self-consistent model, differences of P-wave and S-wave velocities between the Backus average and the self-consistent model, respectively. ....	93
Table 4.11: The maximum, minimum and mean values of estimated pore aspect ratios and calculated effective elastic moduli of the interpolated data for patchy and uniform saturation by Gassmann-derived velocities for 50 Hz. From the left, with the same data as shown in Table 4.10. ....	94
Table 4.12: Comparisons of the maximum, minimum and mean values of estimated pore aspect ratios from the Gassmann-derived velocities of (a) the XRD data (b) the interpolated data for dry pores, patchy and uniform saturation by velocity modeling (for 50 Hz) ( $Asp_{patchy} < Asp_{dry} < Asp_{uniform}$ ). ....	96
Table 4.13: Comparison of estimated pore aspect ratios of (a) the XRD data (b) the interpolated data for dry pores, the patchy and uniform saturation calculated by the self-consistent model and Gassmann fluid substitution ( $Patchy(SCM) < Patchy(Gassmann) < Dry\ pores < Uniform(SCM) < Uniform(Gassmann)$ ). ....	100

## List of Figures

- Figure 1.1: Stratigraphic section of East Texas (Goldhammer and Johnson, 2001). Hammes et al. (2009) modified ages and composite sea level. The Haynesville Shale is organic- and carbonate-rich shale formation deposited during a transgressive stage. ....5
- Figure 1.2: Nano-scale image of the Haynesville Shale (Modified from Curtis et al., 2010). ....7
- Figure 1.3: SEM image showing different pore types of the Haynesville including organic (O), interparticle (ip), and moldic (M) micropores and nanopores (Hammes et al., 2011). ....8
- Figure 1.4: Well log data. From the left, gamma ray (API), density (g/cc), density porosity (fraction), P-wave velocity (km/s), S-wave velocity (km/s), and Vp/Vs ratio are plotted versus depth. The Haynesville Shale in this well is colored by red at the bottom of the figure. The vertical axis is artificial depth. Depth is disguised to maintain confidentiality of the well location. ....10
- Figure 1.5: Well log data from the Haynesville Shale, showing the Haynesville (red) portions of the curves from Figure 1.4. ....10
- Figure 1.6: Well log data for the middle part of the Haynesville Shale. From the left, volume of clay, water saturation, porosity, and P-impedance versus depth. This part shows good relationships among the well data curves due to small changes of data. ....12

Figure 1.7: Cross plots of the Haynesville Shale. (a)  $V_p$  versus porosity (b)  $V_s$  versus porosity (c)  $V_p$  versus  $V_s$  (d) P-impedance versus porosity. Data points are colored by gamma ray where high GR indicates high clay content. ....13

Figure 1.8: Cross plots of the Haynesville Shale. Water saturation and volume of clay versus (a) porosity and (b) density.....14

Figure 2.1: Concept of the moving Backus average in case of 50 Hz seismic scale.20

Figure 2.2: Moving Backus average for 20 Hz (red) and 50 Hz (green). From the left to right, moving Backus averages for P-wave velocity (km/s) and S-wave velocity (km/s) are plotted versus depth.....21

Figure 2.3: Moving arithmetic average for 20 Hz (red) and 50 Hz (green). From the left to right, moving arithmetic averages for density (g/cc), and porosity (fraction) are plotted versus depth. ....22

Figure 2.4: Moving arithmetic average for 20 Hz (red) and 50 Hz (green). From the left to right, moving arithmetic averages for P impedance (g/cc\*km/s), S impedance (g/cc\*km/s) and  $V_p/V_s$  are plotted versus depth.....23

Figure 2.5: Schematic diagram of the self-consistent model. The square represents an infinite background matrix and the circle does a rock. Blue and black ellipses represent mineral grain inclusions and pore inclusions in the square, respectively (Courtesy of Jiang and Spikes, 2011). ....25

Figure 2.6: Cross plots of (a)  $V_p$  and (b)  $V_s$  versus porosity data overlain with the self-consistent modeling results for the Haynesville Shale. Data points are colored by gamma ray values. The colored lines are the results of the self-consistent model with average composition from the XRD data and normally distributed pore aspect ratio (mean 0.145, standard deviation 0.01). These modeled lines fit well to the measured data reasonably (Bulk modulus: 1 GPa and density: 0.8 g/cc for fluids). .....30

Figure 2.7: Cross plots of (a) bulk modulus ( $K$ ) and (b) shear modulus ( $\mu$ ) versus porosity data overlain with the self-consistent modeling results for the Haynesville Shale. Data points are colored by gamma ray values. The blue lines are from the self-consistent model using same input values in Figure 2.6. These blue lines fit well to the measured data and cross almost the center of the data cluster.....31

Figure 2.8:  $V_p$  and  $V_s$  versus water saturation ( $S_w$ ) measured during a continuous imbibition/drainage experiment (Berryman et al., 1999).....33

Figure 2.9: Schematic diagram for patchy saturation and uniform saturation. Upper figure is the patchy saturation at a coarse scale and bottom one explains the uniform saturation at a fine scale between water and oil (Mavko and Mukerji, 1998). Coarse-scale saturation increases the stiffness and velocity of the rock. However, fine-scale saturation is softer and low velocity than the coarse-scale saturation.....34

Figure 2.10: The discrepancy (differences between the measured and calculated bulk moduli) of Gassmann fluid substitution. The Gassmann's relations are for low frequencies. As a result, there are differences between calculated velocities of saturated rocks using the low frequency Gassmann equations and velocities measured at high frequency (Han et al., 1986).  
.....37

Figure 2.11: Velocity dispersion and frequency. ....38

Figure 2.12: The closing stress of a single isolated pore versus various pore aspect ratios. When pore aspect ratio is 1, the closing stress of a single isolated pore with quartz matrix is about 55 GPa. The closing stress with clay matrix is less than 30 GPa, and the closing stress for an average composition of the Haynesville Shale is almost the same pure quartz.40

Figure 2.13: Zoom of red zone in Figure 2.12. The closing stress of a single isolated pore versus various pore aspect ratios. At the top and the bottom of the Haynesville Shale, the confining pressure is 85 MPa and 90 MPa, respectively. ....40

Figure 3.1: XRD composition data for the Haynesville and Bossier Shale, TX. The red line is the limit of two shale formations. ....45

Figure 3.2: Histograms of mineral percentages for the Haynesville and Bossier Shale, TX. (a) the Bossier Shale (b) the Haynesville Shale. Vertical and horizontal axes are number of samples and fractional composition (%), respectively. ....47

Figure 3.3: Volume of total clay vs. volume of quartz for the Haynesville and Bossier Shale. Data points are colored by depths. ....48

Figure 3.4: Flow chart of velocity modeling to determine the pore aspect ratio of specific depth in the Haynesville Shale. This modeling was performed for the entire depth range at both 20 Hz and 50 Hz. At first, bulk modulus (1 GPa) and density (0.8 g/cc) values for pore fluids were fixed. Partial saturation cases are dealt with in later sections.....52

Figure 4.1: Estimated pore aspect ratios for 20 Hz. From the top to bottom, original XRD data, the 1<sup>st</sup> interpolated data, and the 2<sup>nd</sup> interpolated data, respectively. In each Figure, from the left, pore aspect ratios, effective bulk and shear moduli (GPa), effective P-wave and S-wave velocities (km/s) calculated by the self-consistent model.....56

Figure 4.2: Estimated pore aspect ratios for 50 Hz. From the top to bottom, original XRD data, the 1<sup>st</sup> interpolated data, and the 2<sup>nd</sup> interpolated data, respectively. In each Figure, from the left, with the same data set as in Figure 4.1.....57

Figure 4.3: The histograms of estimated pore aspect ratios for 20 Hz and 50 Hz. From the top to bottom, original XRD data, the 1<sup>st</sup> interpolated data, and the 2<sup>nd</sup> interpolated data, respectively. The left one is for 20 Hz and the right one is for 50 Hz. In each frame, from the left, pore aspect ratios, differences of P-wave and S-wave velocities between the Backus average and the self-consistent model. ....59

Figure 4.4: The Q-Q plots between original XRD data and interpolated data from the velocity modeling for 50 Hz. Left figure is the Q-Q plot between original XRD and 1st interpolated data, and right one is between original XRD and 2nd interpolated data. From top to bottom in each column, the Q-Q plots are for pore aspect ratios, differences of P-wave and S-wave velocities between the self-consistent model and the Backus average are plotted. ....61

Figure 4.5: Comparisons of estimated pore aspect ratios for 20 Hz and 50 Hz. The upper figure is calculated for 20 Hz and the bottom one is for 50 Hz. In each figure, from the left, pore aspect ratios calculated from original XRD data, 1<sup>st</sup> interpolated data, and 2<sup>nd</sup> interpolated data, respectively. ....63

Figure 4.6: Well log data of the whole range of the well. From the left, density porosity (fraction), water saturation (fraction), and volume of illite (fraction) are plotted versus depth. Haynesville Shale is below red arrow in this Figure. There is a large drop of volume clay content at the top of the Haynesville Shale (6,100 ft.) relative to the overlying formation.65

Figure 4.7: Bulk moduli ( $K_{fl}$ ) and densities ( $\rho_{fl}$ ) of fluids for patchy saturation, uniform saturation and fixed fluid values ( $K_{fl}=1$  GPa,  $\rho_{fl}=0.8$  g/cc for fluids) versus depth. Blue is for patchy saturation. Green is for uniform saturation. The red line is for the fixed value of fluids for the velocity modeling. ....66

Figure 4.8: Graphs of (a) bulk moduli, (b) shear moduli (c) P-wave velocities, and (d) S-wave velocities for dry pores, the patchy and uniform saturation calculated by the self-consistent model for the Haynesville shale. Shear moduli and S-wave velocities for saturated cases are different from those of dry cases because the self-consistent model is a high-frequency model. Values between the patchy and uniform saturation are also different due to the effect of partial saturation in both moduli and velocities. Each case corresponds to the same normal distribution of pore aspect ratios.....69

Figure 4.9: Histograms of P-wave and S- wave velocities for dry pores, fixed fluid, the patchy and uniform saturation calculated by the self-consistent model for the Haynesville shale.....72

Figure 4.10: Graphs of (a) P-wave velocities and (b) S- wave velocities for dry pores, the patchy and uniform saturation calculated by Gassmann fluid substitution for the Haynesville Shale. As expected, S-wave velocities for the patchy and uniform saturation cases are the same in (b).....74

Figure 4.11: Histograms of P-wave and S- wave velocities for dry pores and fixed fluid calculated by the self-consistent model, the patchy and uniform saturation calculated by Gassmann fluid substitution for the Haynesville shale. ....76

Figure 4.12: Comparison of P-wave velocities for dry pores, the patchy and uniform saturation calculated by the self-consistent model and from Gassmann fluid substitution for the Haynesville shale. Yellow line is (a) the measured data from the well log and (b) the upscaled data from the Backus average. Patchy saturation values of P-wave velocities from the self-consistent model best represent the measured data at the upscaled scale.....78

Figure 4.13: Comparison of S-wave velocities for dry pores, the patchy and uniform saturation calculated by the self-consistent model and from Gassmann fluid substitution for the Haynesville shale. Yellow line is (a) the measured data from the well log and (b) the upscaled data from the Backus average. Patchy saturation values of S-wave velocities from the self-consistent model also best represent the measured data at the upscaled scale. S-wave velocities for the patchy and uniform saturation calculated by Gassmann fluid substitution are same. ....79

Figure 4.14: Comparison of histograms of P-wave and S-wave velocities for dry pores, fixed fluid, the patchy and uniform saturation calculated by the self-consistent model and Gassmann fluid substitution for the Haynesville shale. ....80

Figure 4.15: Comparison of histograms of estimated pore aspect ratios of (a) the XRD data (b) the interpolated data for dry pores, fixed fluids, the patchy and uniform saturation by velocity modeling (for 50 Hz) for the Haynesville Shale.....85

Figure 4.16: Estimated pore aspect ratios for (a) the XRD data (b) the interpolated data for dry pores, the patchy and uniform saturation cases by using the self-consistent model and the Backus average (50 Hz) for the Haynesville Shale.....87

Figure 4.17: Estimated pore aspect ratios, effective bulk and shear moduli, effective P-wave and S-wave velocities calculated by the self-consistent model of (a) the XRD data and (b) the interpolated data for dry pores by velocity modeling (for 50 Hz). .....89

Figure 4.18: Estimated pore aspect ratios, effective bulk and shear moduli, effective P-wave and S-wave velocities calculated by the self-consistent model of (a) the XRD data and (b) the interpolated data for the uniform saturation by velocity modeling (for 50 Hz).....90

Figure 4.19: Estimated pore aspect ratios, effective bulk and shear moduli, effective P-wave and S-wave velocities calculated by the self-consistent model of (a) the XRD data and (b) the interpolated data for the patchy saturation by velocity modeling (for 50 Hz).....91

Figure 4.20: Comparison of histograms of estimated pore aspect ratios from the Gassmann-derived velocities of (a) the XRD data (b) the interpolated data for dry pores (SCM), fixed fluids (SCM), the patchy and uniform saturation by velocity modeling (for 50 Hz) for the Haynesville Shale. ....95

Figure 4.21: Estimated pore aspect ratios from the Gassmann-derived velocities for (a) the XRD data (b) the interpolated data for dry pores (SCM), the patchy and uniform saturation (50 Hz) for the Haynesville Shale....97

Figure 4.22: Estimated pore aspect ratios, effective bulk and shear moduli, effective P-wave and S-wave velocities calculated by Gassmann fluid substitution of (a) the XRD data and (b) the interpolated data for the uniform saturation by velocity modeling (for 50 Hz).....98

Figure 4.23: Estimated pore aspect ratios, effective bulk and shear moduli, effective P-wave and S-wave velocities calculated by Gassmann fluid substitution of (a) the XRD data and (b) the interpolated data for the patchy saturation by velocity modeling (for 50 Hz).....99

Figure 4.24: Comparison of graphs of estimated pore aspect ratios of the XRD data for dry pores, the patchy and uniform saturation calculated by the self-consistent model and Gassmann fluid substitution for the Haynesville. ....101

Figure 4.25: Comparison of graphs of estimated pore aspect ratios of the interpolated data for dry pores, the patchy and uniform saturation calculated by the self-consistent model and Gassmann fluid substitution for the Haynesville. ....102

Figure 4.26: Comparison of histograms of estimated pore aspect ratios of (a) the XRD data and (b) the interpolated data for dry pores, the patchy and uniform saturation calculated by the self-consistent model and Gassmann fluid substitution for the Haynesville. ....103

Figure 4.27: The relationship between XRD composition data, determined pore aspect ratios of the patchy saturation (SCM), porosity, and measured P-wave velocities for the Haynesville.....107

- Figure 4.28: Cross plots of (a) measured P-wave velocities versus porosity colored by determined pore aspect ratios of the patchy saturation (SCM) and (b) trend line between P-wave velocity and porosity. There is an inverse relationship between P-wave velocities and porosity. ....108
- Figure 4.29: Cross plots of (a) determined pore aspect ratios of the patchy saturation (SCM) versus porosity colored by measured P-wave velocities and (b) trend line between aspect ratio and porosity. There is a direct relationship between pore aspect ratios and porosity. However, pore aspect ratio and porosity are inversely related to P-wave velocities.109
- Figure 4.30: Cross plots of (a) measured P-wave velocities versus determined pore aspect ratios of the patchy saturation (SCM) colored by porosity and (b) trend line between P-wave velocity and aspect ratio. There is an inverse relationship between pore aspect ratio and P-wave velocity. ....110

# Chapter 1: Introduction

## 1.1 MOTIVATION

The shapes of pores in sedimentary rocks affect both the transport and elastic properties of that rock (Sun, 2004; Avseth et al., 2010; Sondergeld et al., 2010). Typically, rounded pores at a constant porosity correspond to faster seismic P-wave velocity because the stiffness of the pores and overall rock stiffness increases. Counter to that, thin, elongated pores at the same porosity often lead to slower velocity. The pore shape is described by the pore aspect ratio, which is defined as the ratio between its shortest and longest axes. In addition, rounded pores would be much less likely to collapse or close from an external pressure than crack-like or penny-shaped pores that have low aspect ratios. Therefore, the relationship between the pore shape and the elastic properties is important to understand. The work here characterizes pore shapes in terms of velocities calculated from rock physics relationships for the Haynesville Shale. Ultimately, these should be related to the geomechanical properties, which is beyond the scope of the work presented here.

Techniques such as horizontal drilling and hydraulic fracturing make the production of shale gas feasible in spite of extremely low permeability, on the order of nanoDarcies. The purpose of the fracturing is to connect isolated pores and natural fractures with one another to enhance the permeability for economic production. The Haynesville Shale has penny-shaped or elongated grains compared with the other shale formations (Curtis et al., 2010). Due to the low aspect ratios of the pores in the Haynesville Shale, advanced techniques such as multistage hydraulic fracturing

technologies have a significant impact on gas production. Estimating pore aspect ratios can be helpful to find optimal locations for fracturing the shale to produce the gas shale economically while considering brittleness and in-situ stress of the formation.

According to Hammes et al. (2011), the average production rate per well is around 2 Bcfd (Billion cubic feet per day), and total reserves are estimated to be more than 100 Tcf (Trillion cubic feet). Although the Haynesville Shale currently produces a large amount of gas, a comprehensive rock physics study has not been performed to relate the reservoir properties to the elastic properties. It is a challenge to diagnose the characteristics of the Haynesville Shale only with well data. Unlike conventional sandstone and carbonate rocks, shale formations need quite different reservoir parameters such as pore shape and a description of a wide range of minerals and their proportionate quantities to explain observed variations in the elastic properties.

In this thesis, pore aspect ratios were determined by comparing measured velocities from well data to velocities computed from a rock physics model. Specifically, the self-consistent model (O'Connell and Budiansky, 1974; Berryman, 1980; Mavko et al., 2009) was used. This model incorporates grain and pore shapes and their elastic moduli into the formulation. In addition, this effective medium model is not limited to specific compositions and is also able to merge multiple mineralogical phases, as well as distributions of pore shapes (Mavko et al., 2009). This comparison was evaluated on well data upscaled to the bandwidth of surface seismic data (20 and 50 Hz) using the Backus average. The effective elastic moduli and velocities of the matrix were calculated using the self-consistent model with composition data and estimated pore aspect ratios. Comparing these calculated P-wave velocities to upscaled Backus-averaged velocities with a convergence of 0.5 % by trial and error made it possible to determine pore aspect ratios at each depth of the formation. The effects of pore-fluid properties were studied by

comparing velocities between the self-consistent model and Gassmann fluid substitution for both the patchy and uniform distributions of fluid saturations. Estimated pore aspect ratios for various fluid property types were also calculated by comparing modeled and measured velocities. By determining pore aspect ratios of the formation, we can better understand elastic properties of the Haynesville Shale. By performing this on up-scaled data, we can also estimate the ability to infer pore shape from surface seismic data. Knowing the pore shapes at the log and seismic scales make it possible to integrate well log measurements and surface seismic data and to help to understand the seismically derived reservoir characteristics of the Haynesville Shale.

## **1.2 OUTLINE AND CONTENT**

This thesis is organized as follows. I begin with background material for the Haynesville Shale in terms of the geologic and stratigraphic setting. Next, well logs and cross plots of elastic and reservoir properties were examined to determine general relationships between geophysical measurements and reservoir parameters of interest. Then, brief discussions of the theoretical bases for my modeling work are introduced. By using these theories and models, I demonstrate my research methodology and discuss the required data and inputs. Next, I examine the details of the modeling results obtained from the self-consistent model.

For the purpose of analysis, my discussion considers two primary topics. First, I determined pore aspect ratios of the formation by rock physics velocity modeling under the constant fluid properties; second, I analyzed the effect of fluid properties on

determining pore aspect ratios. I conclude with a discussion of these results to determine the reservoir characteristics of the Haynesville Shale in a practical sense.

### **1.3 GEOLOGICAL BACKGROUND**

The Haynesville Shale is a black, organic- and carbonate-rich shale of upper Jurassic age that underlies much of the Gulf Coast area. It was deposited about 150 million years ago in a shallow offshore environment and surrounded by carbonate platforms in the south and west, and by clastic formations in the north and northeast directions. The Haynesville Shale is underlain by the Smackover Formation and overlain by rocks of the Cotton Valley Group. The Cotton Valley Group is also called the Bossier Shale and primarily consists of sandy shales (Hammes et al., 2009).

The sequence stratigraphy of East Texas as it relates to the Haynesville Shale was introduced by Goldhammer (1998) and Goldhammer and Johnson (2001). Also, Hammes et al. (2009) analyzed specific sequence stratigraphy aspects of the Haynesville Shale. In the stratigraphic section illustrated in Figure 1.1, the Upper Jurassic section consists of two second-order super sequences, SS1 and SS2. Goldhammer and Johnson (2001) stated that the Smackover Formation formed during the late HST (high stand transgression) of SS1 (Super Sequence 1) and the Cotton Valley Group was deposited during the HST of SS1 and LST (low stand transgression) of SS2 (Super Sequence 2). The Haynesville Shale is organic- and carbonate-rich shale formation because it was deposited during the transgressive stage of SS2. In contrast to that, the Bossier Shale is a siliciclastic-rich shale deposited during the regressive phase of SS2.

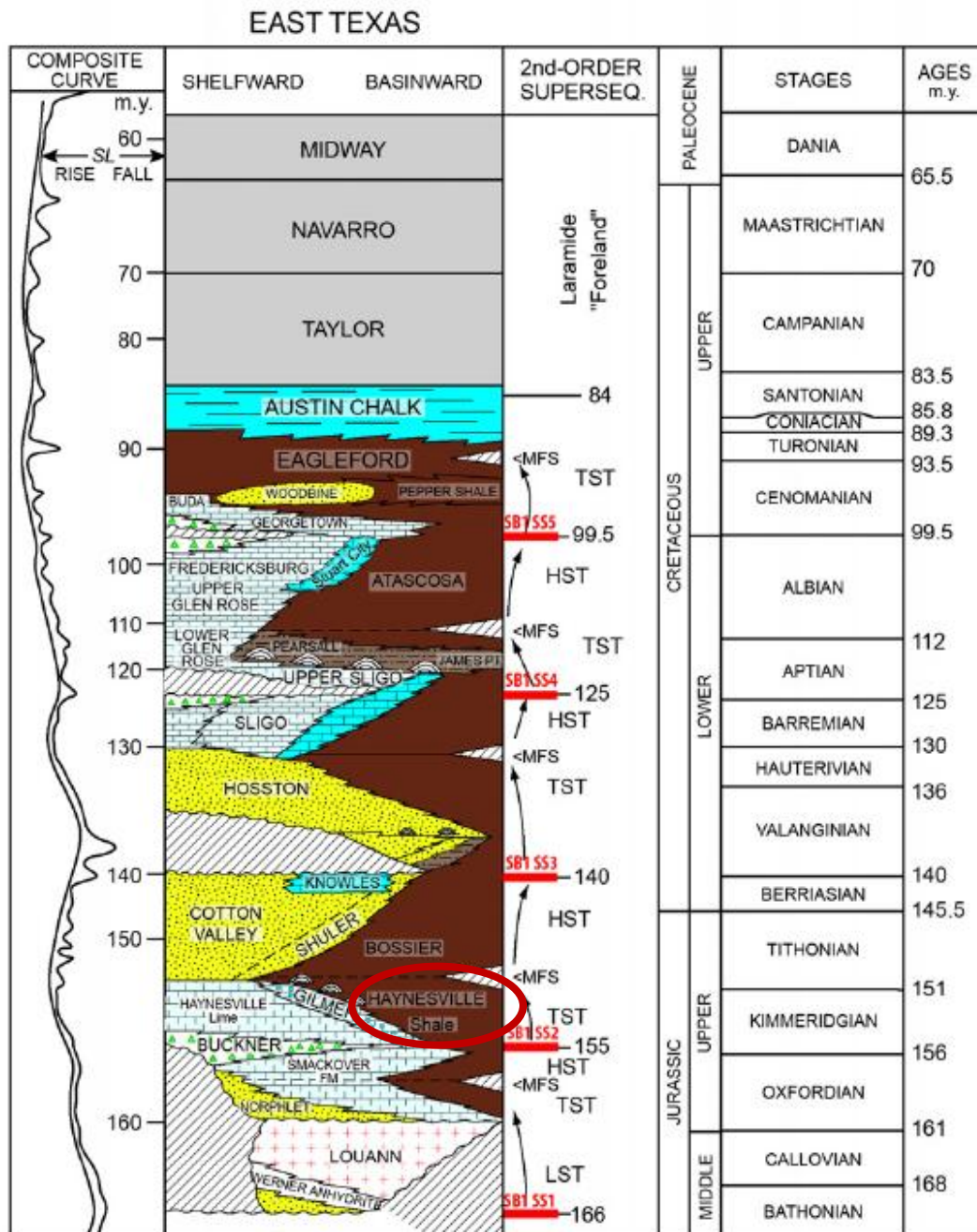


Figure 1.1: Stratigraphic section of East Texas (Goldhammer and Johnson, 2001). Hammes et al. (2009) modified ages and composite sea level. The Haynesville Shale is organic- and carbonate-rich shale formation deposited during a transgressive stage.

Because of its low permeability (in the micro to nanoDarcy range), the Haynesville was originally considered to be a gas source rock rather than a gas reservoir in spite of moderately high average porosity ranging from 8% to 12 % and relatively high total organic carbon (TOC) values that varies from 1% to 8% (Hammes et al., 2011). Geochemical and petrological analyses indicate that the Haynesville shale contains large amounts of carbonate, in addition to quartz and clay.

Since applying new techniques such as horizontal drilling and hydraulic fracturing, natural gas production from the Haynesville is one of the largest gas reservoirs in United States, which occurs from rocks about 10,000 to 13,000 feet subsurface in northwest Louisiana and East Texas. One of the unique characteristics of the Haynesville is a high overpressure whose geo-pressure gradient is more than 0.9 psi/ft. Because of this overpressure characteristic, Haynesville gas production shows a steeper decline curve (~80% in the first year) than other shale-gas plays (Wang and Hammes, 2011). In addition, this formation includes natural fractures as well as high calcite and quartz content. On account of high overpressure, natural fractures, and high calcite and quartz contents, the Haynesville Shale is considered a brittle rock, allowing for relatively easy hydraulic fracturing.

#### 1.4 MICRO-STRUCTURAL IMAGE

Figure 1.2 is a nano-scale image of the Haynesville Shale. Dark patches in the red ellipses are pieces of organic material (solid) inside of pores. Light gray features in the white ellipses are matrix or grains. Most pore shapes are flat (or crack-like), which have small aspect ratios. Grain shapes vary in this formation from flat to rounded of which the latter has large aspect ratios.

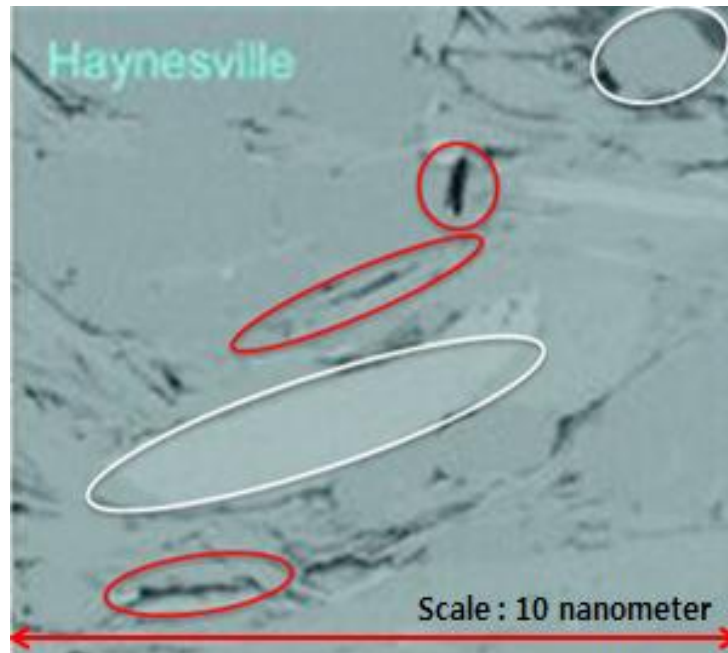


Figure 1.2: Nano-scale image of the Haynesville Shale (Modified from Curtis et al., 2010).

Figure 1.3 is an image showing the variability of pore types in the Haynesville. On the middle right, numerous nano-scale pores and one  $\mu\text{m}$ -scale pore are present (O). At the lower left (ip), a number of pores (inter-crystalline pores) are present between pyrite framboid crystals. In the top center (M), pores are present between organic matter

and mineral grain. Loucks et al. (2009) indicated that nano-scale pores with organic material are most likely related to hydrocarbon maturation, and the inter-crystalline pores between pyrite framboids and calcite crystals contribute a significant amount of porosity for gas storage.

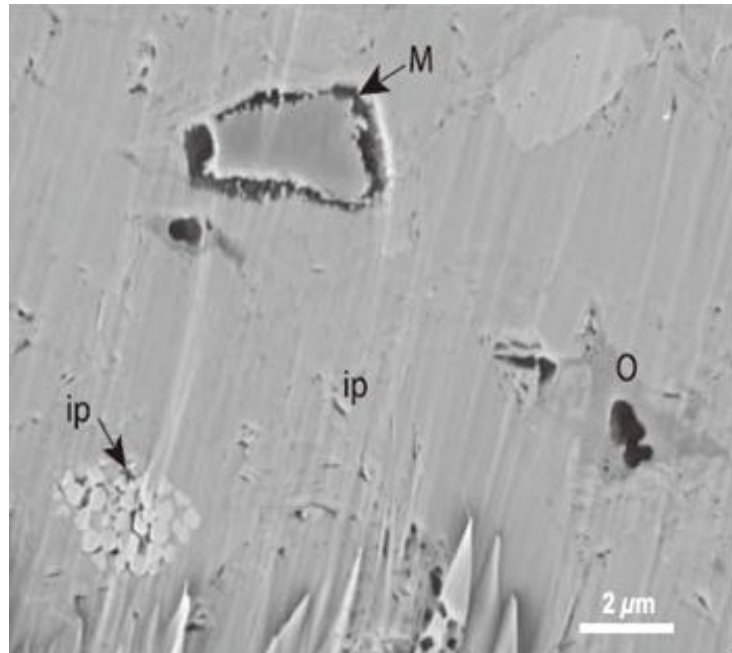


Figure 1.3: SEM image showing different pore types of the Haynesville including organic (O), interparticle (ip), and moldic (M) micropores and nanopores (Hammes et al., 2011).

## 1.5 WELL DATA

The well log data used in this thesis are from East Texas. Figures 1.4 and 1.5 are the well log data including gamma ray (API), density (g/cc), density-derived porosity (fraction), P-wave velocity (km/s), S-wave velocity (km/s), and  $V_p/V_s$  versus depth. The

density porosity log was calculated from the density log using the limestone matrix composition and water-saturated density (Figures 1.4 and 1.5). The relationship between rock bulk density and rock porosity is given by a volumetric average:

$$\rho_b = \varphi\rho_f + (1 - \varphi)\rho_m \quad (1.1)$$

Here,  $\rho_b$  is bulk density,  $\rho_m$  is matrix density,  $\rho_f$  is fluid density, and  $\varphi$  is total porosity. Solving the above equation for porosity requires that  $\rho_m$  and  $\rho_f$  be known in addition to the observed rock bulk density. Even though errors results in the calculation of total porosity using a limestone matrix and water density, it is assumed acceptable to use the calculated porosity because the main purpose of this thesis is to determine pore aspect ratios instead of calculating porosity. By assuming one type of fluid (water) and one type of rock matrix (limestone), total porosity ( $\varphi_D$ ) is then given by the equation.

$$\varphi_D = (2.71 - \rho_b) / (2.71 - 1) \quad (1.2)$$

Here,  $\rho_b$  is bulk density, 2.71 is limestone density (g/cc), 1 is water density (g/cc), and  $\varphi_D$  is density porosity.

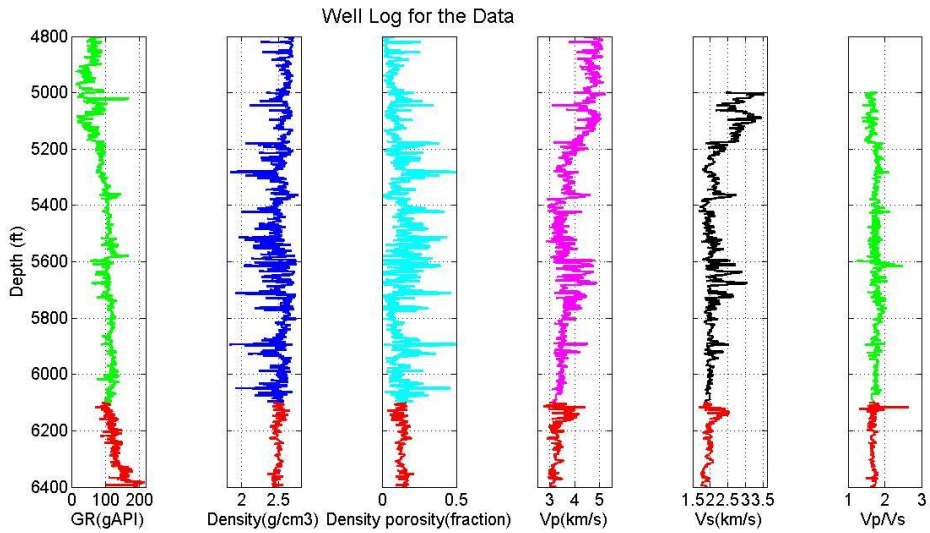


Figure 1.4: Well log data. From the left, gamma ray (API), density (g/cc), density porosity (fraction), P-wave velocity (km/s), S-wave velocity (km/s), and Vp/Vs ratio are plotted versus depth. The Haynesville Shale in this well is colored by red at the bottom of the figure. The vertical axis is artificial depth. Depth is disguised to maintain confidentiality of the well location.

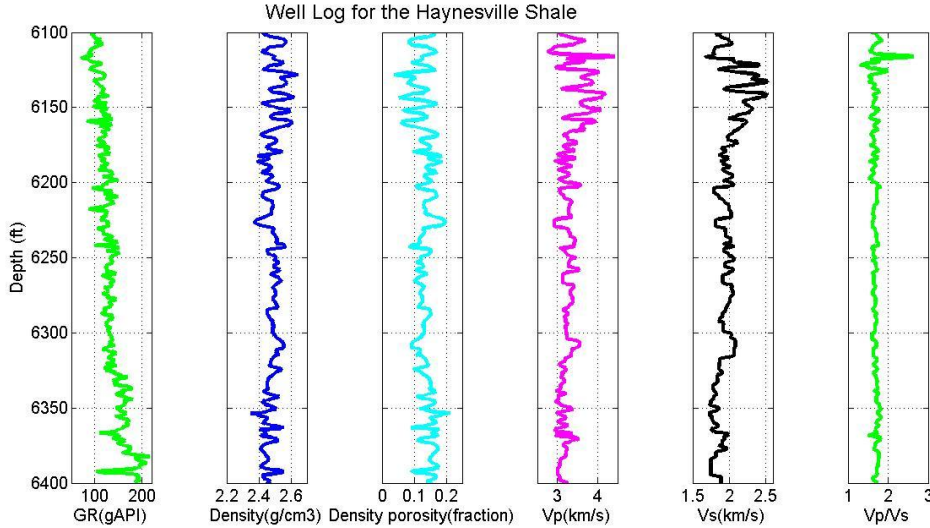


Figure 1.5: Well log data from the Haynesville Shale, showing the Haynesville (red) portions of the curves from Figure 1.4.

The Haynesville Shale shows higher gamma ray (API) values relative to the non-shaly overlying formation because the Haynesville contains a larger percentage of clays (average 35.6 %). In the Haynesville Shale, the lower section of the Haynesville Shale has higher gamma ray values than the upper section, which suggests an increase of shaly components. In addition, it has higher porosity and lower density and velocities than the overlying formation on account of increased clay and kerogen content. P-wave and S-wave velocities are inversely correlated with the gamma ray and are highly correlated with the density. Typically,  $V_p/V_s$  is a good indicator of the lithology. However,  $V_p/V_s$  values in Figure 1.5 do not correlate well with the gamma ray. The  $V_p/V_s$  log shows almost constant values for the entire depth range except for the top of the Haynesville while gamma ray values increase with increasing depth. This is mainly because S-wave velocities in this log were calculated from monopole P-wave velocities and estimated lithology information. In the Haynesville Shale, P-wave velocity varies from 2.75 to 4.42 km/s (average 3.28 km/s) and S-wave velocity ranges over 1.67 - 2.53 km/s (average 1.96 km/s). The range of bulk density is 2.35 through 2.65 g/cc with the average of 2.48 g/cc. The upper part of the Haynesville Shale has higher P-wave velocity (km/s) and S-wave velocity (km/s) than deeper sections. From this information, we interpret that the shallower intervals of the Haynesville contain less clay than the deeper intervals.

Figure 1.6 is well log data for middle part of the Haynesville Shale (6,200–6,230 feet), which is expanded to highlight the relationships among the well data curves. From the left, volume of clay, water saturation, porosity, and P-impedance were plotted versus depth. The P-impedance curve mirrors the porosity curve in Figure 1.6. We can see that there is an inverse relation between P-impedance and porosity and a direct relationship between water saturation and volume of clay.

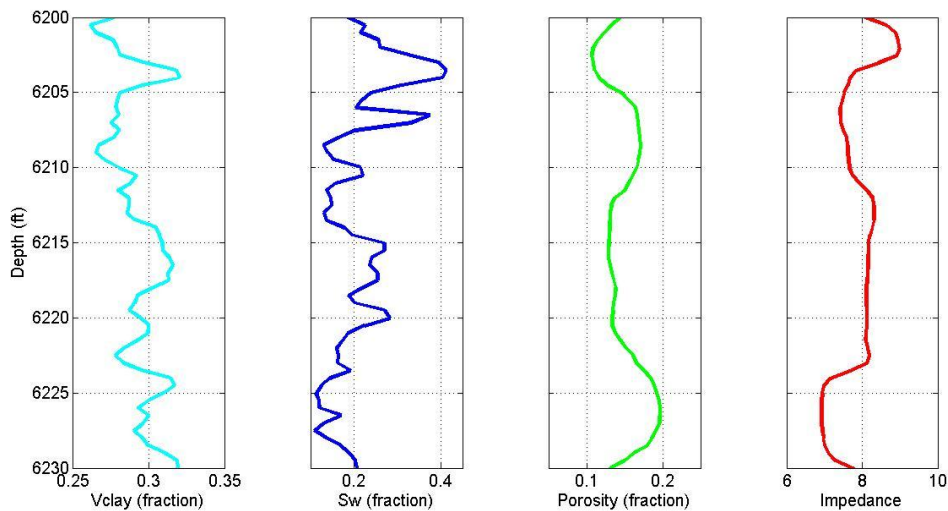


Figure 1.6: Well log data for the middle part of the Haynesville Shale. From the left, volume of clay, water saturation, porosity, and P-impedance versus depth. This part shows good relationships among the well data curves due to small changes of data.

Figure 1.7 shows the relationships (cross plots) between seismic velocities and reservoir properties of the Haynesville Shale. Those are cross plots for  $V_p$  versus porosity,  $V_s$  versus porosity,  $V_p$  versus  $V_s$ , and P-impedance versus porosity for Figures 1.7a-d, respectively. Data points are colored by gamma ray. P-wave and S-wave velocities are inversely correlated to porosity and change significantly with small changes in porosity. P-impedance is also inversely correlated to porosity. The general velocity

trends of the Haynesville Shale increase with decreasing porosity and clay content. Red indicates high GR, which is inferred as high clay content.

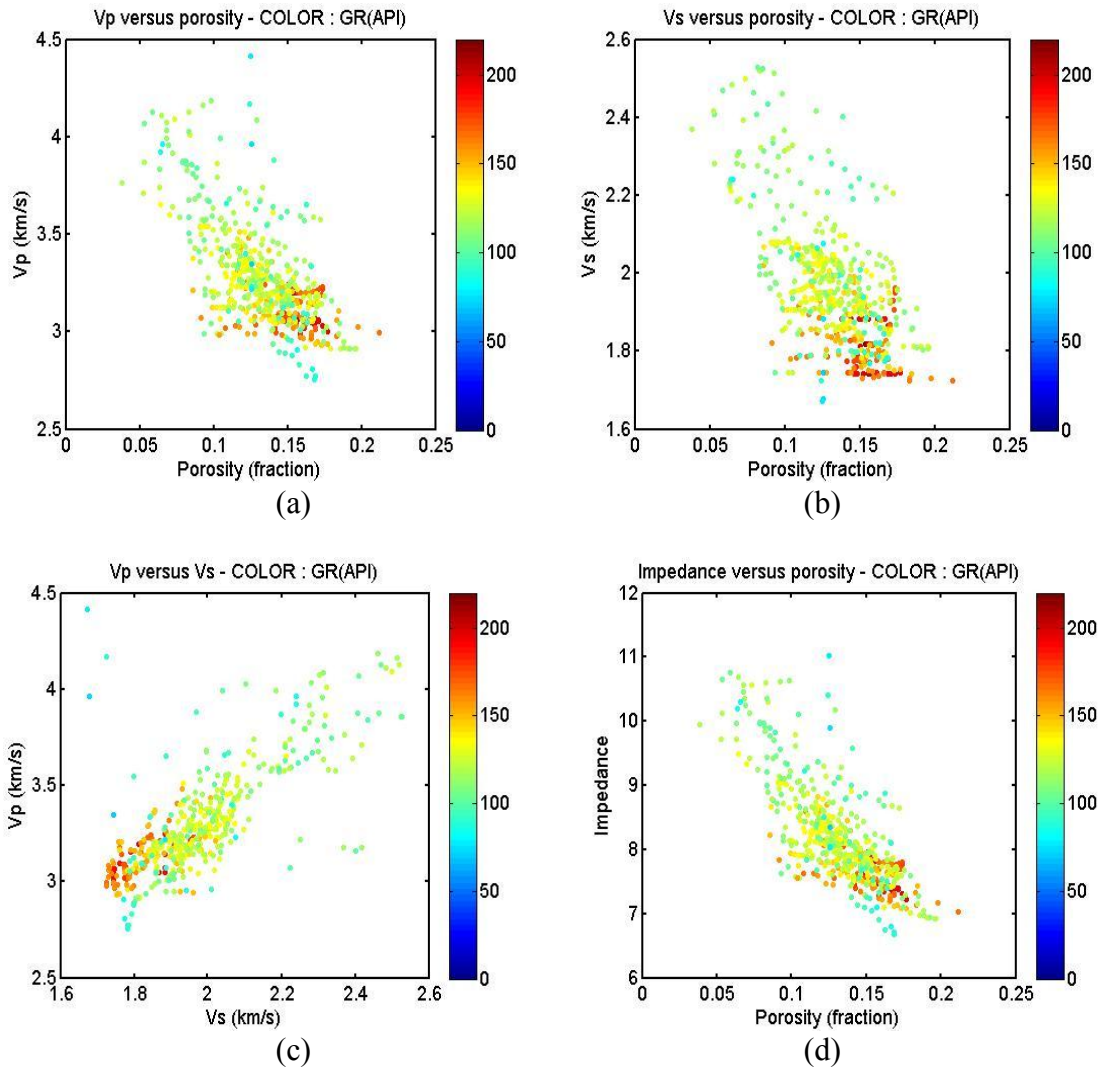


Figure 1.7: Cross plots of the Haynesville Shale. (a) Vp versus porosity (b) Vs versus porosity (c) Vp versus Vs (d) P-impedance versus porosity. Data points are colored by gamma ray where high GR indicates high clay content.

Figure 1.8 shows that when porosity decreases and density increases, water saturation increases slightly, but volume content of clay is nearly constant regardless of the porosity.

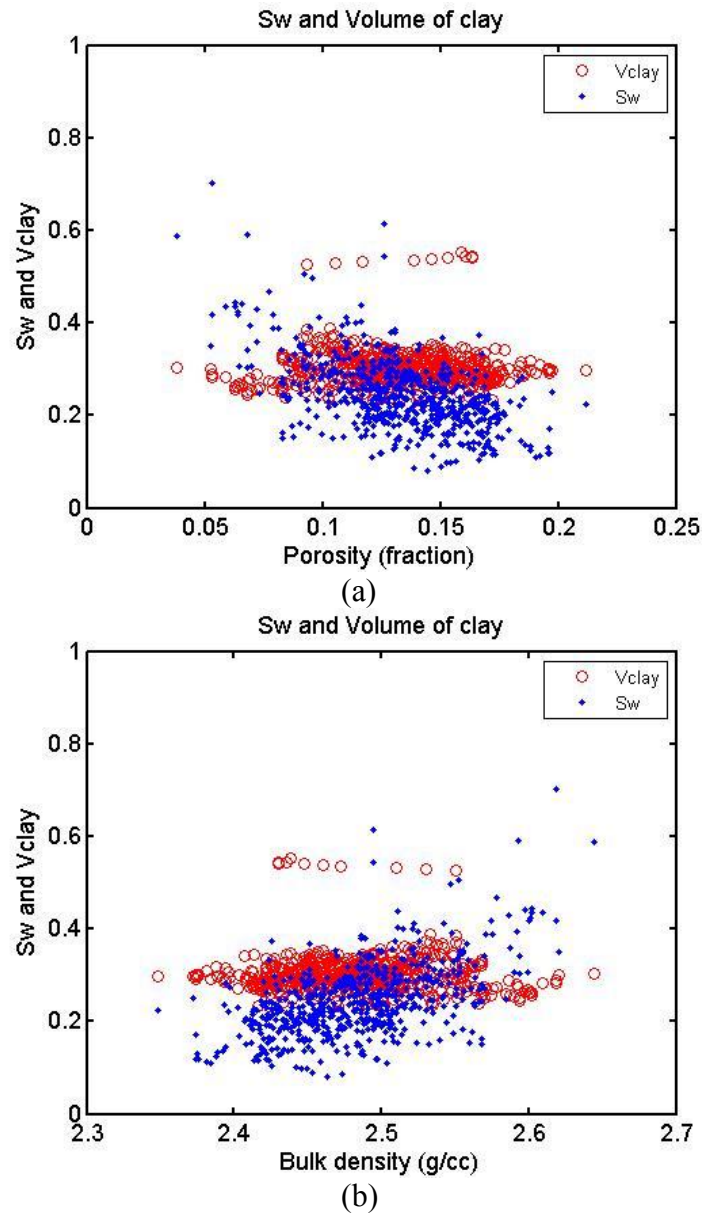


Figure 1.8: Cross plots of the Haynesville Shale. Water saturation and volume of clay versus (a) porosity and (b) density.

In summary, the Haynesville Shale has higher gamma ray (GR) values because of higher clay content, and velocities are lower than the overlying Bossier formation on account of clay and kerogen content. From the reservoir properties of the well logs and cross plots of the Haynesville Shale, in general, velocity increases with decreasing porosity and increasing density. There is an inverse relationship between P-impedance and porosity. In addition, porosity and water saturation show an inverse relationship, but there is no correlation between volume content of clay and porosity. Table 1.1 summarizes the well data and reservoir properties of the Haynesville Shale together with data from the entire logged section.

Table 1.1: Well data and the range of reservoir properties of the well.

Data	Total well	Haynesville
GR (gAPI)	13.4 - 215.2	71.2 - 215.2
Bulk density (g/cc)	1.839 - 2.755	2.348 - 2.645
Density porosity (fraction)	0.000 - 0.509	0.038 - 0.212
Volume of clay (fraction)	0.231 - 0.616	0.231 - 0.552
Vp (km/s)	2.754 - 5.466	2.754 - 4.418
Vs (km/s)	1.673 - 3.511	1.673 - 2.527
P-impedance (g/cc*km/s)	6.152 - 14.650	6.671 - 11.030
Vp/Vs	1.250 - 2.6419	1.314 - 2.641
Caliper (inch)	4.500 - 10.727	6.627 - 10.195
Sw (fraction)	0.082 - 0.702	0.082 - 0.702

## 1.6 REFERENCES

Avseth, P., Mukerji, T., Mavko, G., and Dvorkin, J., 2010, Rock-physics diagnostics of depositional texture, diagenetic alterations, and reservoir heterogeneity in high-porosity siliciclastic sediments and rocks - A review of selected models and suggested work flows, *Geophysics*, 75, 75A31–75A47.

- Curtis, M. E., Ambrose, R. J., Sondergeld, C. H., and C. S. Rai, 2010, Structural characterization of gas shales on the micro-and nano-scales: Canadian Society for Unconventional Gas/Society of Petroleum Engineers, DOI: 10.2118/137693-MS.
- Goldhammer, R. K., 1998a, Second-order accommodation cycles and points of “stratigraphic turnaround”: Implications for high-resolution sequence stratigraphy and facies architecture of the Cotton Valley Lime/Haynesville of the East Texas Salt Basin (abs): AAPG 1998 Annual Convention, Salt Lake City, Utah.
- Goldhammer, R. K., and Johnson, C. A., 2001, Middle Jurassic-Upper Cretaceous paleogeographic evolution and sequence stratigraphic framework of the northwest Gulf of Mexico rim, in C. Bartolini, A. Cantu-Chapa, and R.T. Buffler, eds., The western Gulf of Mexico Basin: Tectonics, sedimentary basins and petroleum systems: AAPG Memoir **75**, p. 45-81.
- Hammes, U., Eastwood, R., Rowe, H. D., and Reed, R. M., 2009, Addressing conventional parameters in unconventional shale-gas systems: depositional environment, petrography, geochemistry, and petrophysics of the Haynesville Shale: 29th Annual GCSSEPM Foundation Bob F. Perkins Research Conference, Houston, 181–202.
- Hammes, U., Hamlin, H. S., and Ewing, T. E., 2011, Geologic analysis of the Upper Jurassic Haynesville Shale in east Texas and west Louisiana, AAPG Bulletin, **95**, 1643-1666.
- Loucks, R. G., R.M. Reed, S.C. Ruppel, and D. Jarvie, 2009, Morphology, Genesis, and Distribution of Nanometer-Scale Pores in Siliceous Mudstones of the Mississippian Barnett Shale, Journal of Sedimentary Research, **79**, 848-861.
- Mavko, G., Mukerji, T. and Dvorkin, J., 2009, The rock physics handbook (2nd Edn), Cambridge Univ. Press, Cambridge, England.
- O’Connell, R. and B. Budiansky, 1974, Seismic velocities in dry and saturated crack solids: Journal of Geophysics Research, **79**, 5412-5426.
- Sondergeld, C. H., Ambrose, R. J., Rai, C. S., and Moncrieff, J., 2010, Micro-Structural Studies of Gas Shales, 2010 SPE Unconventional gas Conference, Pittsburgh, Pennsylvania.
- Sun, Y. F., 2004, Pore structure effects on elastic wave propagation in rocks: AVO modeling, Journal of Geophysics and Engineering, **1**, 268–276.
- Wang, F. P., and Hammes, U., 2011, Effects of petrophysical factors on Haynesville fluid flow and production, World Oil, **231**, pD.79-D.82.

## Chapter 2: Theory

This section describes several theories used in velocity modeling for this thesis. Although the theories are discussed separately under the five concept headings, it should be understood that separate explanations are necessary for brevity and clarity. All these conceptions are interrelated and interdependent.

### 2.1 EFFECTIVE MEDIUM THEORY

Sonic log data can include large fluctuations in P-wave and S-wave velocities because they are measured at high frequencies (approximately 10 kHz) approximately every 15 cm (0.5 feet) within the wellbore. These fluctuations are significantly decreased at the lower frequencies (below 100 Hz) of surface seismic data because the wavelength is much larger than at the well log scale. Because of different measurement scales for data, we need to upscale well log data to the longer wavelength seismic scale. Then we can understand how elastic properties and estimated rock properties appear at the seismic scale.

Upscaling means theoretically predicting the elastic properties in rocks at lower frequency from higher frequency sonic logging data (Bayuk et al., 2007). When the wavelength ( $\lambda$ ) is large compared to the layer thickness ( $d$ ), the wave velocity is estimated by an average of the properties in the individual layers (Backus, 1962), assuming each layer is isotropic. The waves behave as if propagating in an effective homogeneous medium. In contrast, when the wavelength ( $\lambda$ ) is small compared to the layer thickness ( $d$ ), the waves obey ray theory, which is a high-frequency approximation.

The effective medium theory encompasses the Backus average in the low-frequency limit and ray theory in the high-frequency limit. When  $\lambda / d \gg 1$ , a stratified medium behaves as a homogeneous effective elastic medium with wave propagation normal to the layering. The equation that describes this is

$$V_{EMT} = \left( \frac{M_{EMT}}{\rho_{ave}} \right)^{1/2}. \quad (2.1)$$

The effective velocity,  $V_{EMT}$ , is calculated using the Backus average of the elements of the elastic stiffness tensors  $C_{ij}$  of the constituents. For normal incidence propagation through horizontal layers, this is equivalent to the Reuss average or iso-stress average of the P-wave modulus.

$$M_{EMT} = \left[ \sum_k \frac{f_k}{M_k} \right]^{-1} \quad \text{or} \quad \frac{1}{\rho_{ave} V_{EMT}^2} = \sum_k \frac{f_k}{\rho_k V_k^2} \quad (2.2)$$

$$\rho_{ave} = \sum_k f_k \rho_k \quad (2.3)$$

Here,  $f_k$  is the fractional thickness,  $\rho_k$  are layer densities,  $M_k$  are layer moduli, and  $V_k$  are velocities of each layer.

The fundamental elastic properties of the rocks are the elastic moduli and bulk density. Elastic moduli can be calculated from P-wave velocity, S-wave velocity, and bulk density in the isotropic and elastic case. For the isotropic and elastic case, the relationships between velocities and moduli are in Equations 2.4–2.6.

$$K = \rho(V_p^2 - (4/3)V_s^2) \quad (2.4)$$

$$\mu = \rho V_s^2 \quad (2.5)$$

$$M = \rho V_p^2 = K + \left(\frac{4}{3}\right)\mu \quad (2.6)$$

These properties are averaged in the Backus technique. For the elastic moduli, the harmonic average is used. For the bulk density, the arithmetic average is used. However, the upscaling calculation should not distort the geologic geometry (Lindsay and Koughnet, 2001). For this process to be reliable, the Backus average can be calculated using a moving window, where a stack of thin layers is approximated by the properties of a single thick layer. In other words, the Backus average is used to model a finely stratified medium as a single homogeneous medium. Implemented sequentially as a moving average, this Backus average effectively upscales log data to the seismic scale data while preserving gradational interfaces.

The size of the moving window can be chosen for the anticipated seismic bandwidth. Smooth, seismic-scale velocities are found after upscaling log measurements to the seismic scale data (Figure 2.1).

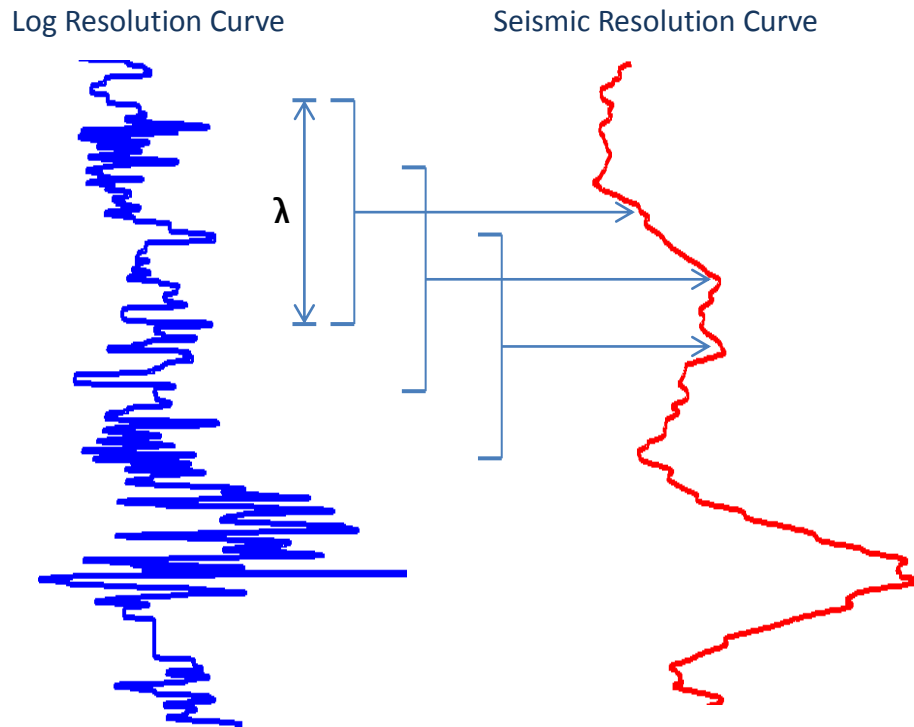


Figure 2.1: Concept of the moving Backus average in case of 50 Hz seismic scale.

In this study, I used two frequencies, 20 Hz and 50 Hz, to calculate a moving average as a function of depth. These two frequencies were selected because they are in the bandwidth (10–100 Hz) of surface seismic data.

Figure 2.2 is the moving Backus averages of P-wave and S-wave velocities for the Haynesville Shale data. P-wave and S-wave velocities of well log data were averaged within the moving windows for 20 and 50 Hz. Therefore, the log data are smoothed after upscaling.

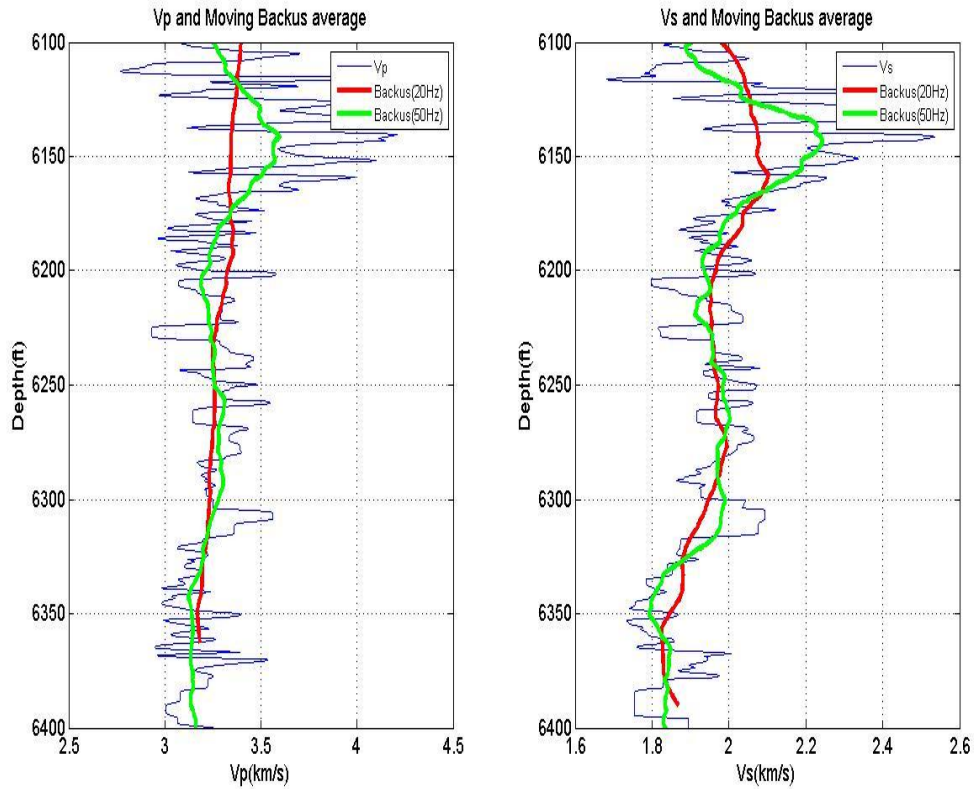


Figure 2.2: Moving Backus average for 20 Hz (red) and 50 Hz (green). From the left to right, moving Backus averages for P-wave velocity (km/s) and S-wave velocity (km/s) are plotted versus depth.

Figure 2.3 is the moving arithmetic averages of density and porosity for 20 and 50 Hz, respectively. For density and porosity, the arithmetic average is used when upscaling log measurements to the seismic scale data using Equation 2.3.

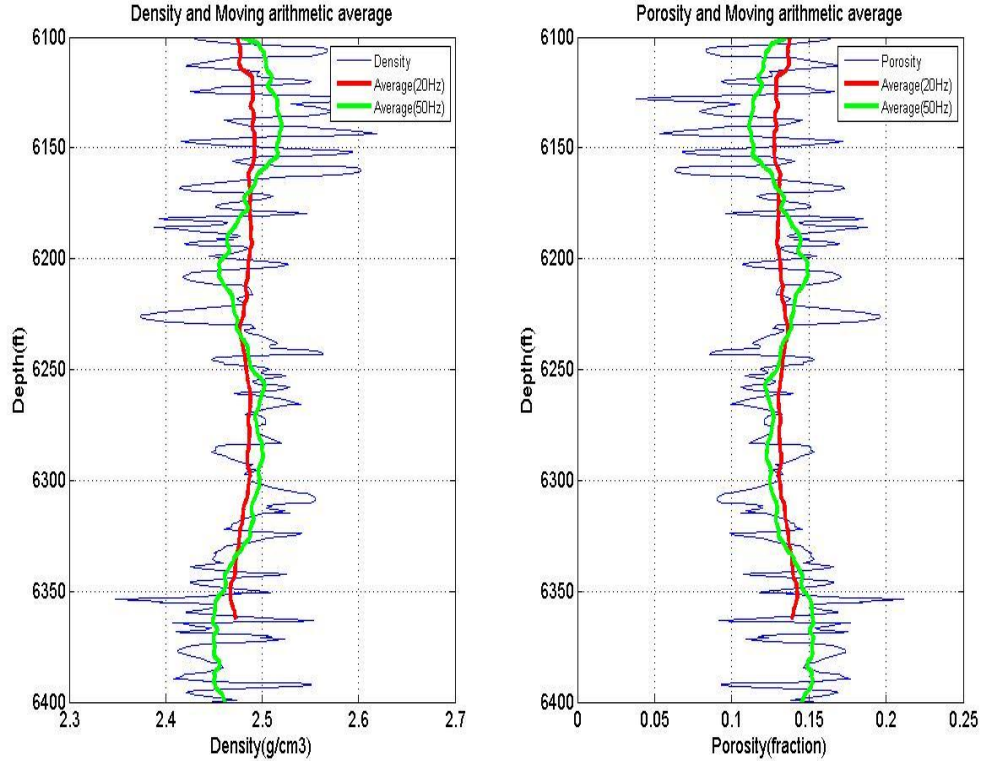


Figure 2.3: Moving arithmetic average for 20 Hz (red) and 50 Hz (green). From the left to right, moving arithmetic averages for density (g/cc), and porosity (fraction) are plotted versus depth.

Figure 2.4 is the moving arithmetic averages of P-impedance, S-impedance and  $V_p/V_s$  for 20 and 50 Hz, respectively. Upscaled impedance curves show similar patterns with upscaled velocity curves because impedances are results of the multiplication of velocity and density. Upscaled  $V_p/V_s$  were calculated from the moving Backus averages of P-wave and S-wave velocities. These values also show smooths change as a function of depth.

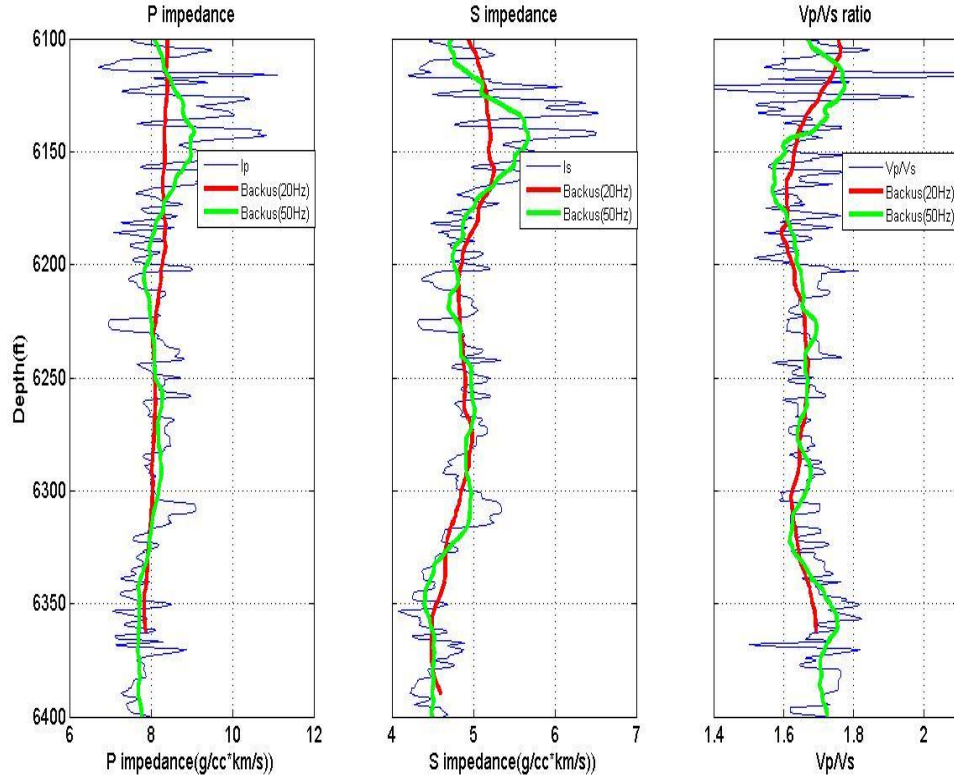


Figure 2.4: Moving arithmetic average for 20 Hz (red) and 50 Hz (green). From the left to right, moving arithmetic averages for P impedance (g/cc\*km/s), S impedance (g/cc\*km/s) and Vp/Vs are plotted versus depth.

## 2.2 SELF-CONSISTENT MODEL

To estimate the effective moduli of a composite or porous elastic material for the Haynesville Shale, we need to know the elastic properties and the volume fractions of the individual components, and the geometric details of the shapes and spatial distributions of the components and pores (Mavko et al., 2009). We do not know exactly each of these parameters at every location in a reservoir or other rock formations. A rock physics model such as the self-consistent model approximates these parameters by representing grains and pores as idealized shapes. It is able to represent multiple mineral phases for idealized ellipsoidal pores. Avseth et al. (2010) indicated that inclusion models such as the self-consistent model approximate the rock as an elastic solid containing dry or fluid-filled inclusion that represents the pore space. This model is most accurate for relatively low concentrations of pore inclusions because it does not account for the elastic interactions between the pores. In addition, it assumes that the pore inclusions are isolated, and the fluids cannot move between the pores. Accordingly, it is considered a high-frequency model most appropriate to model ultrasonic laboratory conditions because there is no time for wave-induced pore pressure to equilibrate. The Haynesville Shale has very low permeability and essentially isolated pores.

Figure 2.5 is a schematic diagram of the self-consistent model. The square represents an infinite background matrix and the circle does a rock. Inside the rock, blue and black ellipses represent isolated mineral grain inclusions and pore inclusions, respectively. Isolated mineral grains and pore inclusions with various aspect ratios in the rock are assumed to be imbedded in an infinite background matrix of unknown properties. The aspect ratio ( $\alpha$ ) of an ellipsoid is defined as the ratio between its smallest and largest axes. The elastic properties of the solid grains and pores affect the elastic

moduli of the rock. These unknown properties of the background matrix are perturbed until the inclusion effects vanish. These properties represent a unique solution for the effective elastic properties of the mixed material at some point (Jensen et al., 2011).

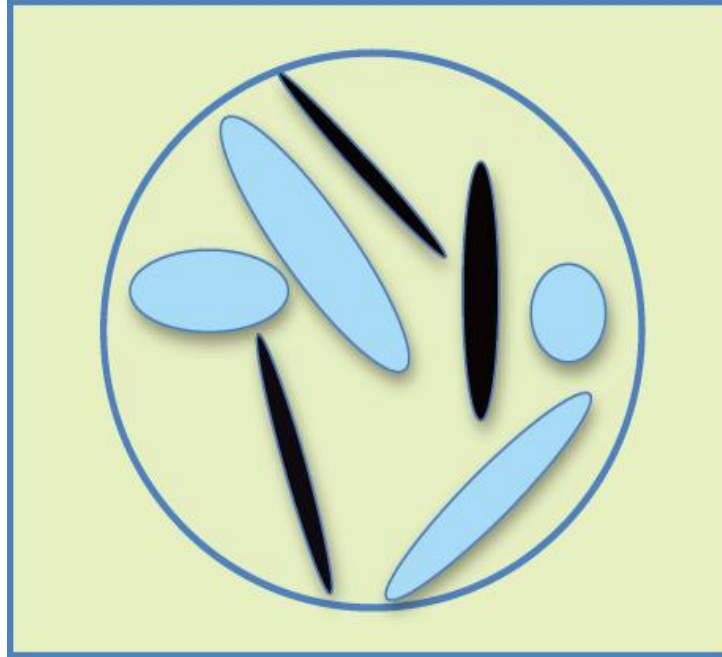


Figure 2.5: Schematic diagram of the self-consistent model. The square represents an infinite background matrix and the circle does a rock. Blue and black ellipses represent mineral grain inclusions and pore inclusions in the square, respectively (Courtesy of Jiang and Spikes, 2011).

Berryman (1980) introduced a general form of the self-consistent model for N-phase composites (Mavko et al., 2009). The effective moduli of the infinite background matrix can be solved by simultaneous iteration for unknown quantities ( $K_{SC}^*$  and  $\mu_{SC}^*$ ) in Equations 2.7 and 2.8.

$$\sum_{i=1}^N x_i (K_i - K_{SC}^*) P^{*i} = 0 \quad (2.7)$$

$$\sum_{i=1}^N x_i (\mu_i - \mu_{SC}^*) Q^{*i} = 0 \quad (2.8)$$

Where  $i$  refers to the  $i^{th}$  material,  $x_i$  is its volume fraction of each phase of the rock, and  $P$  and  $Q$  are geometric factors. In these equations,  $K_{SC}^*$  and  $\mu_{SC}^*$  are the effective (self-consistent) bulk and shear moduli, respectively, of a porous medium with randomly oriented penny-shaped cracks to be calculated by simultaneous iteration. The summation includes minerals and pores. Bulk and shear modulus, density, and aspect ratio for minerals, fluids, and pores are needed to solve Equations 2.7 and 2.8.

For geometric factors,  $P$  and  $Q$  of ellipsoidal inclusions of arbitrary aspect ratio in Equations 2.7 and 2.8, Berryman (1980) gives the relevant scalars required for computing  $P$  and  $Q$  as

$$P^{*i} = \frac{1}{3} T_{iijj} \quad (2.9)$$

$$Q^{*i} = \frac{1}{5} \left( T_{ijij} - \frac{1}{3} T_{iijj} \right) . \quad (2.10)$$

The strain tensors,  $T_{iijj}$  and  $T_{ijij}$  in Equations 2.9 and 2.10 are computed by numerical methods as below.

$$T_{iijj} = \frac{3F_1}{F_2} \quad (2.11)$$

$$T_{ijij} - \frac{1}{3} T_{iijj} = \frac{2}{F_3} + \frac{1}{F_4} + \frac{F_4 F_5 + F_6 F_7 - F_8 F_9}{F_2 F_4} \quad (2.12)$$

Where

$$F_1 = 1 + A \left[ \frac{3}{2} (f + \theta) - R \left( \frac{3}{2} f + \frac{5}{2} \theta - \frac{4}{3} \right) \right] \quad (2.13)$$

$$F_2 = 1 + A \left[ 1 + \frac{3}{2} (f + \theta) - \frac{1}{2} R(3f + 5\theta) \right] + B(3 - 4R) \\ + \frac{1}{2} A(A + 3B)(3 - 4R)[f + \theta - R(f - \theta + 2\theta^2)]$$

$$F_3 = 1 + A \left[ 1 - \left( f + \frac{3}{2} \theta \right) + R(f + \theta) \right]$$

$$F_4 = 1 + \frac{1}{4} A[f + 3\theta - R(f - \theta)]$$

$$F_5 = A \left[ -f + R \left( f + \theta - \frac{4}{3} \right) \right] + B\theta(3 - 4R)$$

$$F_6 = 1 + A[1 + f - R(f + \theta)] + B(1 - \theta)(3 - 4R)$$

$$F_7 = 2 + \frac{1}{4} A[3f + 9\theta - R(3f + 5\theta)] + B\theta(3 - 4R)$$

$$F_8 = A \left[ 1 - 2R + \frac{1}{2} f(R - 1) + \frac{1}{2} \theta(5R - 3) \right] + B(1 - \theta)(3 - 4R)$$

$$F_9 = A[(R - 1)f - R\theta] + B\theta(3 - 4R)$$

In Equation 13,  $A$ ,  $B$ , and  $R$  are given by

$$A = \frac{\mu_i}{\mu_m} - 1 \quad (2.14)$$

$$B = \frac{1}{3} \left( \frac{K_i}{K_m} - \frac{\mu_i}{\mu_m} \right)$$

$$R = \frac{(1 - 2\nu_m)}{2(1 - \nu_m)}$$

For oblate spheroids ( $\alpha < 1$ ), the functions  $\theta$  and  $f$  are given by

$$\theta = \frac{\alpha}{(1 - \alpha^2)^{3/2}} \left[ \cos^{-1} \alpha - \alpha(1 - \alpha^2)^{1/2} \right] \quad (2.15)$$

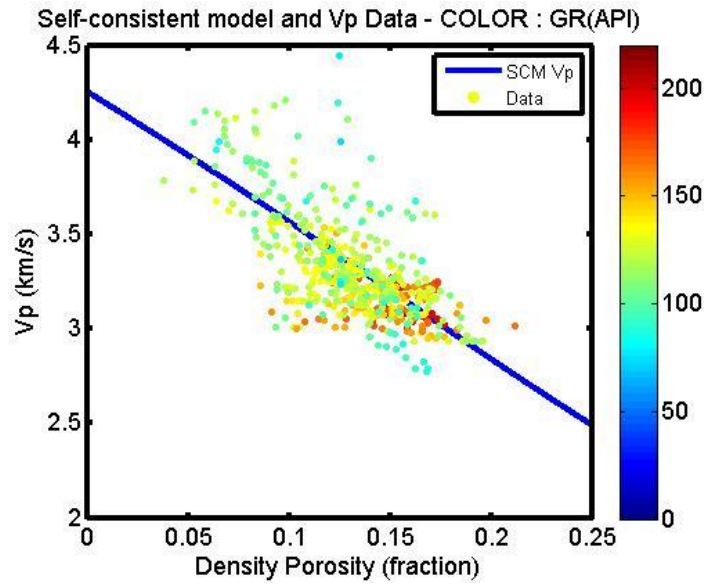
$$f = \frac{\alpha^2}{(1 - \alpha^2)} (3\theta - 2)$$

Figures 2.6 and 2.7 show cross plots of P-wave velocity, S-wave velocity, bulk modulus, and shear modulus versus total porosity for the Haynesville Shale data along with a self-consistent model (blue lines). Elastic properties of fluids in the pore spaces were fixed values (Bulk modulus: 1 GPa and density: 0.8 g/cc for fluids). In the model, 50 pore inclusions in the rock were assumed. The aspect ratios for the pore inclusions were assumed with mean 0.145, and normally distributed with standard deviation 0.01. An average composition of the Haynesville Shale from the XRD data was used (Table 2.1). The blue lines are modeled velocities calculated from the self-consistent model. Data points are colored by gamma ray values.

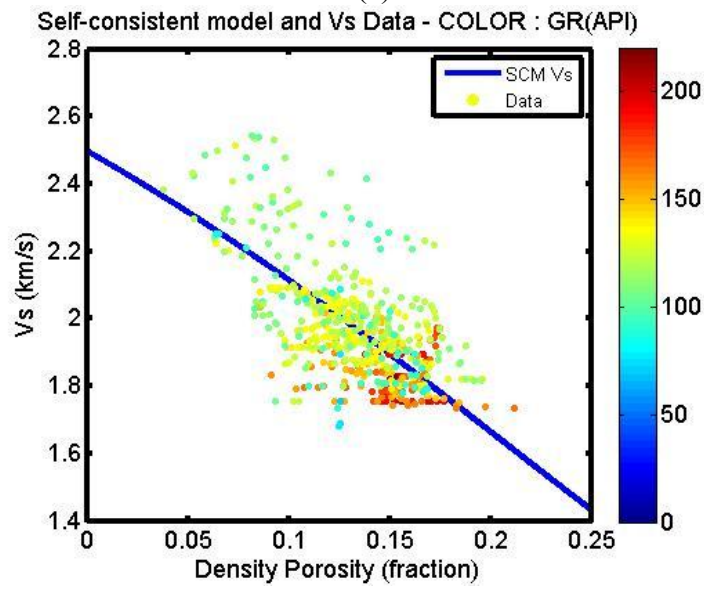
These plots show the trend that effective bulk moduli, shear moduli, P-wave and S-wave velocities modeled from the self-consistent model decrease while total porosity increases. These calculated results are similar to measured data values and cross almost the center of the data. Therefore, the self-consistent approximation characterizes the overall trend observed in the data from the Haynesville Shale.

Table 2.1: Average fractional (%) composition data of the Haynesville Shale.

Data	Quartz	Feldspar	Calcite	Dolomite	Pyrite	Kerogen	Clay	Sum
Mean	31.7	8.1	14.2	3.2	2.0	5.2	35.6	100



(a)



(b)

Figure 2.6: Cross plots of (a)  $V_p$  and (b)  $V_s$  versus porosity data overlain with the self-consistent modeling results for the Haynesville Shale. Data points are colored by gamma ray values. The colored lines are the results of the self-consistent model with average composition from the XRD data and normally distributed pore aspect ratio (mean 0.145, standard deviation 0.01). These modeled lines fit well to the measured data reasonably (Bulk modulus: 1 GPa and density: 0.8 g/cc for fluids).

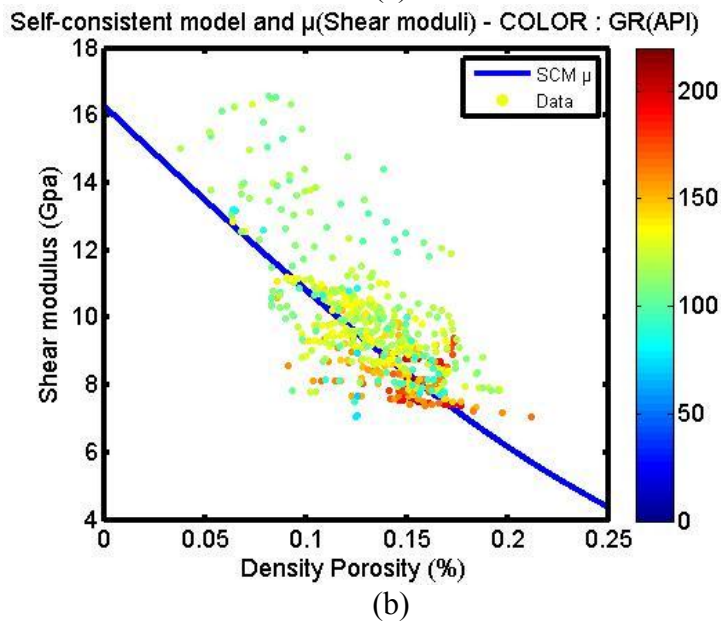
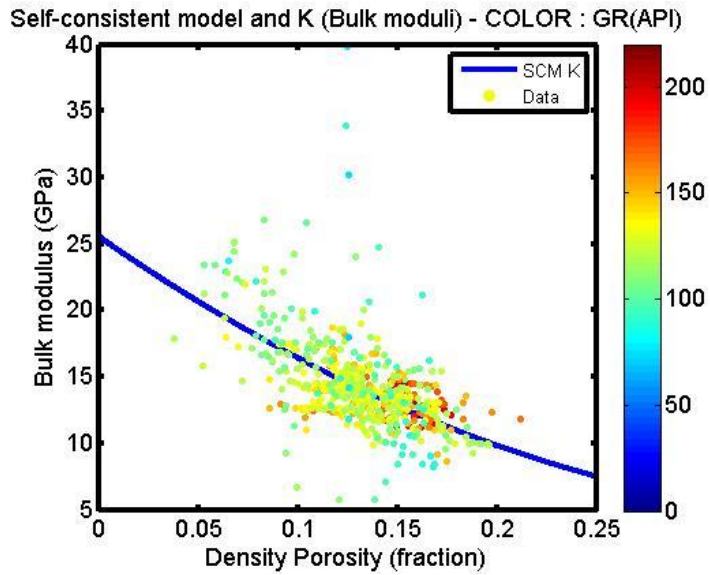


Figure 2.7: Cross plots of (a) bulk modulus ( $K$ ) and (b) shear modulus ( $\mu$ ) versus porosity data overlay with the self-consistent modeling results for the Haynesville Shale. Data points are colored by gamma ray values. The blue lines are from the self-consistent model using same input values in Figure 2.6. These blue lines fit well to the measured data and cross almost the center of the data cluster.

### 2.3 FLUID MIXTURES AND SATURATION SCALES

Knight and Nolen-Hoeksema (1990) and Berryman et al. (1999) demonstrated that laboratory data being collected during a continuous imbibition/drainage experiment showed a clear dependence of elastic wave velocities on the detail of the pore-scale distribution of water and air in the rock. Imbibition is the increase of water saturation in a water-wet sample by the displacement of a non-wetting fluid by water; drainage is the decrease of water saturation in a water-wet sample by the displacement of water by a non-wetting fluid. Longeron et al. (1989) and Knight (1991) also found hysteresis in the electrical resistivity of partially saturated rocks during repeated imbibition-drainage cycles.

It is clear from these results that the details of pore scale fluid distribution are very important in the interpretation of both the elastic and electrical data from partially saturated rocks. The experimental results from these studies clearly show the existence of hysteresis in the dependence of elastic wave velocities and electrical resistivity on water saturation. Figure 2.8 shows the hysteresis effect between the imbibition and drainage experiments. This effect becomes significant in the higher saturation region ( $S_w > 0.8$ ) where  $V_p$  increases rapidly to larger values.  $V_s$  also increases in the higher saturation region but not nearly as fast as  $V_p$  does.

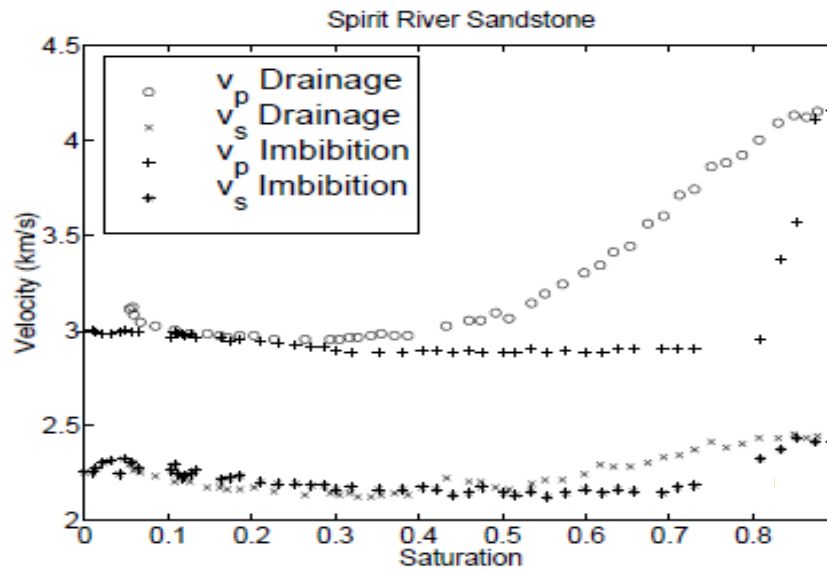


Figure 2.8:  $v_p$  and  $v_s$  versus water saturation ( $S_w$ ) measured during a continuous imbibition/drainage experiment (Berryman et al., 1999).

From this result, it is apparent that elastic velocities can be significantly affected by the pore scale distribution of fluids. Therefore, velocities depend on both saturation and the fluid mixing scales (Avseth et al., 2005). The imbibition is typical when phases are mixed at a fine scale (uniform saturation). On the other hand, the drainage is typical when the phases are mixed at a coarse scale (patchy saturation). Figure 2.9 explains how the fluids are mixed in the pore space. In the patchy saturation scenario, patches in the top of Figure 2.9 are isolated from one another at a coarse scale; some patches are stiff and some are softer. Therefore, overall effective velocity is higher. In contrast to that, fluids are mixed at a fine scale in the uniform saturation in the bottom of the Figure 2.9. Stiffness in the uniform saturation is less than the case of patchy saturation. The patchy saturation case corresponds to a high frequency response and the uniform saturation to a very low frequency response.

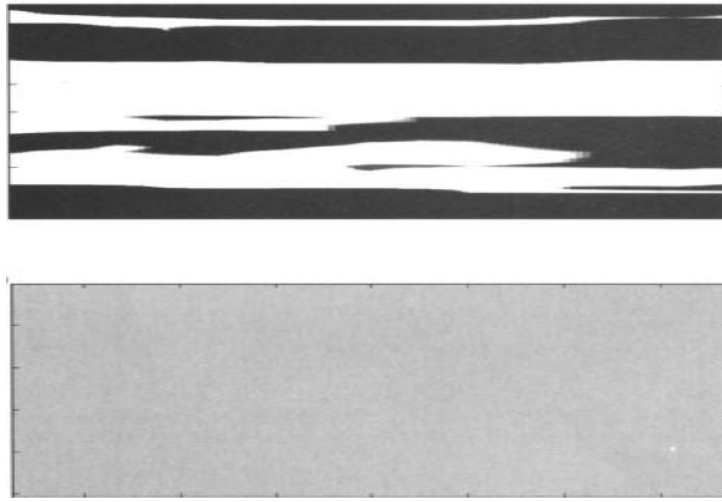


Figure 2.9: Schematic diagram for patchy saturation and uniform saturation. Upper figure is the patchy saturation at a coarse scale and bottom one explains the uniform saturation at a fine scale between water and oil (Mavko and Mukerji, 1998). Coarse-scale saturation increases the stiffness and velocity of the rock. However, fine-scale saturation is softer and low velocity than the coarse-scale saturation.

The patchy and uniform saturation curves are upper and lower bounds in terms of fluid-mixing scales. The uniform saturation model is typically used for reservoirs with oil and water cases. Reservoirs with gas are very likely to show patchy behavior. The patchy saturation upper bound can be found by the Voigt average, and the uniform saturation lower bound can be calculated by the Reuss average of the fluid moduli (Mavko et al., 2009).

$$K_{fl} = \sum S_i K_i \quad (2.16)$$

$$\frac{1}{K_{fl}} = \sum \left( \frac{S_i}{K_i} \right) \quad (2.17)$$

In Equations 2.16 and 2.17,  $K_{fl}$  is the effective bulk modulus of the fluid mixture,  $K_i$  is the bulk modulus of each fluid phase, and  $S_i$  represents its fractional saturation. The water saturation is defined as the volume fraction of the pore space filled with water, the remainder being filled with a fluid other than water. In order to accurately interpret geophysical data such as seismic velocities as a function of saturation, the dependence of the elastic properties on pore-fluid mixing needs to be more fully understood. According to Mavko and Mukerji (1998), patchy saturation always lead to higher seismic velocities than if the same fluids are mixed uniformly at a fine scale.

## 2.4 GASSMANN FLUID SUBSTITUTION

Gassmann (1951) fluid substitution allows us to obtain the bulk and shear modulus of a porous fluid-saturated rock from the dry rock and mineral bulk modulus, porosity, and fluid modulus (Equation 2.18). This can be done under the assumptions that the rock is isotropic, the mineral modulus is homogeneous, and the frequency is low. High frequencies, high fluid viscosity, and large fractions of clay can violate these assumptions. This theory predicts that the rock's bulk modulus changes with saturation, but the shear modulus remains fixed between dry and saturated rocks. P-waves are sensitive to pore fluids while, except for density, S-waves are not. Gassmann provided this general relation between the dry-rock and saturated-rock moduli.

$$\frac{K_{sat}}{K_{min}-K_{sat}} = \frac{K_{dry}}{K_{min}-K_{dry}} + \frac{K_{fluid}}{\varphi(K_{min}-K_{fluid})}, \quad \frac{1}{\mu_{sat}} = \frac{1}{\mu_{dry}}. \quad (2.18)$$

where,  $K$  is the bulk modulus, and  $\mu$  is the shear modulus. For rocks that are isotropic and homogeneous at low frequencies, Gassmann fluid substitution predicts no change in the shear modulus between dry and saturated rock, allowing this relation to be used to estimate  $K$ . Adam et al. (2006) indicated that Gassmann's theory predicts that the shear modulus will remain constant under different saturations. They also described that Gassmann's relations are low-frequency (seismic) results, and both laboratory and well-log measurements of wave velocities have been observed to deviate markedly from Gassmann's equations at higher (sonic and ultrasonic) frequencies. This is especially so for partial saturation conditions when the fluid in each pore is a mixture of gas and liquid.

In Figure 2.10, x-axes are measured bulk moduli at high frequency from the wellbore and y-axes are theoretically calculated bulk moduli of saturated rocks from dry rocks using Gassmann relation. This figure shows discrepancies between calculated bulk moduli of saturated rocks using Gassmann substitution at low frequency and measured bulk moduli in-situ condition at high frequency. Deviations of data from the solid line can be considered estimates of bulk modulus dispersion related to frequency (Han et al., 1986).

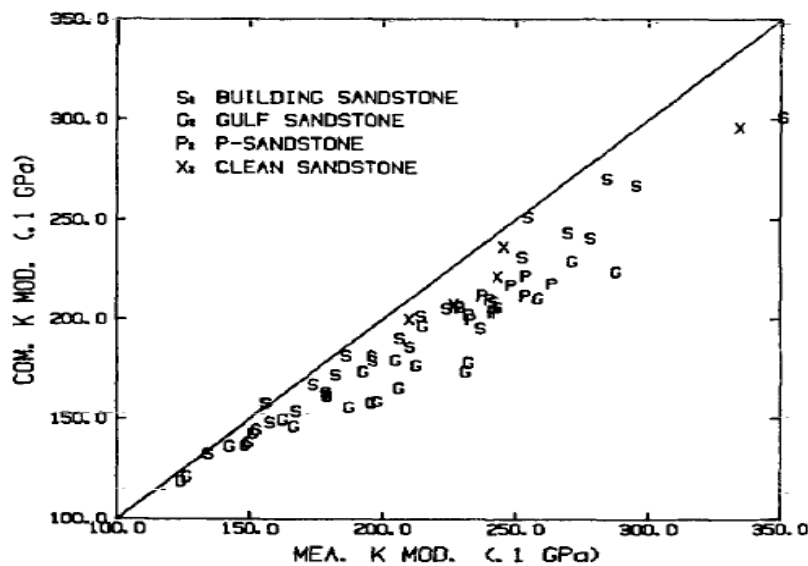


Figure 2.10: The discrepancy (differences between the measured and calculated bulk moduli) of Gassmann fluid substitution. The Gassmann's relations are for low frequencies. As a result, there are differences between calculated velocities of saturated rocks using the low frequency Gassmann equations and velocities measured at high frequency (Han et al., 1986).

Figure 2.11 schematically illustrates the difference of velocities between dry and saturated rock according to the frequencies and the disagreement from the low-frequency Gassmann theory due to frequency-related velocity dispersion. The disagreement between the two typically increases as frequency increases. Due to this discrepancy, to apply ultrasonic core data to field conditions, we need to measure velocities on dry cores,

and then use Gassmann's equations by adding the fluids in the rock to calculate saturated rock velocities. This method assumes that velocity dispersion is smaller for dry rocks, and that the ultrasonic dry velocities are good estimates of low-frequency dry velocities.

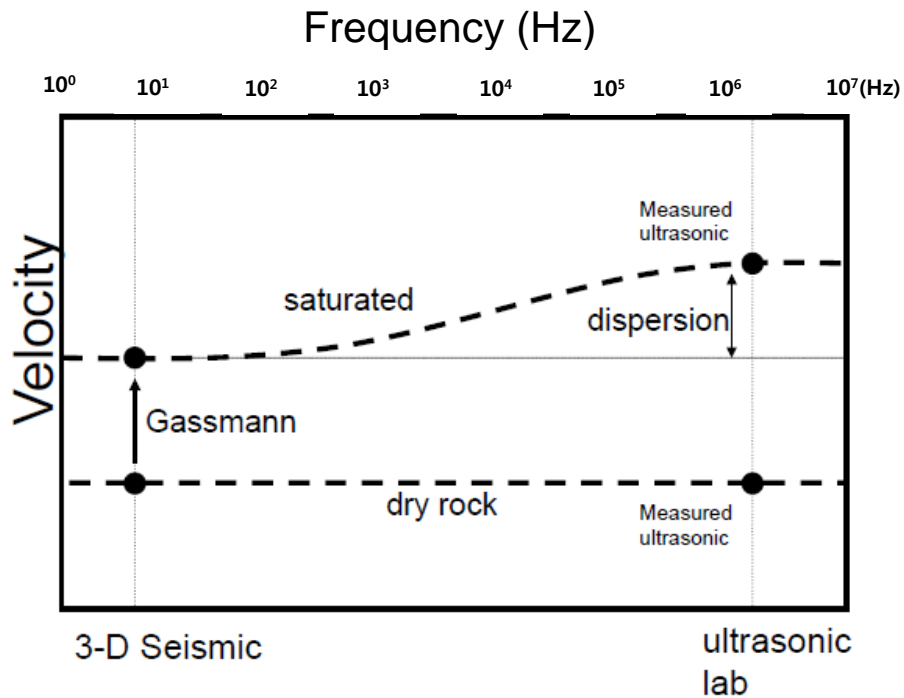


Figure 2.11: Velocity dispersion and frequency.

As the measuring frequency increases, seismic velocities almost always increase in most rocks and sediments such as Fig 2.11. This is known as an inverse dispersion because normal dispersion is defined as a velocity increase with decreasing frequency. However, seismic waves are always attenuated as they travel through the subsurface. Attenuation accompanies this velocity dispersion, and it tends to be highest where the velocity increases most rapidly. When changing from dry- to fluid-saturated rocks, these two effects usually increase and are closely related to the pore fluids moving within the pore space when a high-frequency wave propagates through the rock.

## 2.5 CLOSING STRESS

Pore aspect ratios are also closely related to the closing stress of the pores. The thinnest crack-like pores will close first, followed by larger ones. A pore with a given aspect ratio at a particular depth can be open or closed according to the matrix material and the closing stress. The aspect ratio distribution versus depth allows estimating which depths of pores remain open for an applied stress field. Equation 2.19 gives the relation for the stress ( $\sigma_{close}$ ) needed to close a single isolated pore with aspect ratio ( $\alpha$ ) in an infinite homogeneous matrix with Poisson's ratio ( $\nu_0$ ) and bulk modulus ( $K_0$ ).

$$\sigma_{close} = \frac{3\pi(1-2\nu_0)}{4(1-\nu_0^2)} \alpha K_0 \quad (2.19)$$

Closing stress is plotted as a function of aspect ratio in Figures 2.12 and 2.13. Matrix compositions are quartz (red), clay (green), and average composition data of the Haynesville Shale (blue) in Table 2.1.

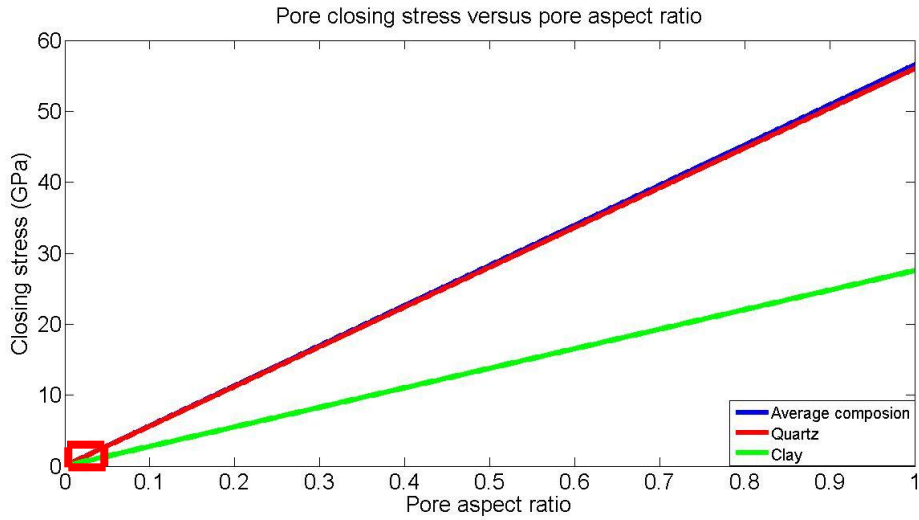


Figure 2.12: The closing stress of a single isolated pore versus various pore aspect ratios. When pore aspect ratio is 1, the closing stress of a single isolated pore with quartz matrix is about 55 GPa. The closing stress with clay matrix is less than 30 GPa, and the closing stress for an average composition of the Haynesville Shale is almost the same pure quartz.

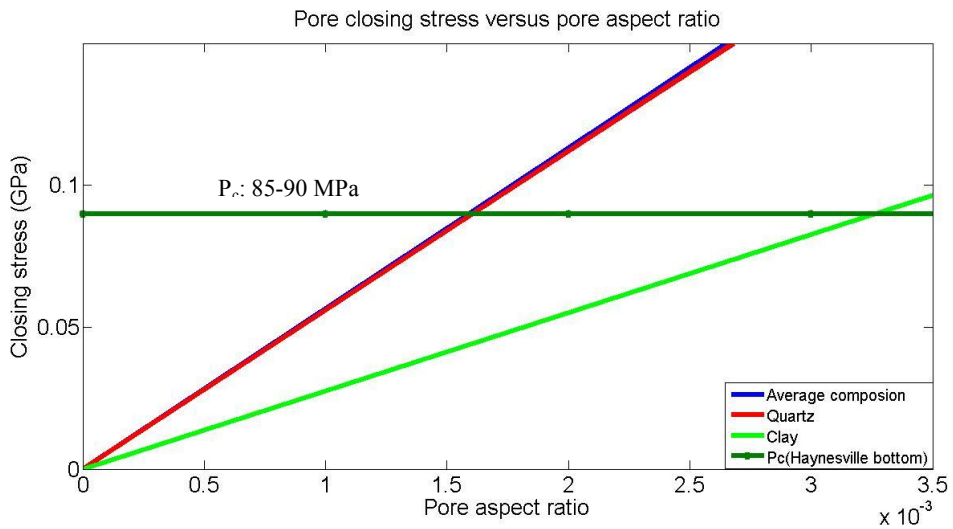


Figure 2.13: Zoom of red zone in Figure 2.12. The closing stress of a single isolated pore versus various pore aspect ratios. At the top and the bottom of the Haynesville Shale, the confining pressure is 85 MPa and 90 MPa, respectively.

The confining pressure of the formation in each depth is calculated by Equation 2.20 (Castagna and Backus, 1993).

$$P_c = \int_{h_0=0}^{h_0} \rho g dh \quad (2.20)$$

The confining pressure of the Haynesville Shale varies from 85 to 90 MPa. For quartz and average composition of the Haynesville Shale, the computed pore aspect ratios that are closed are 0.0015 to 0.0016 at the top and bottom of the Haynesville Shale, respectively. For the clay matrix, closed pores have aspect ratios of 0.0035. The closing stresses are also affected by pore pressure. As pore pressure increases, effective pressure decreases, and pores could be open that have aspect ratios smaller than those predicted by Equation 2.19.

## 2.6 SUMMARY

This chapter described several theories and concepts applied in velocity modeling to determine pore aspect ratios of the Haynesville Shale. Specifically, the self-consistent model was used to model elastic properties. Well data were upscaled to the bandwidth of surface seismic data (20 and 50 Hz) using the Backus average. In addition, the effects of pore fluid mixing on seismic velocities were addressed.

The next chapter explains how the theories presented in Chapter 2 are connected in order to determine aspect ratios by comparing modeled and measured velocities.

## 2.7 REFERENCES

- Adam, L., Batzle, M., and Brevik, I., 2006, Gassmann's fluid substitution and shear modulus variability in carbonates at laboratory seismic and ultrasonic frequencies, *Geophysics*, **71**, 173–183.
- Avseth, P., Mukerji, T., and Mavko, G., 2005, *Quantitative seismic interpretation: applying rock physics tools to reduce interpretation risk*, Cambridge Univ. Press, Cambridge, England.
- Avseth, P., Mukerji, T., Mavko, G., and Dvorkin, J., 2010, Rock-physics diagnostics of depositional texture, diagenetic alterations, and reservoir heterogeneity in high-porosity siliciclastic sediments and rocks - A review of selected models and suggested work flows, *Geophysics*, **75**, 75A31–75A47.
- Backus, G. E., 1962, Long wave elastic anisotropy produced by horizontal layering, *Journal of Geophysical Research*, **67**, 4427-4440.
- Bayuk, I. O., Ammerman, M., and Chesnokov, E. M., 2007, Upscaling of elastic properties of anisotropic sedimentary rocks, *Geophysical Journal International*, **172**, 842-860.
- Berryman, J., 1980, Long-wavelength propagation in composite elastic media I. Spherical inclusions, *Journal of the Acoustical Society of America*, **68**, 1809-1819.

- Berryman, J. G., Berge, P. A., and Bonner, B. P., 1999, Estimating rock porosity and fluid saturation using only seismic velocities, *Stanford Exploration Project*, **102**, 143–157.
- Castagna, J. P. and Backus, M. M., 1993, Offset dependent reflectivity – theory and practice of AVO analysis, SEG, *Investigations in Geophysics Series No. 8*, Tulsa, OK.
- Gassmann, F., 1951, On the elasticity of porous media, *Vier. der Natur. Gesllschft in Zurich*, **96**, 1-23.
- Han, D. H., Nur, A., and Morgan, D., 1986, Effects of porosity and clay content on wave velocities in sandstones, *Geophysics*, **51**, 2093-2107.
- Jensen, E. H., Andersen, C. F., and Johansen, T. A., 2011, Estimation of elastic moduli of mixed porous clay composites, *Geophysics*, **76**, E9-E20.
- Jiang, M and Spikes, K., 2011, Pore-shape and composition effects on rock-physics modeling in the Haynesville Shale, *SEG Expanded Abstracts* **30**, 2079, doi:10.1190/1.3627618.
- Knight, R., and Nolen-Hoeksema, R., 1990, A laboratory study of the dependence of elastic wave velocities on pore scale fluid distribution, *Geophysics*, **17**, 1529-1532.
- Knight, R., 1991, Hysteresis in the electrical resistivity of partially saturated sandstones, *Geophysics*, **56**, 2139-2147.
- Lindsay, R., and Koughnet, R. V., 2001, Sequential Backus Averaging: Upscaling well logs to seismic wavelengths, *The Leading Edge*, **20**, 188-191.
- Longeron, D. G., Argaud, M. J., and Feraud, J. P., 1989, Effect of overburden pressure and the nature and microscopic distribution of fluids on electrical properties of rock samples, *SPE Format. Eval.*, **4**, 194-202.
- Mavko, G., and Mukerji, T., 1998, Bounds on low-frequency seismic velocities in partially saturated rocks, *Geophysics*, **63**, 918-924.
- Mavko, G., Mukerji, T. and Dvorkin, J., 2009, *The rock physics handbook (2nd Edn)*, Cambridge Univ. Press, Cambridge, England.

## Chapter 3: Modeling methodology

Bulk and shear moduli and bulk densities of minerals and fluids were input into the self-consistent model to calculate the modeled velocities. These calculated velocities were compared to the upscaled velocities from the log data in this modeling to estimate pore aspect ratios of the Haynesville Shale. The velocity modeling procedure is described in Chapter 3.2. X-ray Diffraction (XRD) analysis data were used as composition data, and the aspect ratios of mineral grains and pores were also used in the modeling.

### 3.1 INPUT DATA

#### 3.1.1 Elastic property of composition

Bulk moduli, shear moduli, and bulk densities of minerals and fluids used in the self-consistent model in this modeling are summarized in Table 3.1. Elastic properties of pyrite are from Simmons and Birth (1963), and those of kerogen are from Carmichael (1989). The other values for this modeling are used from Mavko et al (2009).

Table 3.1: Elastic properties of minerals and fluids used in this modeling. (Simmons and Birth, 1963; Carmichael, 1989; Mavko et al., 2009).

Component	Bulk modulus (GPa)	Shear modulus (GPa)	Density (g/cc)
Quartz	36.6	45	2.65
Feldspar	37.5	15	2.62
Calcite	69	33	2.71
Dolomite	95	45	2.87
Pyrite	147.3	132.5	4.93
Kerogen	2.9	2.7	1.3
Clay	18	7	2.58
Water	2.8	0	1.09
Gas	0.07	0	0.16

### 3.1.2 Composition data

XRD (X-ray Diffraction) analysis data (48 samples) (Hammes, 2010) versus depth were used to determine pore aspect ratios as component composition data in the modeling. These 48 samples were from depth locations throughout the Haynesville and Bossier Shale, which is the overlying formation of the Haynesville. Twenty eight samples were in the Haynesville shale, and the distance between samples was approximately 10 feet (3.05 m). Figure 3.1 shows composition variation versus depth in the Haynesville and Bossier Shale.

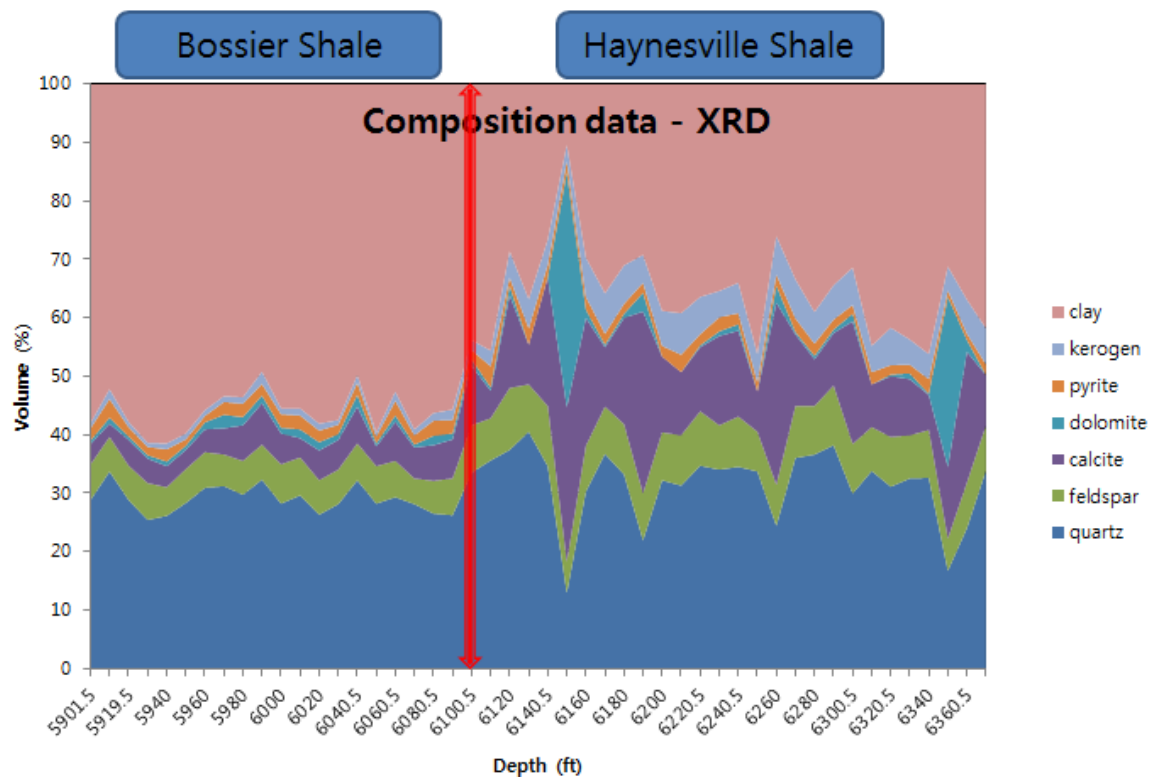


Figure 3.1: XRD composition data for the Haynesville and Bossier Shale, TX. The red line is the limit of two shale formations.

The Haynesville has much less clay and much higher calcite content than the Bossier Shale. The average clay content of the Haynesville is 35.6 % and that of the Bossier is 56.1 %. In addition, kerogen content (average 5.2 %) in the Haynesville is much more than the Bossier Shale (average 1.2 %). Kerogen content from XRD data show that the Haynesville Shale has relatively high TOC values that varies from 1% to 7%. Table 3.2 summarizes composition data of the Haynesville and Bossier Shale, and Figure 3.2 represents this composition in a histogram.

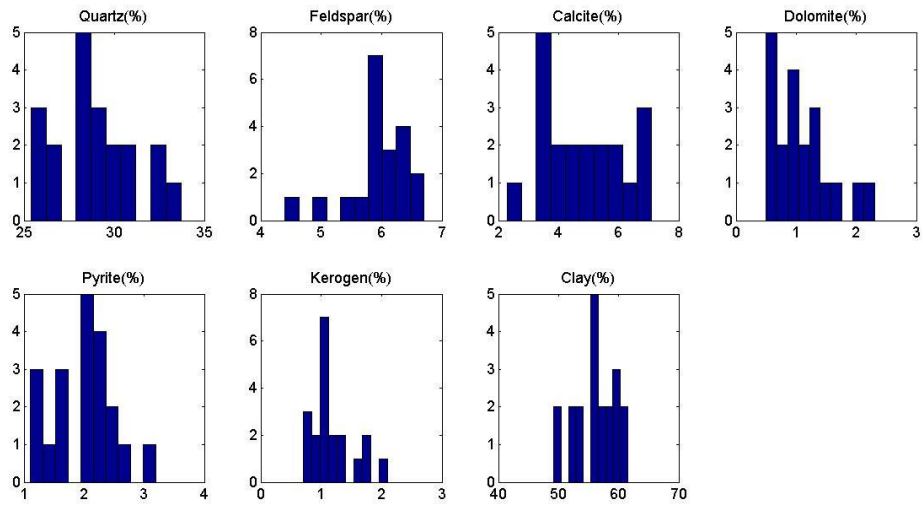
Table 3.2: Comparison of fractional (%) composition data between the Haynesville and the Bossier Shale, TX (Courtesy of Hammes, 2010).

The Haynesville Shale

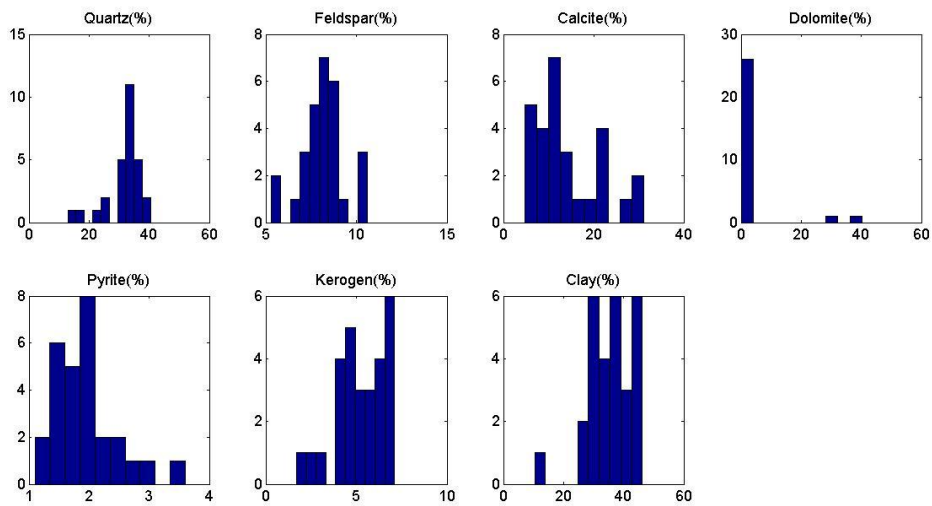
Data	Quartz	Feldspar	Calcite	Dolomite	Pyrite	Kerogen	Clay	Sum
Max	40.5	10.6	31.2	40.2	3.6	7.1	46.2	100
Min	12.9	5.3	4.7	0.0	1.1	1.7	10.4	100
Mean	31.7	8.1	14.2	3.2	2.0	5.2	35.6	100

The Bossier Shale

Data	Quartz	Feldspar	Calcite	Dolomite	Pyrite	Kerogen	Clay	Sum
Max	33.7	6.7	7.1	2.3	3.2	2.1	61.5	100
Min	25.4	4.4	2.3	0.5	1.1	0.7	49.2	100
Mean	28.9	5.9	4.8	1.1	2.0	1.2	56.1	100



(a)



(b)

Figure 3.2: Histograms of mineral percentages for the Haynesville and Bossier Shale, TX. (a) the Bossier Shale (b) the Haynesville Shale. Vertical and horizontal axes are number of samples and fractional composition (%), respectively.

We can see a large difference in volume of clay content between the Haynesville and the Bossier Shale in Figure 3.3. Eastwood and Hammes (2011) indicated that the decrease in volume of clay from the Bossier to the Haynesville may affect the

preservation of kerogen. They also suggested the process of compaction and water expulsion due to considerably smaller clay fractions in the Haynesville must be different from the process of the Bossier Shale and permitted increased amounts of kerogen to survive for the Haynesville. In spite of much less clay and much more calcite contents, P- and S-wave velocities of the Haynesville Shale are slower than those of the Bossier Shale due to the increased kerogen content. Pore aspect ratios are also expected to be larger in the Haynesville Shale compared to those of the Bossier Shale.

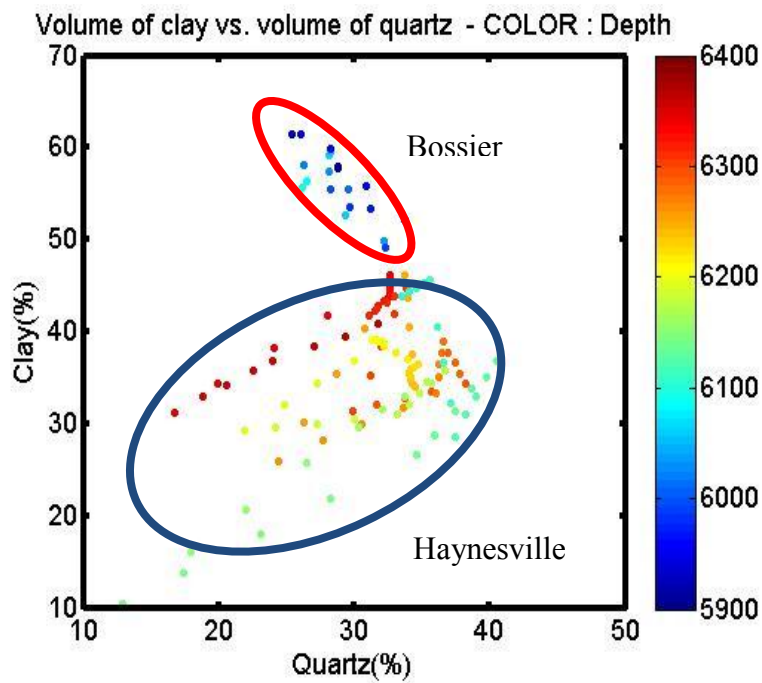


Figure 3.3: Volume of total clay vs. volume of quartz for the Haynesville and Bossier Shale. Data points are colored by depths.

### 3.1.3 Aspect ratio for mineral grains and pores

The self-consistent model requires aspect ratios for both grains and pores. The aspect ratio is the ratio between its longest and shortest axes of mineral grains or pores. The aspect ratios of quartz, feldspar, calcite, dolomite, and pyrite were set to 1. In addition, it was 0.01 for kerogen, and 0.1 for clay (Table 3.3).

Table 3.3: Aspect ratios of minerals used in the modeling.

	Quartz	Feldspar	Calcite	Dolomite	Pyrite	Kerogen	Clay
aspect ratio	1	1	1	1	1	0.01	0.1

Generally, rounded pores that have large aspect ratios increase the stiffness of the pores and overall rocks. Curtis et al. (2010) showed that the pore aspect ratios of the Haynesville Shale, however, are small compared to the other shale formations. Elongated pores that have small aspect ratios such as the Haynesville often lead to slower velocity compared to the rounded pores.

Fifty pore inclusions were assumed in the self-consistent model. These were normally distributed with a variable mean and a standard deviation of 0.01. Using the distribution of aspect ratios in the model allows for calculating a velocity that is a function of multiple pores and multiple minerals. This situation is geologically meaningful because any measured velocity value is a function of the matrix and multiple pores through which the wave travels. Thus, the distribution of modeled pores provides a more realistic scenario. In terms of estimating aspect ratios through comparisons of

modeled and measured velocities, the values reported in this work correspond to the mean value of the normal distribution of aspect ratios.

### 3.2 VELOCITY MODELING FOR PORE SHAPE ESTIMATION

Effective elastic moduli were calculated using the self-consistent model with component composition data and an estimated pore aspect ratio distribution. Mineralogy input in the self-consistent model came from XRD analysis from core (28 composition samples in the Haynesville shale) approximately every 10 feet (3.05 m) in the Haynesville. Using those calculated effective elastic moduli, P-wave and S-wave velocities were calculated at each depth of the formation. P-wave velocities calculated by the self-consistent model were compared to up-scaled P-wave velocities from the moving Backus average instead of the measured log velocities because log-scale measured data can't be seen at the seismic scale. In addition, measured velocities fluctuated significantly versus depth, so it would take much longer time to do this modeling compared to up-scaled velocities. S-wave velocities were not used in this modeling due to inherent uncertainties in both the measurements and model calculations. This comparison method was an iterative, trial and error technique, applied at each depth location in the well. When the difference between the modeled and measured velocity was within 0.5%, the aspect ratio used in the modeling was determined at that location (Figure 3.4). That aspect ratio corresponded to the mean of the input distribution of pore shapes.

After determining the pore aspect ratios for the depths with XRD data, component compositions between depths were interpolated. From the available 28 XRD data approximately 10 feet (3.05 m) interval in depth, I interpolated compositions between the depths, so that composition was estimated every 2.5 ft. As a result, 109 composition data throughout the Haynesville were modeled in total. Then the aspect ratios were estimated for the entire formation using the same procedure. By interpolating composition data between depths, the aspect ratios determined in the modeling became more specific

versus depth than the original values. This helped to understand elastic properties according to the effect of compositions and pore aspect ratios at the seismic scale.

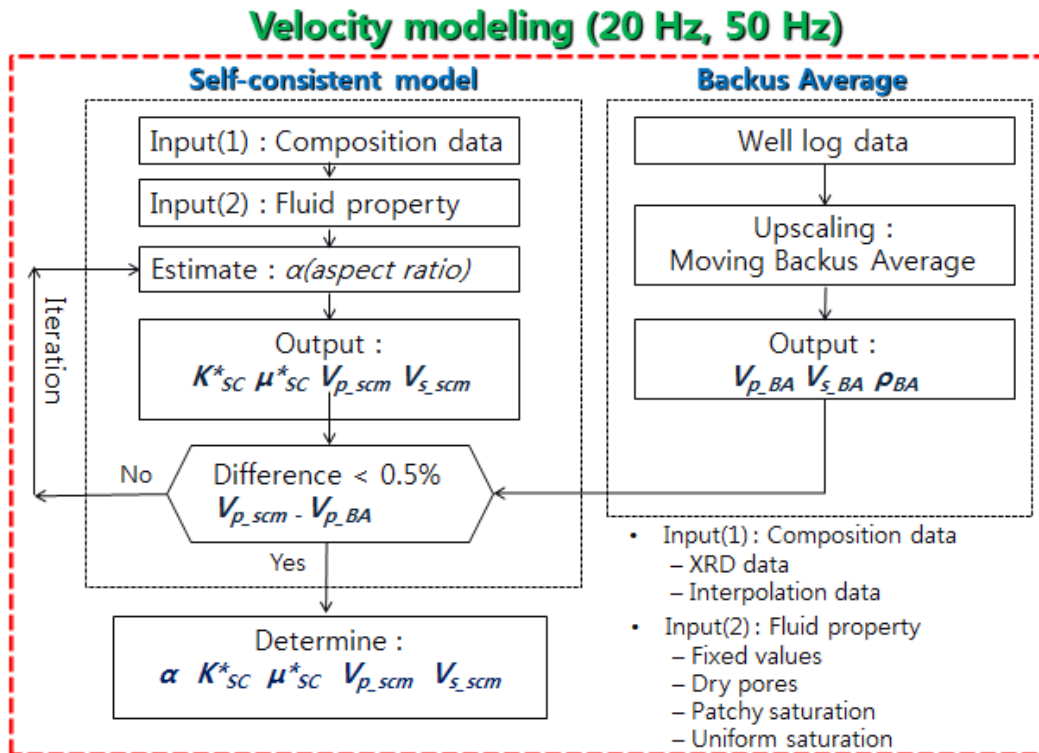


Figure 3.4: Flow chart of velocity modeling to determine the pore aspect ratio of specific depth in the Haynesville Shale. This modeling was performed for the entire depth range at both 20 Hz and 50 Hz. At first, bulk modulus (1 GPa) and density (0.8 g/cc) values for pore fluids were fixed. Partial saturation cases are dealt with in later sections.

The well-log velocity was upscaled to 20 Hz and 50 Hz to determine the dependency of the frequency for the modeling using moving Backus averages. In terms of fluid saturation, first, a single fluid was used at every depth to study only the pore-shape effects. Then the effects of fluid property changes were performed using uniform and patchy fluid saturations in later sections. The results are discussed in Chapter 4.

### 3.3 REFERENCES

- Carmichael, R.S., 1989. Practical Handbook of Physical Properties of Rocks and Minerals, CRC Press, Boca Raton, FL.
- Curtis, M. E., Ambrose, R. J., Sondergeld, C. H., and C. S. Rai, 2010, Structural characterization of gas shales on the micro-and nano-scales: Canadian Society for Unconventional Gas/Society of Petroleum Engineers, DOI: 10.2118/137693-MS.
- Eastwood, R. L., and Hammes, U., 2011, Log model development for the Bossier and Haynesville Shales, SPWLA 52<sup>nd</sup> Annual Logging Symposium, May 14-18, 2011.
- Mavko, G., Mukerji, T. and Dvorkin, J., 2009, The rock physics handbook (2nd Edn), Cambridge Univ. Press, Cambridge, England.
- Simmons, G., and Birch, F., 1963, Elastic constants of pyrite, J. Appl. Phys., **34**, 2736-2738.

## Chapter 4: Modeling Results and Discussion

### 4.1 PORE SHAPE ESTIMATES FOR FIXED FLUID PROPERTIES

The results of the estimated pore aspect ratios for the 20 Hz and 50 Hz cases for the original XRD data and interpolated data described in Chapter 3.2 are shown in Tables 4.1 and 4.2, and Figures 4.1 and 4.2, respectively. In these tables and figures, velocities are in km/s and moduli in GPa. This calculation was carried out for P-wave velocities (within 0.5% differences) with constant fluid elastic properties to minimize the effect of pore fluid change in this section (fluid bulk modulus: 1 GPa, fluid shear modulus: 0 GPa, fluid density: 0.8 g/cc).

Table 4.1: The maximum, minimum and mean values of estimated pore aspect ratios and calculated effective elastic moduli for 20 Hz for the interpolated composition data. From the left, estimated pore aspect ratios, P-wave and S-wave velocities calculated from the Backus average, bulk moduli, shear moduli, P-wave and S-wave velocities calculated from the self-consistent model, differences of P-wave and S-wave velocities between the Backus average and the self-consistent model, respectively.

Pore aspect ratios	Vp_backus	Vs_backus	K_scm	$\mu$ _scm	Vp_scm	Vs_scm	Vp Diff (%)	Vs Diff (%)	
Max	0.320	3.3832	2.0994	16.5155	10.0225	3.3889	2.0213	0.47	8.90
Min	0.029	3.1696	1.8251	12.4748	7.8768	3.1586	1.8540	-0.50	-2.88
Mean	0.144	3.2810	1.9739	13.6729	8.9453	3.2816	1.9398	-0.02	1.67

Table 4.2: The maximum, minimum and mean values of estimated pore aspect ratios and calculated effective elastic moduli for 50 Hz for the interpolated data.

Pore aspect ratios	Vp_backus	Vs_backus	K_scm	$\mu$ _scm	Vp_scm	Vs_scm	Vp Diff (%)	Vs Diff (%)	
Max	0.298	3.5913	2.2410	17.9875	11.4649	3.6039	2.1626	0.46	5.53
Min	0.035	3.1220	1.7933	12.1049	7.6508	3.1221	1.8288	-0.46	-2.66
Mean	0.143	3.2889	1.9744	13.7074	9.0138	3.2887	1.9462	0.01	1.35

Calculated pore aspect ratios from the interpolated data for 20 Hz vary from 0.029 to 0.320 with the mean of 0.144 and the range of pore aspect ratios of the interpolated data for 50 Hz is from 0.035 to 0.298 with the average of 0.143 (Figures 4.1 and 4.2). Compared to the value of aspect ratio for clay (0.1) in Table 3.3, these estimated values for the Hayneville Shale are larger due to the mixture with other components such as quartz, calcite, and so on. The aspect ratios for the two frequencies are similar, but the range of pore aspect ratios for 50 Hz shows a narrower range and a specific variation versus depth than that of 20 Hz. For high frequency (50 Hz) data, P-wave and S-wave velocities show more detailed and distinguishing values versus depth compared to those of 20 Hz.

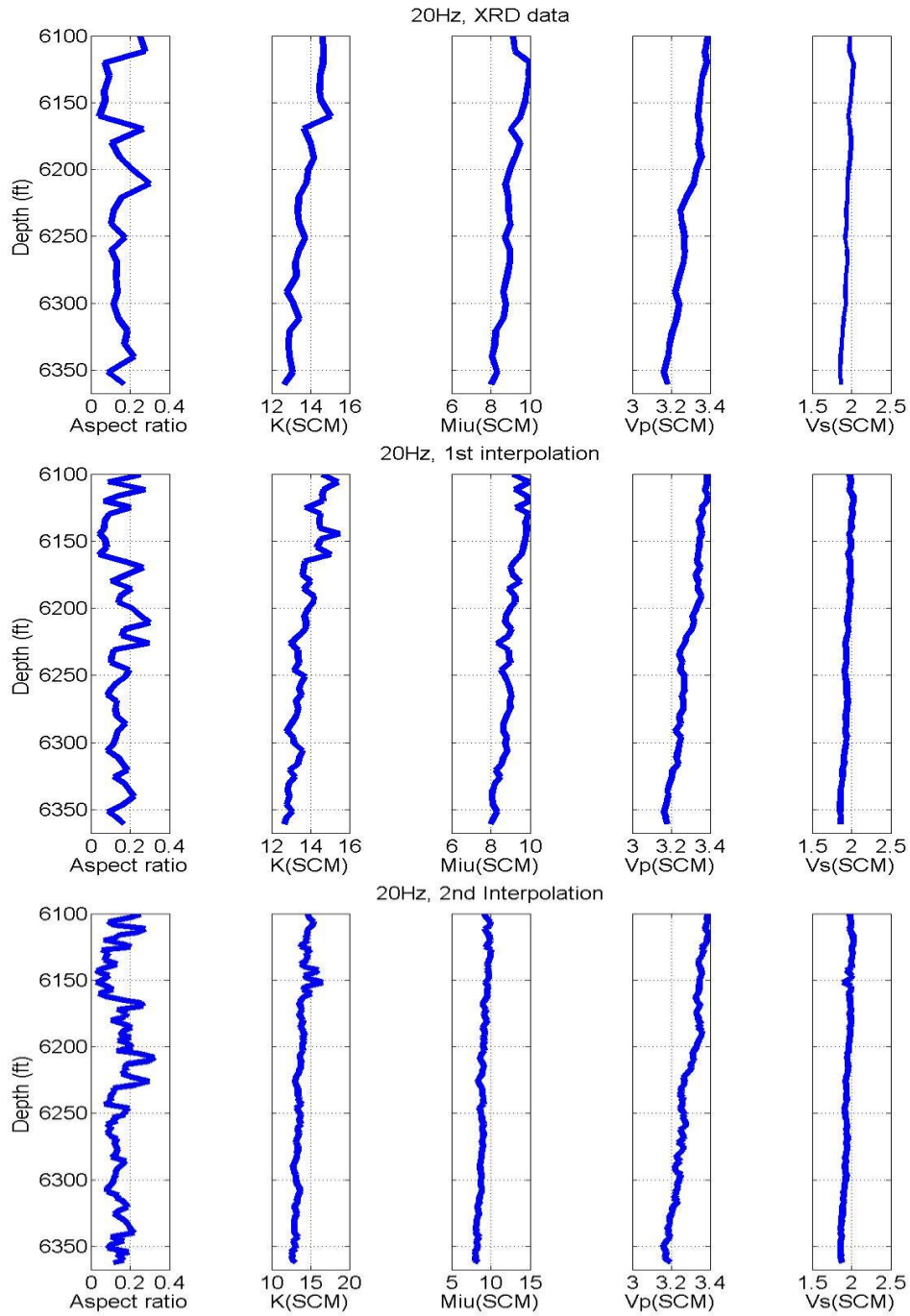


Figure 4.1: Estimated pore aspect ratios for 20 Hz. From the top to bottom, original XRD data, the 1<sup>st</sup> interpolated data, and the 2<sup>nd</sup> interpolated data, respectively. In each Figure, from the left, pore aspect ratios, effective bulk and shear moduli (GPa), effective P-wave and S-wave velocities (km/s) calculated by the self-consistent model.

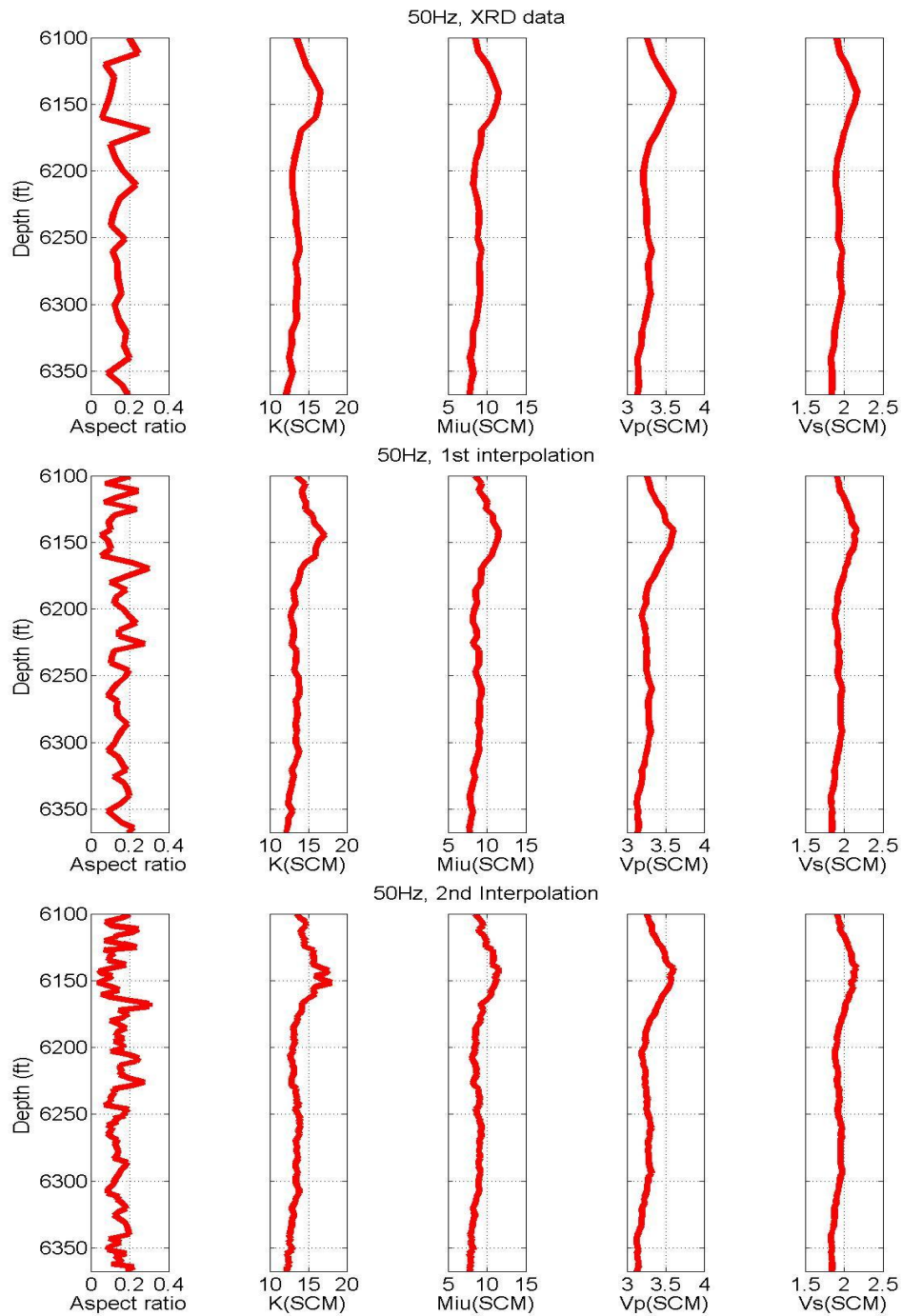


Figure 4.2: Estimated pore aspect ratios for 50 Hz. From the top to bottom, original XRD data, the 1<sup>st</sup> interpolated data, and the 2<sup>nd</sup> interpolated data, respectively. In each Figure, from the left, with the same data set as in Figure 4.1.

The histograms for the interpolated data in Figure 4.3 appear to be normally distributed, but some of the histograms for the original XRD data appear uniformly distributed. This is likely because of central limit theorem. The theorem is that sum of many identically distributed independent random variables tends to be Gaussian distributed, no matter the distributions of the random variables being summed. The histograms of estimated pore aspect ratios, differences of P-wave and S-wave velocities between the Backus average and the self-consistent model for the high frequency (50 Hz) show more detailed and better distribution than those for the low frequency (20 Hz).

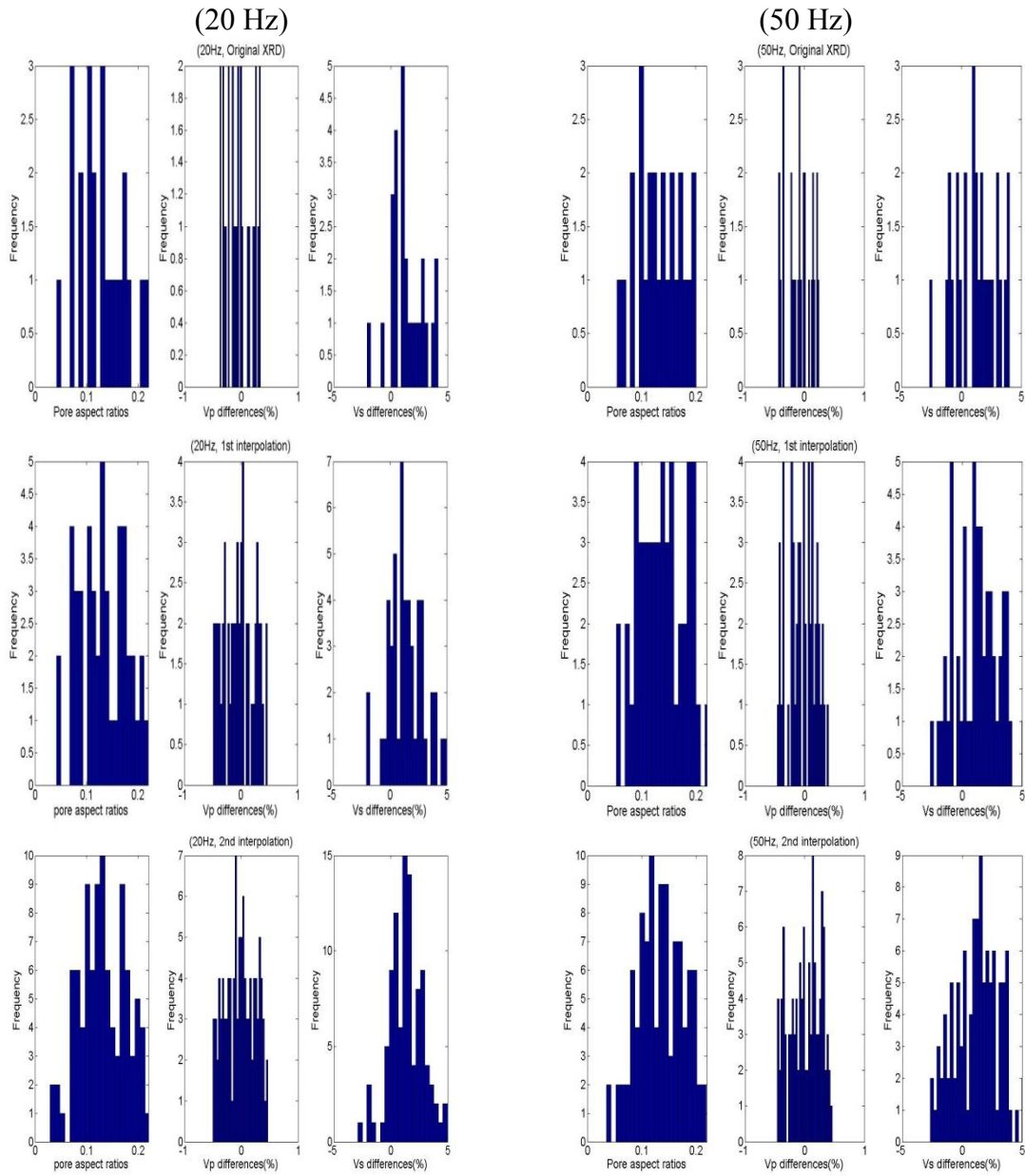


Figure 4.3: The histograms of estimated pore aspect ratios for 20 Hz and 50 Hz. From the top to bottom, original XRD data, the 1<sup>st</sup> interpolated data, and the 2<sup>nd</sup> interpolated data, respectively. The left one is for 20 Hz and the right one is for 50 Hz. In each frame, from the left, pore aspect ratios, differences of P-wave and S-wave velocities between the Backus average and the self-consistent model.

To compare the respective histograms in Figure 4.3, Q-Q plots were generated (Figure 4.4). A Q-Q plot is a plot of the quantiles of two distributions. In statistics, a Q-Q plot is a probability plot, which is a graphical method for comparing two probability distributions by plotting their quantiles against each other (Wilks, 2011). The pattern of points in the plot is a quantitative comparison between the two distributions. If the two distributions being compared are similar, the points in the Q-Q plot will approximately lie on the one-to-one line. A Q-Q plot is generally a more powerful approach to comparing two data distributions than comparing histograms of the two samples.

In addition, correlation coefficients for pore aspect ratios,  $V_p$  and  $V_s$  differences between original XRD data and the 1st interpolated data are 0.9990, 0.8442, and 0.9987, each. Correlation coefficients for pore aspect ratios and  $V_s$  differences between samples are very high. Coefficients for differences in  $V_p$  are lower than those for pore aspect ratios and  $V_s$  differences likely because P-wave velocities for the XRD data are uniformly distributed whereas the P-wave velocities for the first interpolation are normally distributed (Figure 4.3). However, correlation coefficients between original XRD data and the 2nd interpolated data are 0.9987, 0.9545, and 0.9985, each. All three coefficients show that it is well correlated between original XRD data and the 2nd interpolation data for pore aspect ratios,  $V_p$  and  $V_s$  differences. From the results of Q-Q plots and correlation coefficients, it is possible to argue that the pore shapes from the 2nd interpolated data have similar distributions to the original XRD data.

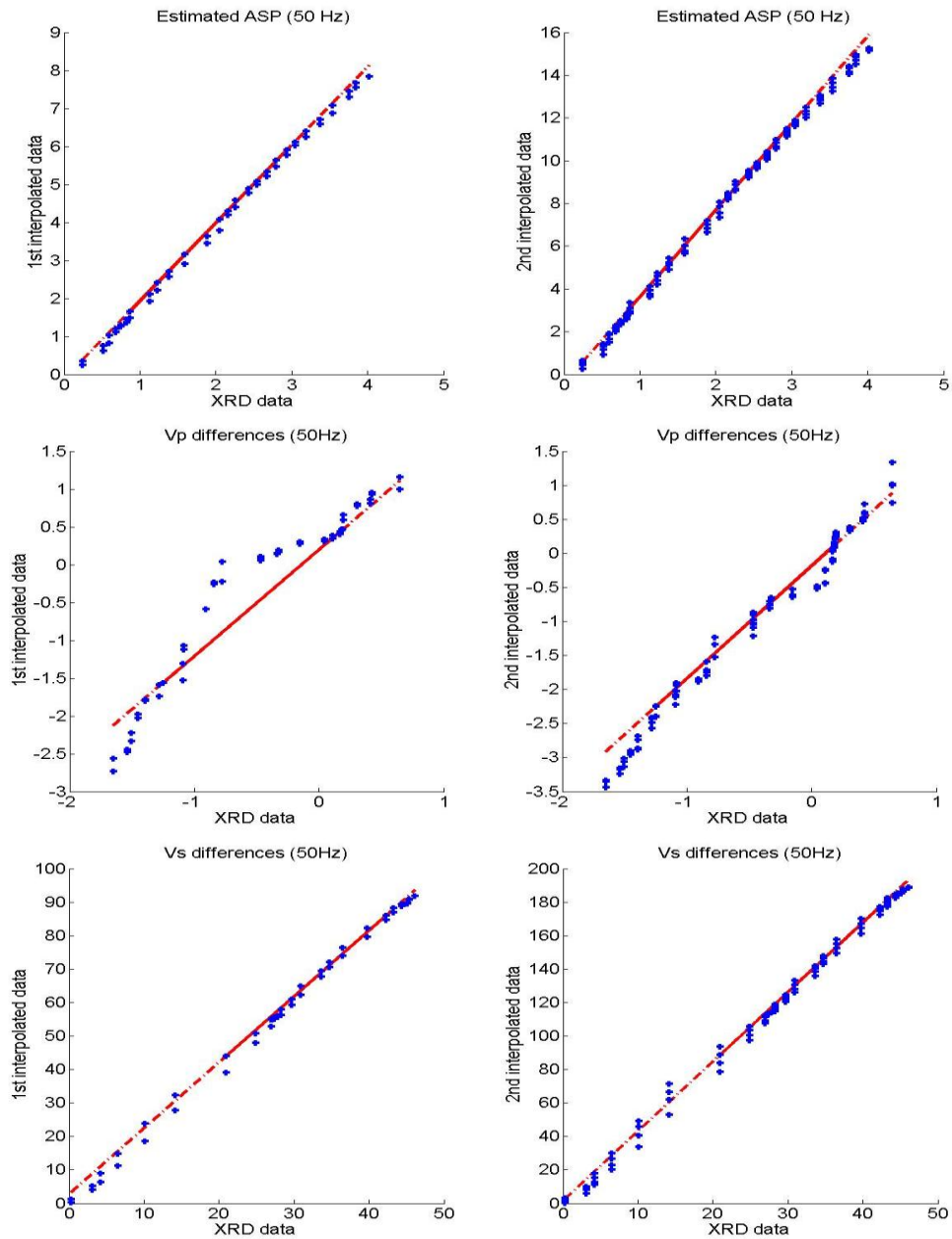


Figure 4.4: The Q-Q plots between original XRD data and interpolated data from the velocity modeling for 50 Hz. Left figure is the Q-Q plot between original XRD and 1st interpolated data, and right one is between original XRD and 2nd interpolated data. From top to bottom in each column, the Q-Q plots are for pore aspect ratios, differences of P-wave and S-wave velocities between the self-consistent model and the Backus average are plotted.

Figure 4.5 is comparison of estimated pore aspect ratios for 20 Hz and 50 Hz for both XRD data and interpolated data. The more increased numbers of data points, the better representing the change of specific pore aspect ratio versus depth. Pore aspect ratios estimated (0.035-0.298) from the high-frequency case show a narrower range and more detailed and specific values versus depth than those (0.029-0.320) from the low-frequency for the interpolated data.

For average composition of the Haynesville Shale, the calculated pore aspect ratios that are closed were 0.0015 to 0.0016 at the top and bottom of the Haynesville Shale, respectively (Chapter 2.5). Comparing these values to the estimated pore aspect ratios of the interpolated data for 50 Hz (0.035-0.298) in this modeling, the Haynesville Shale appears to have pores that are open regardless of the pore pressure and in-situ stress in the formation.

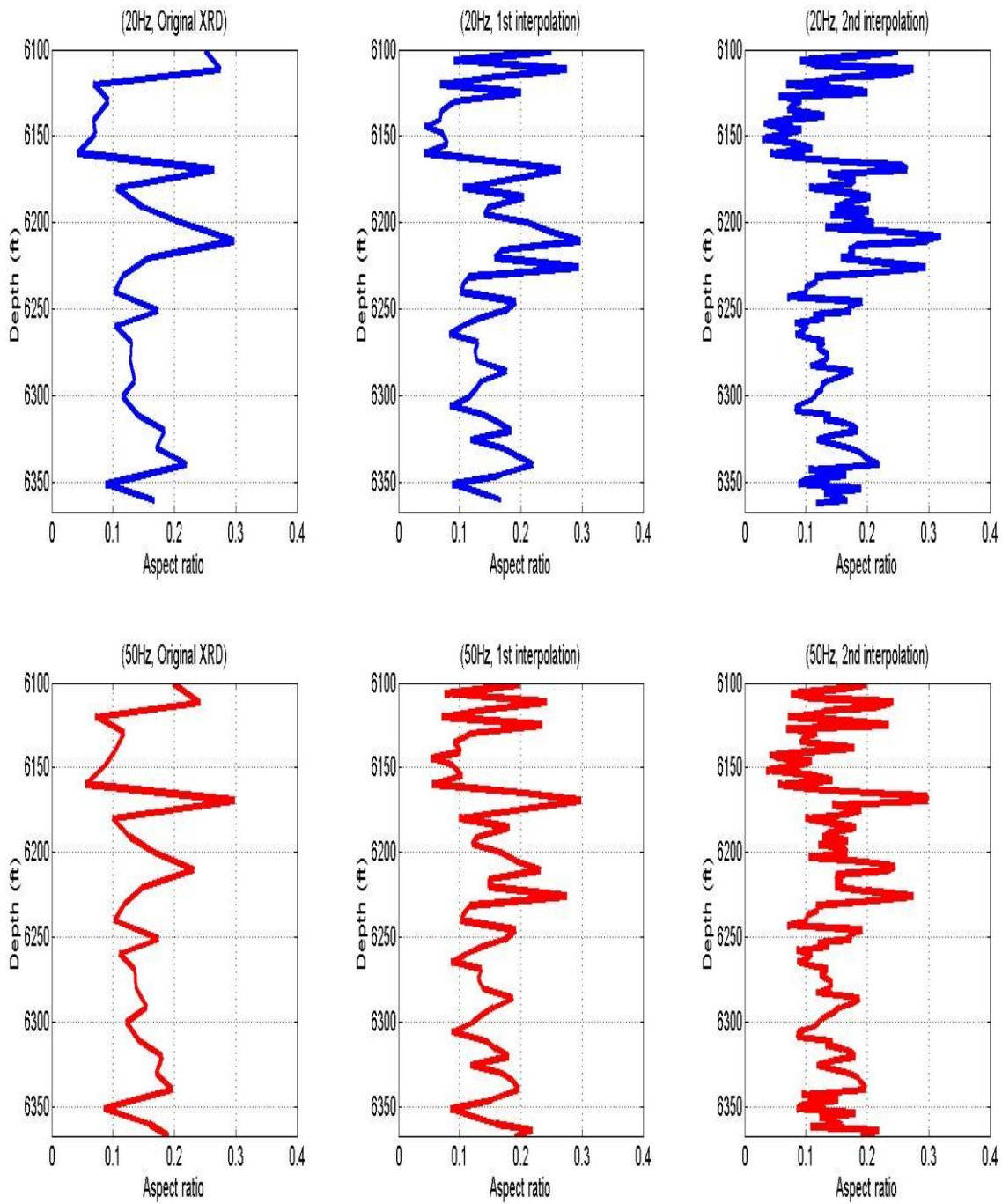


Figure 4.5: Comparisons of estimated pore aspect ratios for 20 Hz and 50 Hz. The upper figure is calculated for 20 Hz and the bottom one is for 50 Hz. In each figure, from the left, pore aspect ratios calculated from original XRD data, 1<sup>st</sup> interpolated data, and 2<sup>nd</sup> interpolated data, respectively.

## **4.2 THE EFFECTS OF FLUID PROPERTY CHANGES TO VELOCITIES**

In the preceding section, I estimated pore aspect ratios at constant fluid properties in the Haynesville Shale at both 20 Hz and 50 Hz. This minimized the effect of variable pore fluid, allowing for estimates of pore shape, independent of the fluid. This section (4.2) describes how seismic velocities and thus pore-shape estimates are affected by pore-fluid properties. In this analysis, I used the original XRD mineral composition data and estimated pore aspect ratios at 50 Hz. To analyze the fluid effect, I performed simulations for five cases, which are 1) the dry pores, 2) patchy saturation, and 3) uniform saturation cases for the self-consistent model. Fluid substitution was performed on the dry rock moduli generated from the self-consistent model to 4) uniform- and 5) patchy-saturation cases. By comparing the differences of P-wave velocities calculated for these cases, we can better understand the effect of fluid-property changes on pore shape estimates in the Haynesville shale.

### **4.2.1 Water saturation**

To analyze the effects of pore-fluid properties, including patchy and uniform saturation, we need to use water saturation data from the well log that were calculated by Archie's (1942) equation. Archie's equation is used to calculate water saturation in clean sandstone formations, so there might be errors in water saturation in the shale formation. Even though using water saturation calculated by Archie's equation as input data in this simulation, it is assumed acceptable to analyze the effect of fluid property changes.

Figure 4.6 is the well log data of the whole range of the well for density porosity (fraction), water saturation (fraction), and volume of illite (fraction). There is a drastic change of volume clay content at the top of the Haynesville Shale relative to the overlying formation (the Bossier Shale). The water saturation for the Haynesville Shale varies from 0.0819 to 0.7020 with mean of 0.2462 from the well log. The clay content of the Haynesville is almost constant throughout the formation except the top section (average 35.6 %). The top section of the Haynesville Shale has higher porosity and water saturation values compared to other sections.

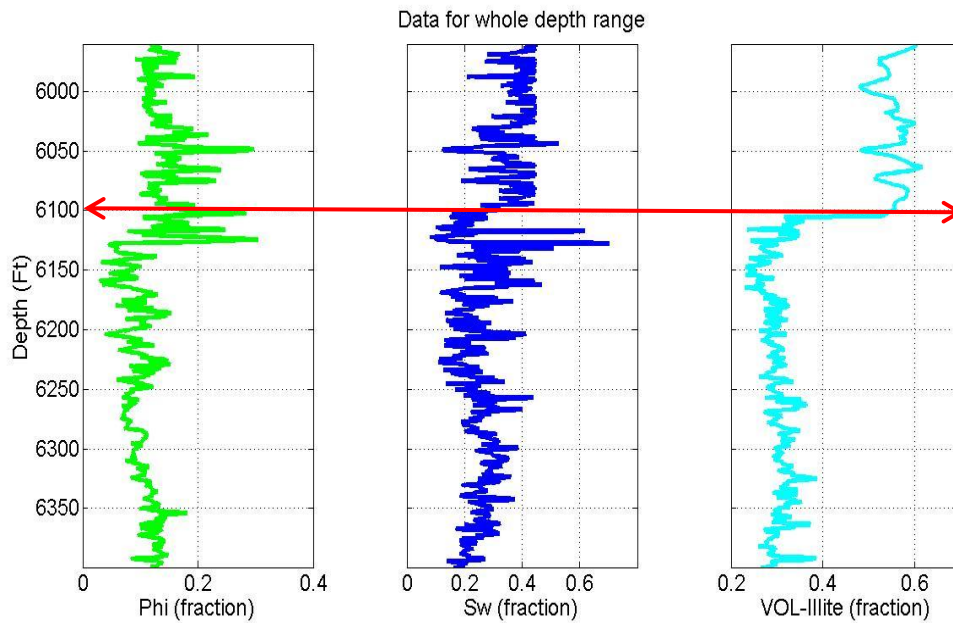


Figure 4.6: Well log data of the whole range of the well. From the left, density porosity (fraction), water saturation (fraction), and volume of illite (fraction) are plotted versus depth. Haynesville Shale is below red arrow in this Figure. There is a large drop of volume clay content at the top of the Haynesville Shale (6,100 ft.) relative to the overlying formation.

## 4.2.2 Patchy and uniform saturation

Pore-scale fluid distribution is important in the interpretation of the bulk elastic properties from partially saturated rocks. It means that elastic velocities can be significantly affected by the pore scale mixing of fluids. The patchy and uniform saturation curves are upper and lower bounds, respectively, in terms of fluid-mixing scales. By using water saturation data, bulk moduli and densities for both patchy saturation and uniform saturation cases can be calculated (Equations 2.16 and 2.17). Figure 4.7 and Table 4.3 show bulk moduli and densities for both cases and constant (fixed) values used in the velocity modeling to estimate pore aspect ratios in Chapter 3.

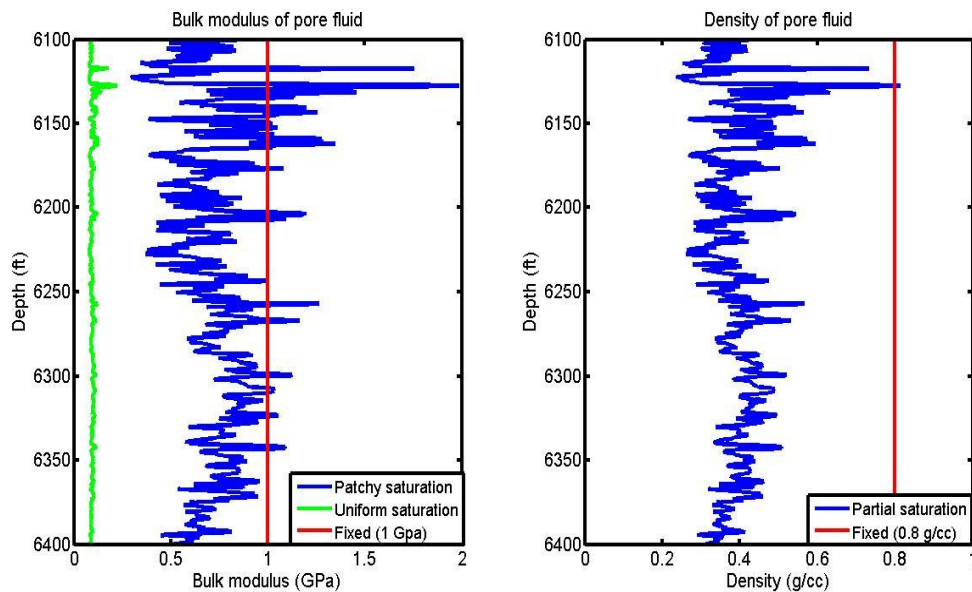


Figure 4.7: Bulk moduli ( $K_f$ ) and densities ( $\rho_f$ ) of fluids for patchy saturation, uniform saturation and fixed fluid values ( $K_f=1$  GPa,  $\rho_f=0.8$  g/cc for fluids) versus depth. Blue is for patchy saturation. Green is for uniform saturation. The red line is for the fixed value of fluids for the velocity modeling.

Table 4.3: Calculated maximum, minimum and mean values of bulk moduli and densities of fluids for fixed fluid, the patchy and uniform saturation.

Pore fluid properties	Fixed	Patchy saturation			Uniform saturation		
		Max	Mean	Min	Max	Mean	Min
Bulk modulus(GPa)	1	1.9866	0.7421	0.2936	0.2219	0.0932	0.0761
Density(g/cc)	0.8	0.8129	0.3889	0.2362	0.8129	0.3889	0.2362

In Chapters 4.2.3 and 4.2.4., effective moduli, P-wave and S-wave velocities in the Haynesville shale were calculated using both the self-consistent model and Gassmann fluid substitution for the saturated-rocks to analyze the pore-fluid effect to velocities.

### **4.2.3 Velocity comparison by SCM for various types of fluid distributions**

By setting bulk moduli and densities for pore fluids to zero within the self-consistent model, elastic moduli and velocities were calculated for dry rocks. A distribution of pore aspect ratios was included with a variable mean and standard deviation 0.01. In addition, effective moduli and velocities by including fluid directly into the dry rock in the self-consistent model were computed for the patchy and uniform saturation cases.

Patchy saturation cases have the largest values for bulk moduli, shear moduli, and P-wave velocities, as expected. Values for dry rock are the smallest and moduli for uniformly mixed fluids are in between them (Figure 4.8 and Table 4.4). Contrary to that, for the S-wave velocities, patchy saturation values are the largest, then, dry pore values, and uniform saturation values are the smallest at some depths. The reason that S-wave velocities of dry pore cases are larger than those of uniform saturation cases is because of the density effect in S-wave velocities. Bulk moduli and P-wave velocity graphs show similar patterns, and shear moduli and S-wave velocity graphs also show similar patterns in Figure 4.8. Comparing P-wave velocities and bulk moduli of patchy saturation to uniform saturation demonstrates patchy saturation values are much higher than uniform saturation values. This is not the case for S-wave velocities and shear moduli.

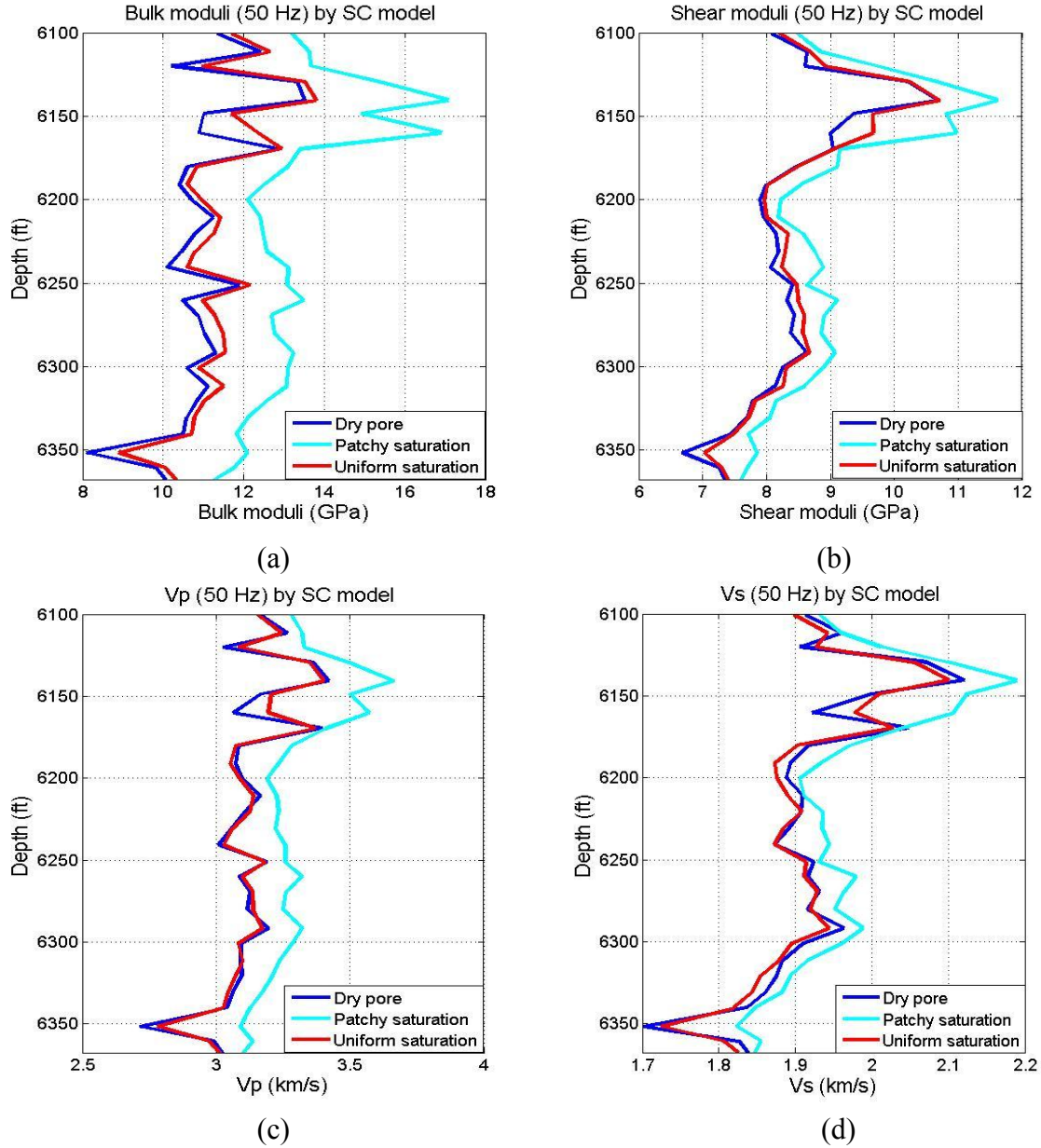


Figure 4.8: Graphs of (a) bulk moduli, (b) shear moduli (c) P-wave velocities, and (d) S-wave velocities for dry pores, the patchy and uniform saturation calculated by the self-consistent model for the Haynesville shale. Shear moduli and S-wave velocities for saturated cases are different from those of dry cases because the self-consistent model is a high-frequency model. Values between the patchy and uniform saturation are also different due to the effect of partial saturation in both moduli and velocities. Each case corresponds to the same normal distribution of pore aspect ratios.

Table 4.4: Bulk and shear moduli, P-wave and S-wave velocities calculated by the self-consistent model for dry pores, fixed fluids, the patchy and uniform saturation.

	Dry pores				Fixed pore fluid			
	$K_{scm}$	$\mu_{scm}$	$Vp_{scm}$	$Vs_{scm}$	$K_{scm}$	$\mu_{scm}$	$Vp_{scm}$	$Vs_{scm}$
Max	13.4989	10.6731	3.4186	2.1209	16.5518	11.4649	3.6039	2.1626
Min	8.1000	6.6758	2.7150	1.7013	12.1164	7.7762	3.1272	1.8288
Mean	10.9584	8.3225	3.1169	1.9142	13.6900	9.0079	3.2880	1.9459
	Patchy saturation				Uniform saturation			
	$K_{scm}$	$\mu_{scm}$	$Vp_{scm}$	$Vs_{scm}$	$K_{scm}$	$\mu_{scm}$	$Vp_{scm}$	$Vs_{scm}$
Max	17.0726	11.6240	3.6640	2.1889	13.7924	10.7088	3.4015	2.1009
Min	11.2519	7.5901	3.0891	1.8228	8.9007	7.0263	2.7802	1.7242
Mean	13.1894	8.9143	3.2847	1.9581	11.3395	8.4494	3.1206	1.9073

When going from a dry- to fluid-saturated rock, the elastic bulk modulus of rock increases, and the bulk density also increases. However, the shear modulus of rock depends on the frequency of the model used. At low frequencies, the shear moduli of dry- and fluid-saturated rock are the same according to Gassmann's relation. However, in inclusion-based models such as the self-consistent model, the shear modulus of fluid-saturated rock increases with saturation changes compared to that of dry rock because the elastic-stiffening effect is exaggerated for both bulk and shear moduli. Velocities depend on the ratio of elastic moduli to density. According to the values of modulus and density, the velocities could increase or decrease. For the self-consistent approximation, local pore pressures increase in some pores and decreases in others. This lack of hydraulic

communication prevents pore pressure equilibration. Therefore, the moduli and velocities increase as frequency increases (frequency dispersion).

Histograms in Figure 4.9 show the frequencies of occurrence distribution of P-wave and S-wave velocities of dry pores, fixed fluids, the patchy and uniform saturations calculated by self-consistent model. These histograms make it easier to differentiate the differences between calculated P-wave and S-wave velocities for the various types of fluid mixtures. Patchy saturation cases have the largest values in both P-wave and S-wave velocities. However, in cases of uniform saturation cases and dry pores, results are different between two velocities as already described.

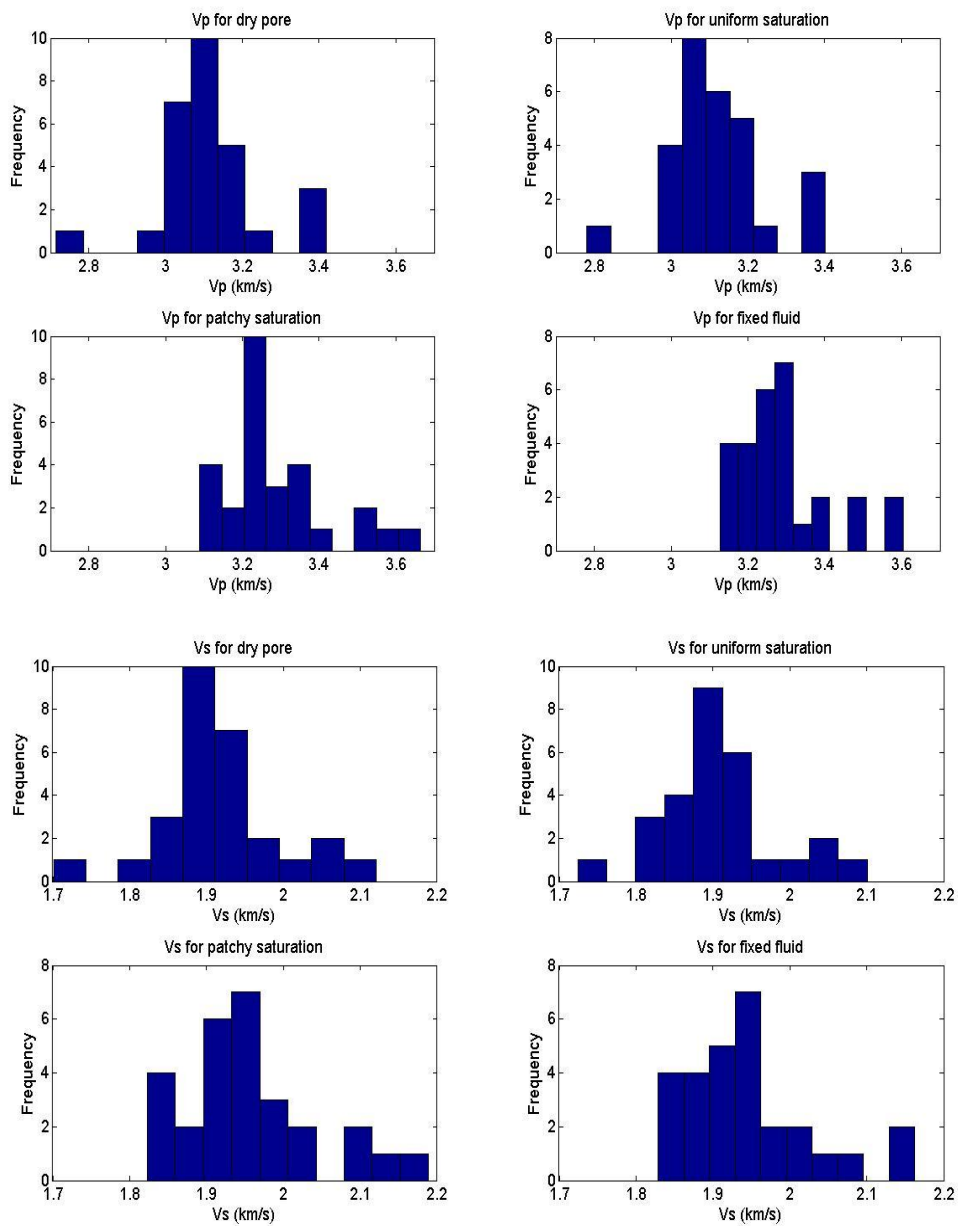


Figure 4.9: Histograms of P-wave and S- wave velocities for dry pores, fixed fluid, the patchy and uniform saturation calculated by the self-consistent model for the Haynesville shale.

#### **4.2.4 Velocity comparison by Gassmann substitution for various types of fluids**

Gassmann fluid substitution allows us to obtain the bulk and shear moduli of the fluid-saturated rock from the dry rock frame moduli, porosity, and fluid (bulk) modulus with the assumption of isotropic, homogeneous rock and the low frequency case. Using Gassmann fluid substitution, I calculated P-wave and S-wave velocities for both the patchy and uniform saturation cases where the dry rock moduli were calculated from the self-consistent model. Before using Gassmann substitution, knowing the effective mineral moduli was necessary to study pore fluid effects. According to Jensen et al. (2011), a common strategy is to use the Hill average (Hill, 1963), which is the average of the Voigt bound and Reuss bound to obtain the effective solid properties.

In inclusion-based models such as the self-consistent model, the moduli and velocities increase as frequency increases (frequency dispersion) because those models are appropriate for high-frequency model. The Biot (global flow) and squirt flow (local flow) also describe the viscoelastic behavior of the rock when pore-pressure gradients are unrelaxed at high frequencies. However, it is assumed acceptable to analyze frequency-related velocity dispersion using the self-consistent model instead of the Biot and squirt flow in this thesis. Contrary to the high-frequency models, the shear moduli of dry- and fluid-saturated rock are the same at low frequencies according to Gassmann's relation. This disagreement between the two methods typically increases as frequency of the propagating waves increases. To analyze differences of velocities between the low-frequency Gassmann relations and the high-frequency self-consistent model for various types of fluid properties, velocity results calculated using Gassmann relations were dealt with in this section.

Patchy saturation cases have the largest values for P-wave velocities calculated by Gassmann fluid substitution. Contrary to that, for the S-wave velocities, dry pore values are the largest, and the patchy and uniform saturation values are the same because Gassmann fluid substitution assumes shear modulus of fluid is zero (Figure 4.10 and Table 4.5). Adam et al. (2006) also indicated that Gassmann's theory predicts that the shear modulus will remain constant under different saturations. The reason that S-wave velocities of dry pore cases are larger than those of the patchy and uniform saturation cases is also the density effect in S-wave velocities. Very little difference exists for S-wave velocities of the dry cases versus the patchy and uniform saturation cases.

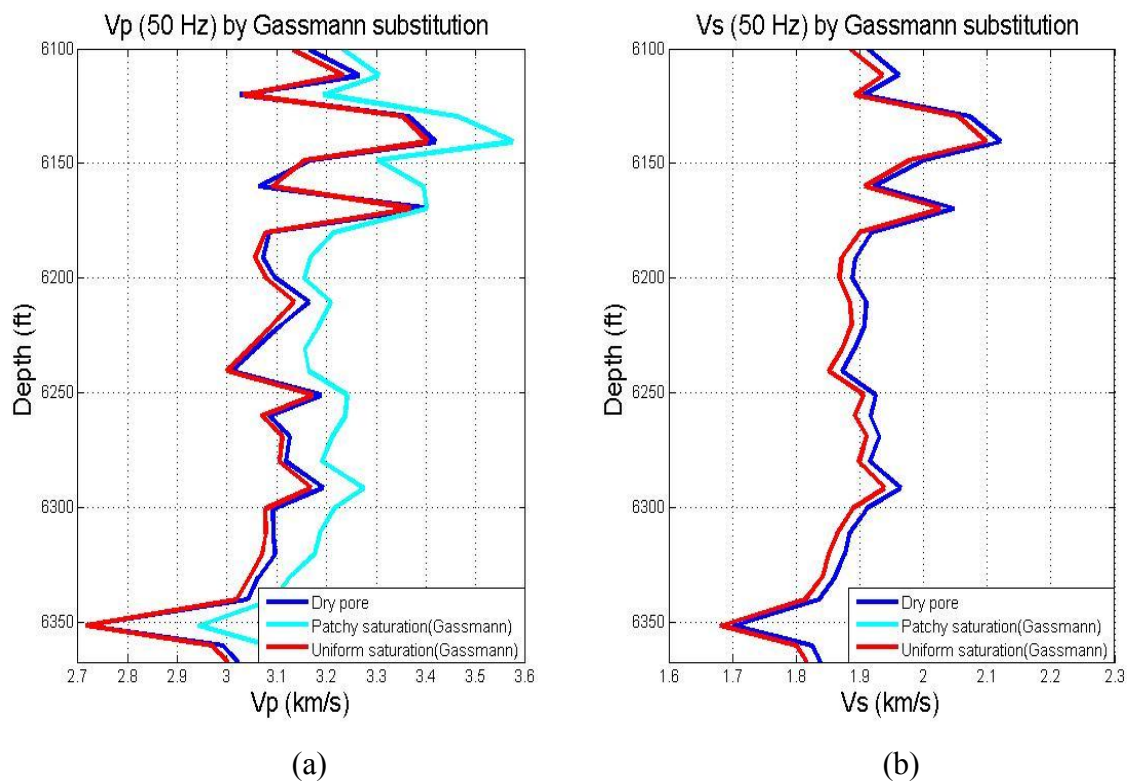


Figure 4.10: Graphs of (a) P-wave velocities and (b) S-wave velocities for dry pores, the patchy and uniform saturation calculated by Gassmann fluid substitution for the Haynesville Shale. As expected, S-wave velocities for the patchy and uniform saturation cases are the same in (b).

Table 4.5: Bulk and shear moduli, P-wave and S-wave velocities calculated using by Gassmann fluid substitution for the patchy and uniform saturation cases.

	Patchy saturation				Uniform saturation			
	K_gass	$\mu_{gass}$	Vp_gass	Vs_gass	K_gass	$\mu_{gass}$	Vp_gass	Vs_gass
Max	16.7715	10.6731	3.5746	2.0974	16.7715	10.6731	3.4033	2.0974
Min	11.1999	6.6758	2.9416	1.6806	11.1999	6.6758	2.7161	1.6806
Mean	12.9799	8.3225	3.2199	1.8931	12.9799	8.3225	3.1014	1.8931

Histograms in Figure 4.11 show the frequencies of occurrence of P-wave and S-wave velocities of dry pores, fixed fluids calculated by the self-consistent model, the patchy and uniform saturation calculated by Gassmann fluid substitution. Patchy saturation cases have larger values in both P-wave and S- wave velocities than those of uniform saturation cases. S-wave velocities for the patchy and uniform saturation cases are the same as already described.

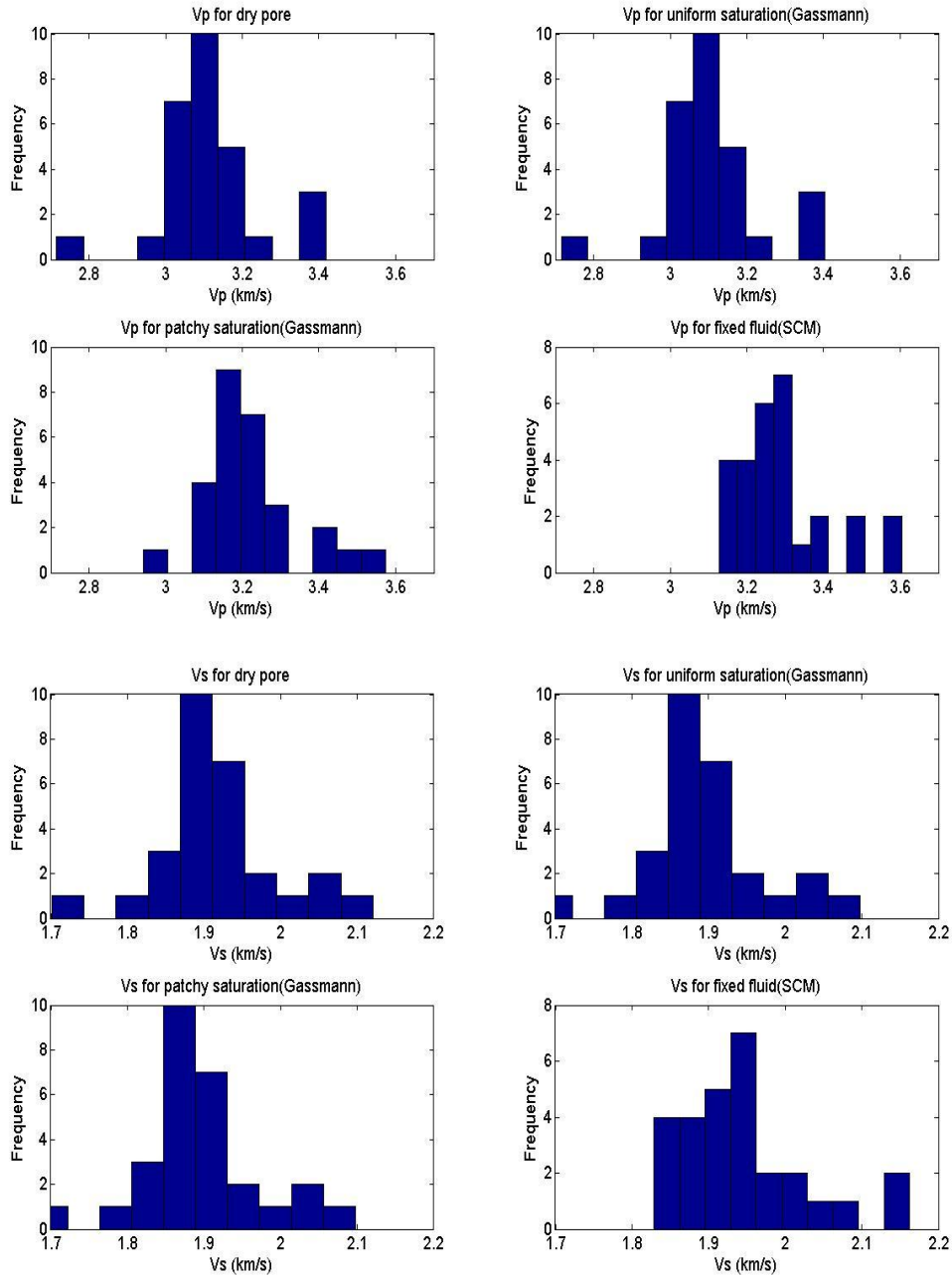


Figure 4.11: Histograms of P-wave and S- wave velocities for dry pores and fixed fluid calculated by the self-consistent model, the patchy and uniform saturation calculated by Gassmann fluid substitution for the Haynesville shale.

#### **4.2.5 Velocity Comparison between the self-consistent model and Gassmann fluid substitution**

The self-consistent model calculates the effective elastic properties of rocks with multi-component minerals and various fluid-saturation cases by inputting elastic properties into the model directly. The pore inclusions in the self-consistent model are isolated with respect to fluid flow. Therefore, this model is appropriate for high frequency modeling of data. Gassmann fluid substitution makes it possible to calculate the bulk and shear moduli of the fluid-saturated rock from the dry rock moduli at low frequency. Gassmann fluid substitution predicts that the rock's total bulk modulus changes with saturation but the shear modulus does not. Therefore, P-waves are sensitive to pore fluids whereas S-waves are not except for density.

For patchy saturation cases, P-wave velocities from the self-consistent model are larger than the values from Gassmann fluid substitution, and the differences decrease in S-wave velocities in Table 4.6, Figures 4.12 and 4.13. For uniform saturation cases, the differences of P-wave and S-wave velocities are very small. Because the self-consistent model is a high- frequency model, P-wave velocities from the model for the saturated rock should be different from P-wave velocities from Gassmann fluid substitution. These velocities for various types of fluid mixing in Figures 4.12 and 4.13 were calculated using pore aspect ratios determined from the upscaled velocities in the modeling. Comparing these values to both the measured (observed) velocities from the well log and upscaled velocities from the Backus average, patchy saturation cases of P-wave and S-wave velocities from the self-consistent model best represent the measured data at the upscaled scale compared to other types of fluid mixing.

Table 4.6: Comparison of bulk and shear moduli, P-wave and S-wave velocities calculated by both the self-consistent model and Gassmann substitution for dry pores, fixed fluids, the patchy and uniform saturation.

	$K$	$\mu$	$V_p$	$V_s$	$K$	$\mu$	$V_p$	$V_s$
	Dry pores (SCM)				Fixed pore fluid (SCM)			
Mean	10.9584	8.3225	3.1169	1.9142	13.6900	9.0079	3.2880	1.9459
	Patchy saturation (SCM)				Uniform saturation (SCM)			
Mean	13.1894	8.9143	3.2847	1.9581	11.3395	8.4494	3.1206	1.9073
	Patchy saturation (Gassmann)				Uniform saturation (Gassmann)			
Mean	12.9799	8.3225	3.2199	1.8931	12.9799	8.3225	3.1014	1.8931

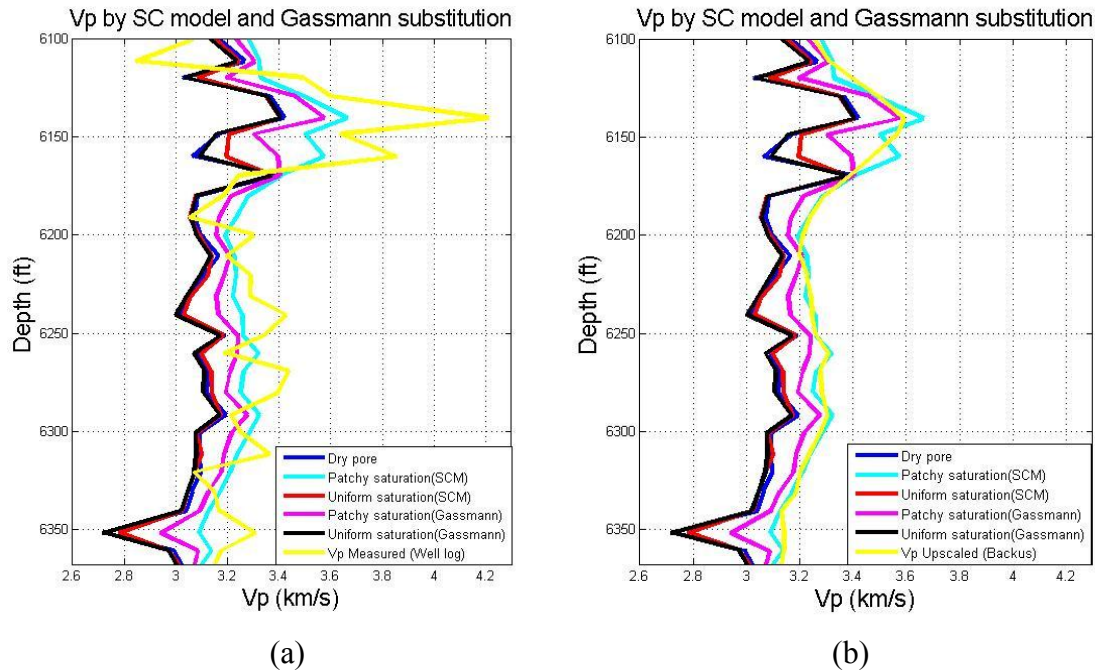


Figure 4.12: Comparison of P-wave velocities for dry pores, the patchy and uniform saturation calculated by the self-consistent model and from Gassmann fluid substitution for the Haynesville shale. Yellow line is (a) the measured data from the well log and (b) the upscaled data from the Backus average. Patchy saturation values of P-wave velocities from the self-consistent model best represent the measured data at the upscaled scale.

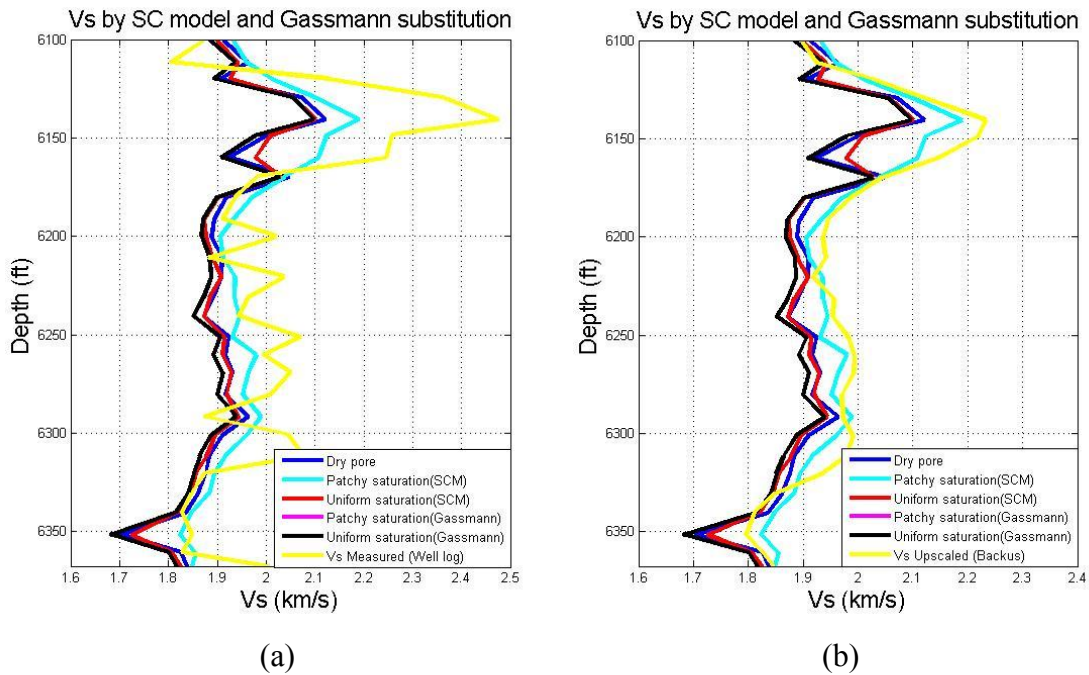


Figure 4.13: Comparison of S-wave velocities for dry pores, the patchy and uniform saturation calculated by the self-consistent model and from Gassmann fluid substitution for the Haynesville shale. Yellow line is (a) the measured data from the well log and (b) the upscaled data from the Backus average. Patchy saturation values of S-wave velocities from the self-consistent model also best represent the measured data at the upscaled scale. S-wave velocities for the patchy and uniform saturation calculated by Gassmann fluid substitution are same.

Overall, P-wave and S-wave velocities from the self-consistent model are larger than the values from Gassmann fluid substitution for each type of fluid mixing. In Figure 4.14, comparison of histograms between Gassmann fluid substitution and the self-consistent model for patchy saturation shows large differences in P-wave velocities and small differences in S-wave velocities. From these results, we can demonstrate that P-wave velocities are more dependent on the frequency than S-wave velocities. However, the differences of P-wave and S-wave velocities for the uniform saturation between two models are smaller than those for the patchy saturation.

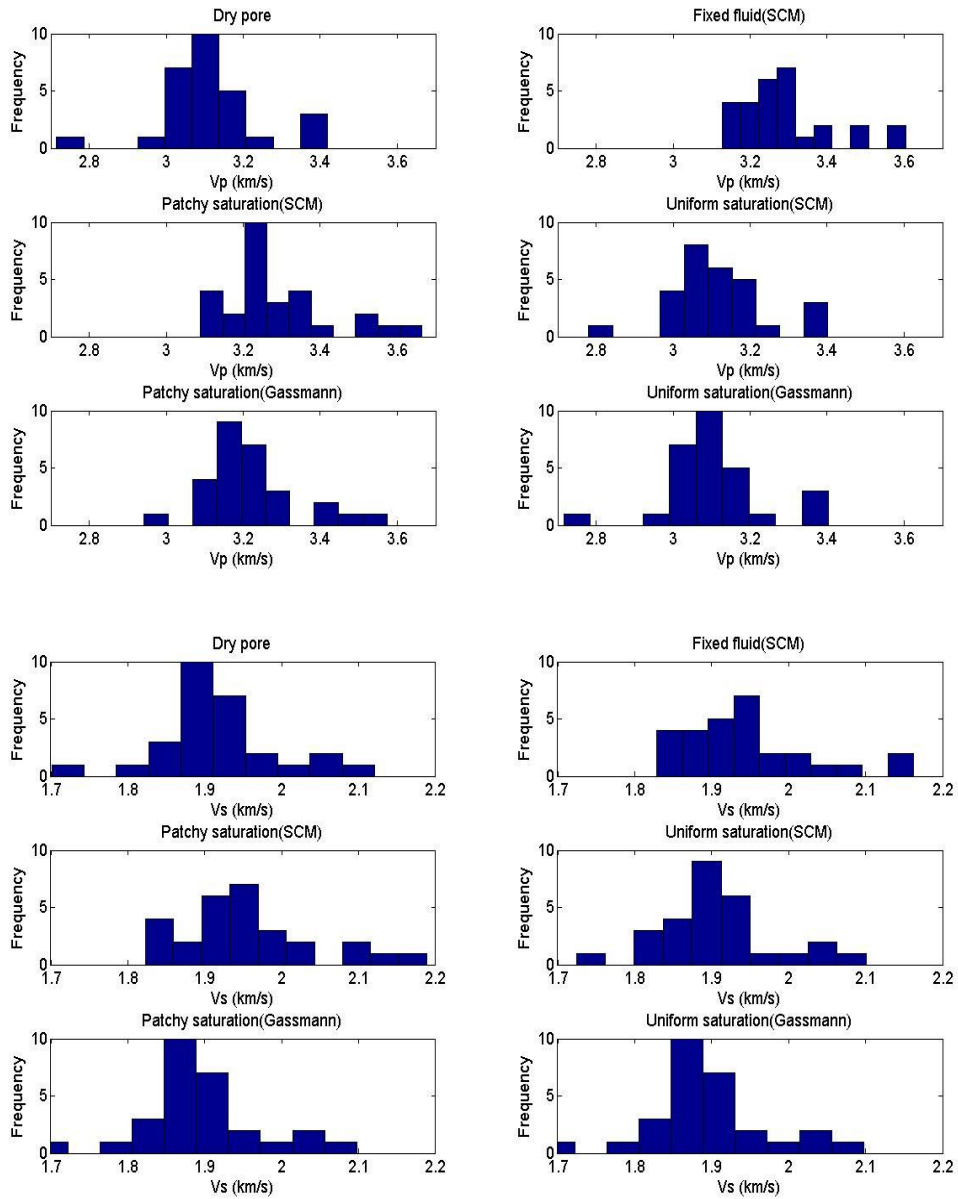


Figure 4.14: Comparison of histograms of P-wave and S-wave velocities for dry pores, fixed fluid, the patchy and uniform saturation calculated by the self-consistent model and Gassmann fluid substitution for the Haynesville shale.

#### 4.2.6 Discussion

In this section, the calculated velocity modeling results between the self-consistent model and Gassmann substitution are summarized as: For P-wave velocities,  $V_p \text{ patchy\_SCM} > V_p \text{ patchy\_Gassmann} > V_p \text{ uniform\_SCM} > V_p \text{ dry} > V_p \text{ Uniform\_Gassmann}$ . For S-wave velocities,  $V_s \text{ patchy\_SCM} > V_s \text{ dry} > V_s \text{ uniform\_SCM} > V_s \text{ patchy\_Gassmann} = V_s \text{ uniform\_Gassmann}$ .

When going from a dry- to fluid-saturated rock, both the elastic bulk modulus of rock and the bulk density increase. Contrary to that, the elastic shear modulus of rock depends on the frequencies. At low frequencies, the shear moduli of dry- and fluid-saturated rock are same according to Gassmann's relation. However, the shear modulus of fluid-saturated rock increases with saturation changes compared to that of dry rock at high frequencies because the elastic-stiffening effect is exaggerated for both bulk and shear moduli. For inclusion-based models such as the self-consistent model that are high-frequency models, the velocities increase due to the frequency-related dispersion. The shear moduli and S-wave velocities are sensitive to fluids at high frequencies.

Comparing the calculated velocities for various types of fluid mixing to both the measured velocities from the well log and upscaled velocities from the Backus average, P-wave and S-wave velocities calculated from the self-consistent model for the patchy saturation cases best represent the measured data at the upscaled scale than other types of fluid mixing.

### **4.3 RESULTS OF DETERMINED PORE ASPECT RATIOS FOR VARIOUS TYPES OF FLUID DISTRIBUTIONS**

In Chapter 4.1, P-wave velocities calculated from the self-consistent model were compared to upscaled observed velocities using the moving Backus average to determine pore aspect ratios with fixed fluid properties. From the simulations of the effect of fluids, considerable P-wave velocity differences resulted according to the ways fluids were mixed. In this section, I performed velocity modeling to determine pore aspect ratios for various fluid properties such as dry pores, the patchy saturation, and uniform saturation cases. This examines the effect of pore-fluid mixing on the estimated pore aspect ratio distributions. Aspect ratios from the Gassmann-derived velocities were also computed to compare the differences. In this analysis, original XRD and interpolated composition data were used at 50 Hz.

#### **4.3.1 Pore Aspect ratios by SCM for various types of fluid distributions**

##### ***4.3.1.1 Results of XRD data***

Estimated pore aspect ratios of the XRD data for various fluid saturations types are summarized in Table 4.7. Estimated pore aspect ratios of the XRD data for the patchy saturation vary from 0.049 to 0.298 ( a range of about one order of magnitude) with the mean of 0.147. The range of pore aspect ratios of the XRD data for uniform saturation cases is from 0.077 to 0.308 with an average of 0.174. The values for the dry pore are from 0.079 to 0.298 with the mean of 0.169 and very close to uniform saturation cases. Pore aspect ratios calculated for patchy saturation are the smallest values, then, dry pore values, and uniform saturation values are the largest.

Table 4.7: The maximum, minimum and mean values of estimated pore aspect ratios and calculated effective elastic moduli of the XRD data for dry pores, patchy and uniform saturation by the velocity modeling for 50 Hz for the Haynesville shale. From the left, estimated pore aspect ratios, P-wave and S-wave velocities calculated from the Backus average, bulk and shear moduli, P-wave and S-wave velocities calculated from the self-consistent model, differences of P-wave and S-wave velocities between the Backus average and the self-consistent model, respectively.

(a) Dry pores									
Pore aspect ratios	Vp_backus	Vs_backus	K_scm	$\mu$ _scm	Vp_scm	Vs_scm	Vp Diff (%)	Vs Diff (%)	
Max	0.298	3.5913	2.2319	15.0437	11.5439	3.5815	2.2147	0.42	1.36
Min	0.079	3.1311	1.7955	10.9083	7.7763	3.1293	1.8790	-0.44	-7.65
Mean	0.168	3.2853	1.9707	12.3623	9.1207	3.2854	2.0025	-0.01	-1.69
(b) Patchy saturation									
Pore aspect ratios	Vp_backus	Vs_backus	K_scm	$\mu$ _scm	Vp_scm	Vs_scm	Vp Diff (%)	Vs Diff (%)	
Max	0.298	3.5913	2.2319	16.3824	11.2089	3.5839	2.1637	0.49	5.92
Min	0.049	3.1311	1.7955	11.4036	7.6769	3.1194	1.8471	-0.41	-2.89
Mean	0.147	3.2853	1.9707	13.1875	8.9025	3.2843	1.9572	0.03	0.60
(c) Uniform saturation									
Pore aspect ratios	Vp_backus	Vs_backus	K_scm	$\mu$ _scm	Vp_scm	Vs_scm	Vp Diff (%)	Vs Diff (%)	
Max	0.308	3.5913	2.2319	15.6532	11.7764	3.5949	2.2056	0.39	1.9
Min	0.077	3.1311	1.7955	11.1748	7.8589	3.1199	1.8666	-0.33	-7.1
Mean	0.174	3.2853	1.9707	12.7273	9.2406	3.2835	1.9934	0.06	-1.2

#### 4.3.1.2 Results of interpolated data

Estimated pore aspect ratios for various fluid saturation types for the interpolated data are summarized in Table 4.8. Estimated pore aspect ratios of the interpolated data for the patchy saturation vary from 0.035 to 0.296 with the mean of 0.145. The range of pore

aspect ratios of the interpolated data for the uniform saturation is from 0.051 to 0.319 with an average of 0.171. Estimated pore aspect ratios of the interpolated data for dry pores have the values from 0.052 to 0.310 with mean 0.168. Pore aspect ratios calculated for patchy saturation are also the smallest values, followed by dry pores values, and uniform saturation values are the largest as in the XRD data. Pore aspect ratios for dry pores are similar to those from the uniform saturation.

Table 4.8: The maximum, minimum and mean values of estimated pore aspect ratios and calculated effective elastic moduli of the interpolated data for dry pores, patchy and uniform saturation by the velocity modeling for 50 Hz for the Haynesville shale. From the left, with the same data as shown in Table 4.7.

(a) Dry pores									
	Pore aspect ratios	Vp_backus	Vs_backus	K_scm	$\mu$ _scm	Vp_scm	Vs_scm	Vp Diff (%)	Vs Diff (%)
Max	0.310	3.5913	2.2410	15.6140	12.6890	3.5996	2.2428	0.38	2.88
Min	0.052	3.1220	1.7933	10.6994	7.6420	3.1208	1.8748	-0.49	-7.63
Aver	0.168	3.2889	1.9744	12.3980	9.1557	3.2897	2.0057	-0.02	-1.66
(b) Patchy saturation									
	Pore aspect ratios	Vp_backus	Vs_backus	K_scm	$\mu$ _scm	Vp_scm	Vs_scm	Vp Diff (%)	Vs Diff (%)
Max	0.296	3.5913	2.2410	17.6380	11.3634	3.5825	2.1607	0.43	5.76
Min	0.035	3.1220	1.7933	11.4721	7.5575	3.1240	1.8313	-0.40	-3.72
Mean	0.145	3.2889	1.9744	13.2395	8.9412	3.2906	1.9613	-0.05	0.58
(c) Uniform saturation									
	Pore aspect ratios	Vp_backus	Vs_backus	K_scm	$\mu$ _scm	Vp_scm	Vs_scm	Vp Diff (%)	Vs Diff (%)
Max	0.319	3.5913	2.2410	15.8008	12.5358	3.5839	2.2211	0.42	3.18
Min	0.051	3.1220	1.7933	11.1459	7.7577	3.1218	1.8678	-0.46	-7.09
Mean	0.171	3.2889	1.9744	12.7540	9.2692	3.2874	1.9963	0.05	-1.19

From the histograms in Figure 4.15, it is also possible to find the range of the pore aspect ratios for the various types of fluid properties. Contrary to that, for P-wave velocities calculated by the self-consistent model (Figure 4.9), patchy saturation cases have the largest values, then, uniform saturation cases, and dry pore values are the smallest. The histograms for the interpolated data appear to be normally distributed, but some of the histograms for the XRD data in Figure 4.15 appear uniformly distributed.

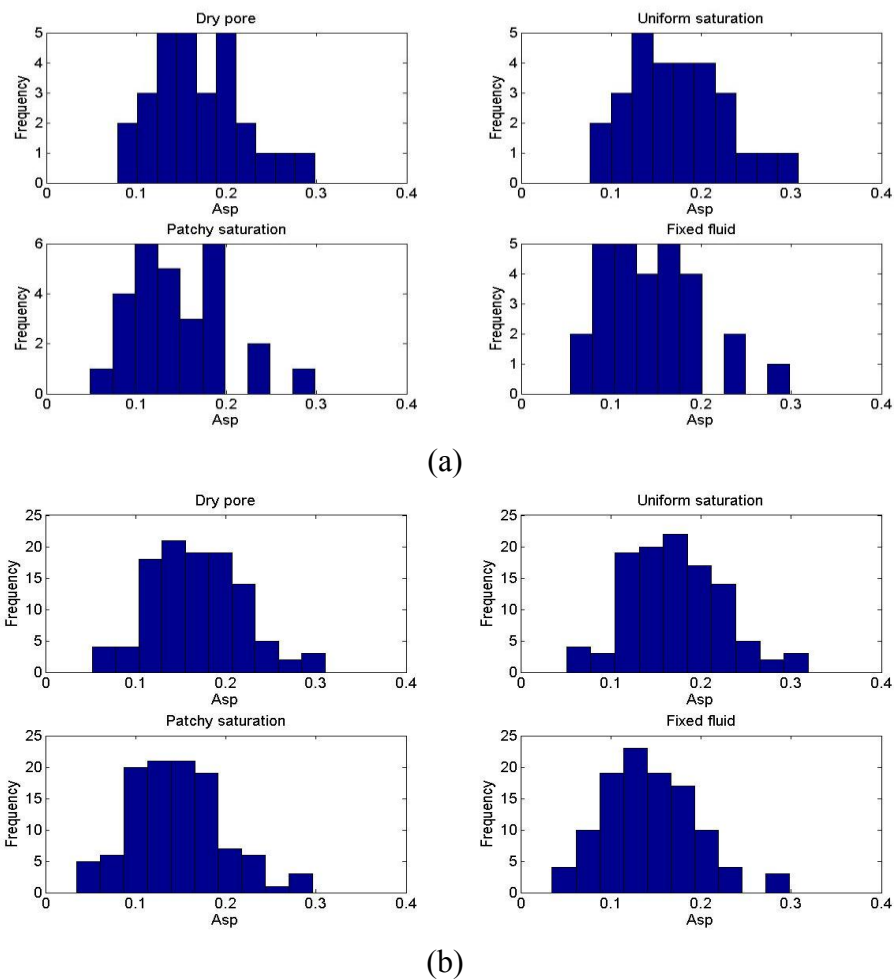


Figure 4.15: Comparison of histograms of estimated pore aspect ratios of (a) the XRD data (b) the interpolated data for dry pores, fixed fluids, the patchy and uniform saturation by velocity modeling (for 50 Hz) for the Haynesville Shale.

### 4.3.1.3 Comparison of results for the self-consistent model

Estimated pore aspect ratios of the XRD data and the interpolated data for dry pores, patchy and uniform saturations by velocity modeling are compared in Table 4.9 and Figure 4.16. It is evident that values from the interpolated data show specific values and variations of pore aspect ratios compared to those for the XRD data. Therefore, it is possible to obtain more specific information from the interpolated data for the Haynesville formation.

Table 4.9: Comparisons of the maximum, minimum and mean values of estimated pore aspect ratios of (a) the XRD data (b) the interpolated data for dry pores, patchy and uniform saturation by velocity modeling (for 50 Hz) for the Haynesville shale ( $Asp_{patchy} < Asp_{dry} < Asp_{uniform}$ ).

a) XRD data			
Pore aspect ratio	Dry pores	Patchy saturation	Uniform Saturation
Max	0.298	0.298	0.308
Min	0.079	0.049	0.077
Mean	0.169	0.147	0.174
b) Interpolated data			
Pore aspect ratio	Dry pores	Patchy saturation	Uniform Saturation
Max	0.310	0.296	0.319
Min	0.052	0.035	0.051
Mean	0.168	0.145	0.171

The graphs of estimated values for the patchy and uniform saturation in Figure 4.16 look very similar, but estimated pore aspect ratios for patchy saturation show a

narrower range and smaller values than those of uniform saturation. In addition, pore aspect ratios of the interpolated data for patchy saturation (mean: 0.145) show a very similar range of values to those of the XRD data for patchy saturation (mean: 0.147).

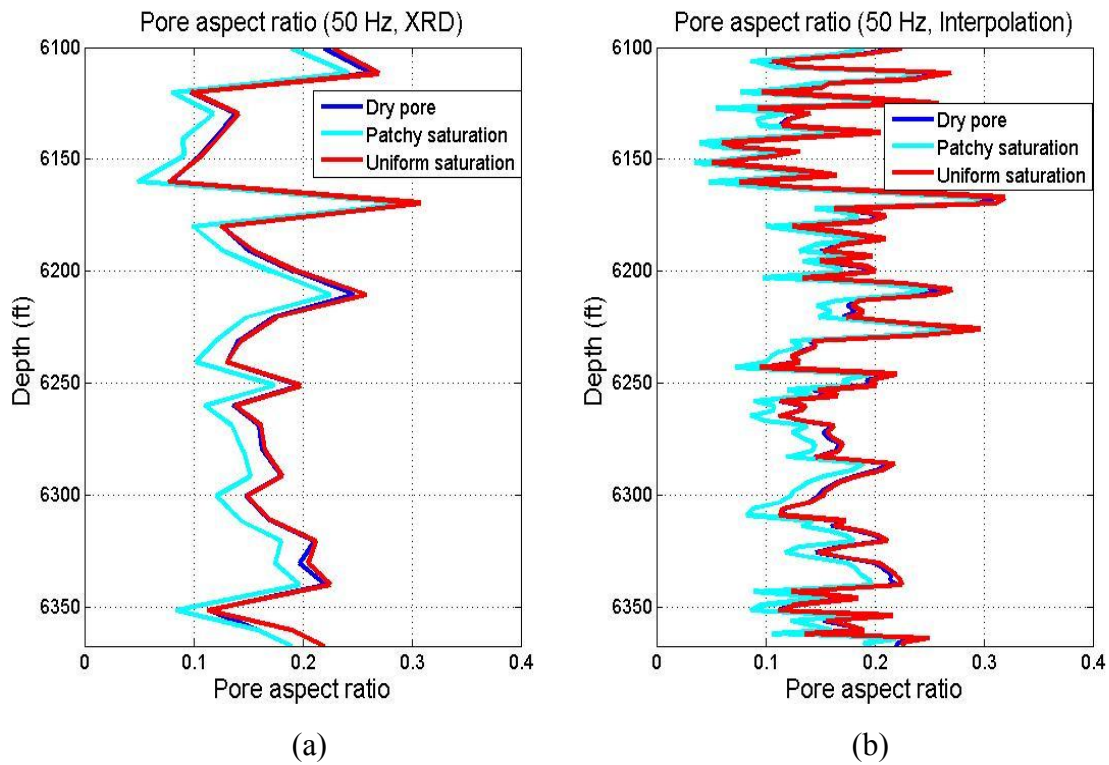
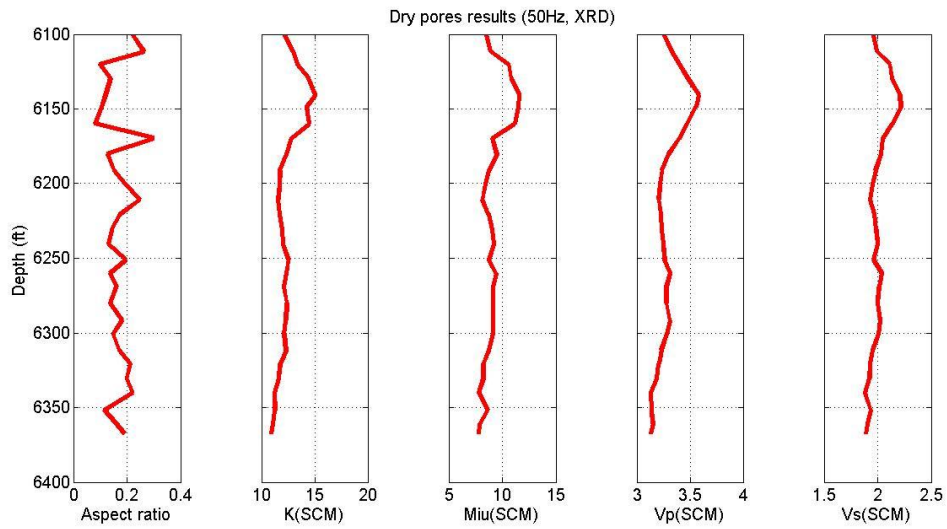


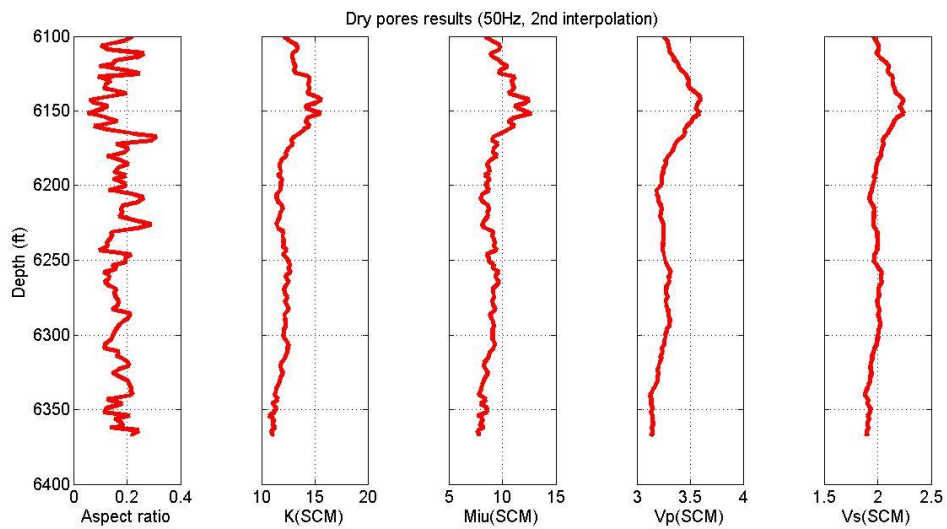
Figure 4.16: Estimated pore aspect ratios for (a) the XRD data (b) the interpolated data for dry pores, the patchy and uniform saturation cases by using the self-consistent model and the Backus average (50 Hz) for the Haynesville Shale.

Estimated pore aspect ratios, effective bulk and shear moduli, effective P-wave and S-wave velocities calculated by the self-consistent model for dry pores, patchy and uniform saturation by velocity modeling for the XRD data and the interpolated data are compared in Figures 4.17, 4.18 and 4.19. Pore aspect ratios estimated for the interpolated data show more specific and detailed variations versus depths than those of the XRD data

in all figures. For the interpolated data, effective moduli, P-wave and S-wave velocities also show more particularized and minute values as a function of depth compared to those of the XRD data. As numbers of data increase, pore aspect ratios versus depths represent the specific change of values well. Regarding types of fluid saturations, pore aspect ratios calculated for patchy saturation are the smallest values, and uniform saturation values are the largest. Dry pores values are in between two saturations.

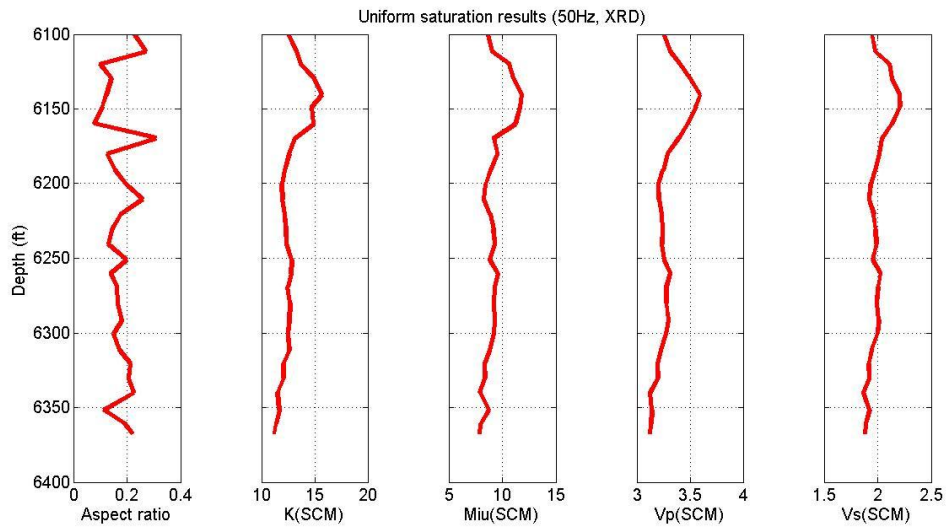


(a)

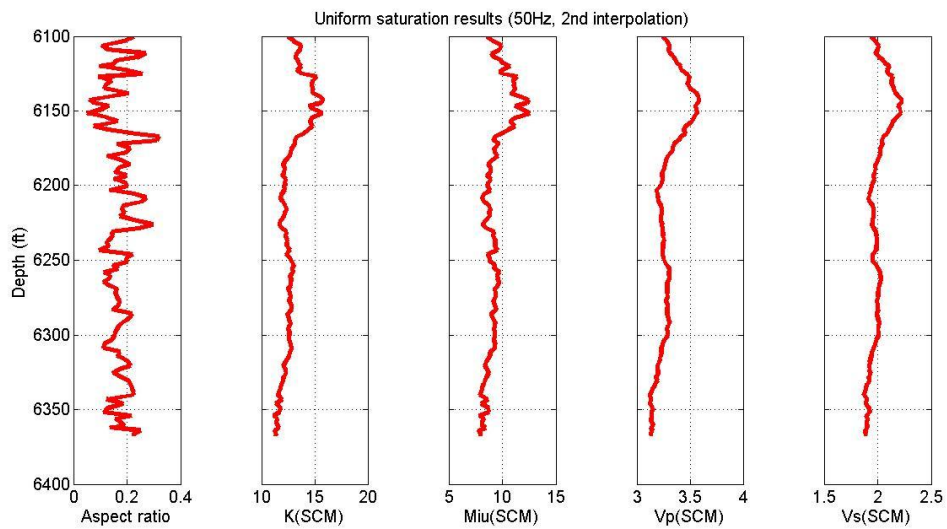


(b)

Figure 4.17: Estimated pore aspect ratios, effective bulk and shear moduli, effective P-wave and S-wave velocities calculated by the self-consistent model of (a) the XRD data and (b) the interpolated data for dry pores by velocity modeling (for 50 Hz).

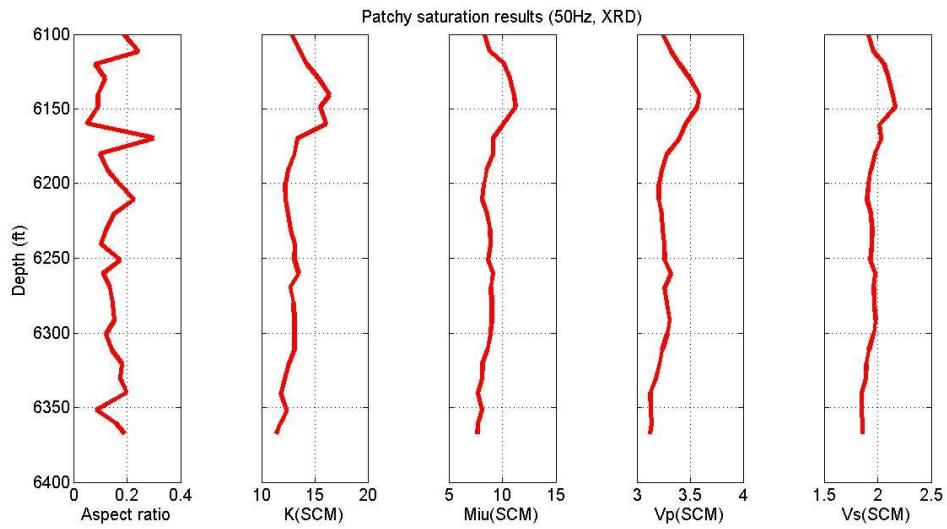


(a)

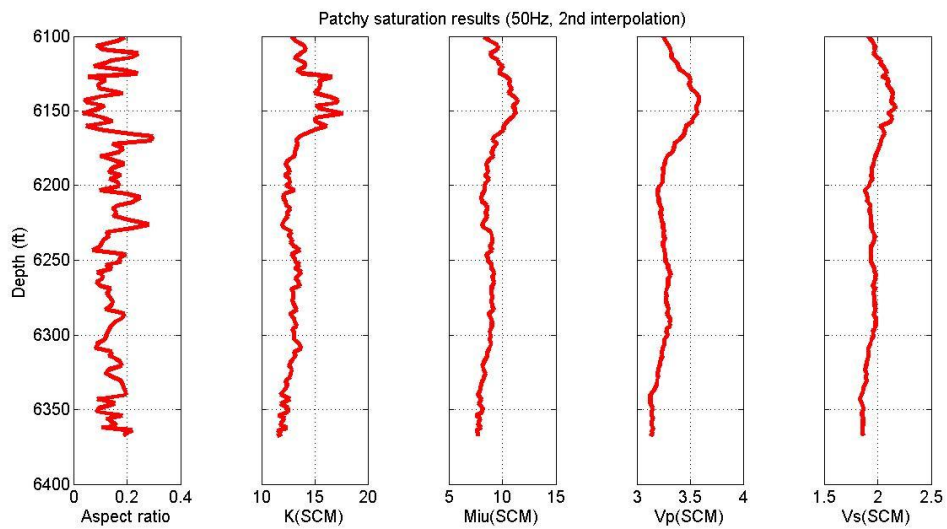


(b)

Figure 4.18: Estimated pore aspect ratios, effective bulk and shear moduli, effective P-wave and S-wave velocities calculated by the self-consistent model of (a) the XRD data and (b) the interpolated data for the uniform saturation by velocity modeling (for 50 Hz).



(a)



(b)

Figure 4.19: Estimated pore aspect ratios, effective bulk and shear moduli, effective P-wave and S-wave velocities calculated by the self-consistent model of (a) the XRD data and (b) the interpolated data for the patchy saturation by velocity modeling (for 50 Hz).

### **4.3.2 Pore aspect ratios by Gassmann substitution for various types of fluid distributions**

Pore aspect ratios from the Gassmann-derived velocities were computed to compare the differences between the self-consistent model and Gassmann substitution. Velocity modeling was performed to determine pore aspect ratios for the patchy saturation and uniform saturation cases to analyze the effect of pore fluid mixing on determining pore aspect ratios, but using the Gassmann-derived velocities instead of velocities calculated from the self-consistent model. In this analysis, original XRD and interpolated composition data were also used at 50 Hz.

#### ***4.3.2.1 Modeling procedure***

The modeling procedure is same as outlined in Figure 3.4 except using the Gassmann-derived velocities.

- 1) Calculate dry pore moduli by the self-consistent model (Figure 3.4). ( $K$ ,  $\mu$ ,  $\rho$  for dry pores = 0) (Input: composition, initial estimated aspect ratio distribution).
- 2) Calculate the patchy and uniform saturation moduli and velocities from the dry rock values by Gassmann fluid substitution, respectively (Equations 2.16 and 2.17).
- 3) Compare calculated P-wave velocity by Gassmann substitution to the Backus average (0.5% P-wave velocity difference) for the patchy and uniform saturation, respectively (Figure 3.4).
- 4). Determine pore aspect ratios for the patchy and uniform saturation in case this difference meets the criterion.

#### 4.3.2.2 Results of XRD data

Pore aspect ratios from the Gassmann-derived velocities for various fluid property types for the XRD data are summarized in Table 4.10. Estimated pore aspect ratios of the XRD data for the patchy saturation vary from 0.059 to 0.296 with the mean of 0.155. The range of pore aspect ratios of the XRD data for the uniform saturation is from 0.080 to 0.310 with the average of 0.177. Pore aspect ratios estimated for patchy saturation from the Gassmann-derived velocities are the smallest values and those for uniform saturation are the largest. These values are larger than pore aspect ratios estimated by the self-consistent model.

Table 4.10: The maximum, minimum and mean values of estimated pore aspect ratios and calculated effective elastic moduli of the XRD data for patchy and uniform saturation by Gassmann-derived velocities for 50 Hz for the Haynesville shale. From the left, estimated pore aspect ratios, P-wave and S-wave velocities calculated from the Backus average, bulk and shear moduli, P-wave and S-wave velocities calculated from the self-consistent model, differences of P-wave and S-wave velocities between the Backus average and the self-consistent model, respectively.

(a) Patchy saturation (Gassmann)									
	Pore aspect ratios	Vp_backus	Vs_backus	K_gass	$\mu_{gass}$	Vp_gass	Vs_gass	Vp Diff (%)	Vs Diff (%)
Max	0.296	3.5913	2.2319	16.9858	11.0504	3.6013	2.1483	0.44	8.40
Min	0.059	3.1311	1.7955	11.3942	7.4990	3.1237	1.8104	-0.36	-1.19
Mean	0.155	3.2853	1.9707	13.3838	8.6892	3.2833	1.9337	0.06	1.80
(b) Uniform saturation (Gassmann)									
	Pore aspect ratios	Vp_backus	Vs_backus	K_gass	$\mu_{gass}$	Vp_gass	Vs_gass	Vp Diff (%)	Vs Diff (%)
Max	0.310	3.5913	2.2319	15.5576	11.6656	3.5804	2.2073	0.30	1.80
Min	0.080	3.1311	1.7955	11.3318	7.8980	3.1290	1.8690	-0.46	-7.23
Mean	0.177	3.2853	1.9707	12.8251	9.2468	3.2907	1.9942	-0.17	-1.26

### 4.3.2.3 Results of interpolated data

Pore aspect ratios from the Gassmann-derived velocities for various fluid property types for the interpolated data are summarized in Table 4.11. Estimated pore aspect ratios of the interpolated data for the patchy saturation vary from 0.045 to 0.301 with the mean of 0.153. The range of pore aspect ratios of the interpolated data for the uniform saturation is from 0.053 to 0.351 with the average of 0.174. Pore aspect ratios estimated for patchy saturation are also the smallest values and those for uniform saturation are the largest as in the interpolated data. Pore aspect ratios from the Gassmann-derived velocities are larger than those values estimated by the self-consistent model.

Table 4.11: The maximum, minimum and mean values of estimated pore aspect ratios and calculated effective elastic moduli of the interpolated data for patchy and uniform saturation by Gassmann-derived velocities for 50 Hz. From the left, with the same data as shown in Table 4.10.

(a) Patchy saturation (Gassmann)									
	Pore aspect ratios	Vp_backus	Vs_backus	K_gass	$\mu_{gass}$	Vp_gass	Vs_gass	Vp Diff (%)	Vs Diff (%)
Max	0.301	3.5913	2.2410	18.4181	10.9680	3.5857	2.1396	0.46	5.69
Min	0.045	3.1220	1.7933	11.5586	7.3231	3.1108	1.7792	-0.40	-1.89
Mean	0.153	3.2889	1.9744	13.4966	8.7034	3.2864	1.9344	0.14	1.20

(b) Uniform saturation (Gassmann)									
	Pore aspect ratios	Vp_backus	Vs_backus	K_gass	$\mu_{gass}$	Vp_gass	Vs_gass	Vp Diff (%)	Vs Diff (%)
Max	0.321	3.5913	2.2410	16.0323	12.5409	3.5972	2.2228	0.49	3.13
Min	0.053	3.1220	1.7933	11.2958	7.7596	3.1202	1.8647	-0.48	-6.45
Mean	0.174	3.2889	1.9744	12.8487	9.2710	3.2921	1.9954	-0.10	-1.14

The histograms in Figure 4.20 show the range of the pore aspect ratios calculated by Gassmann fluid substitution for the various types of fluid properties. These histograms follow the same trend of pore aspect ratios calculated by the self-consistent model (Figure 4.15). Uniform saturation cases have the largest values, then, dry pore values, and patchy saturation values are the smallest.

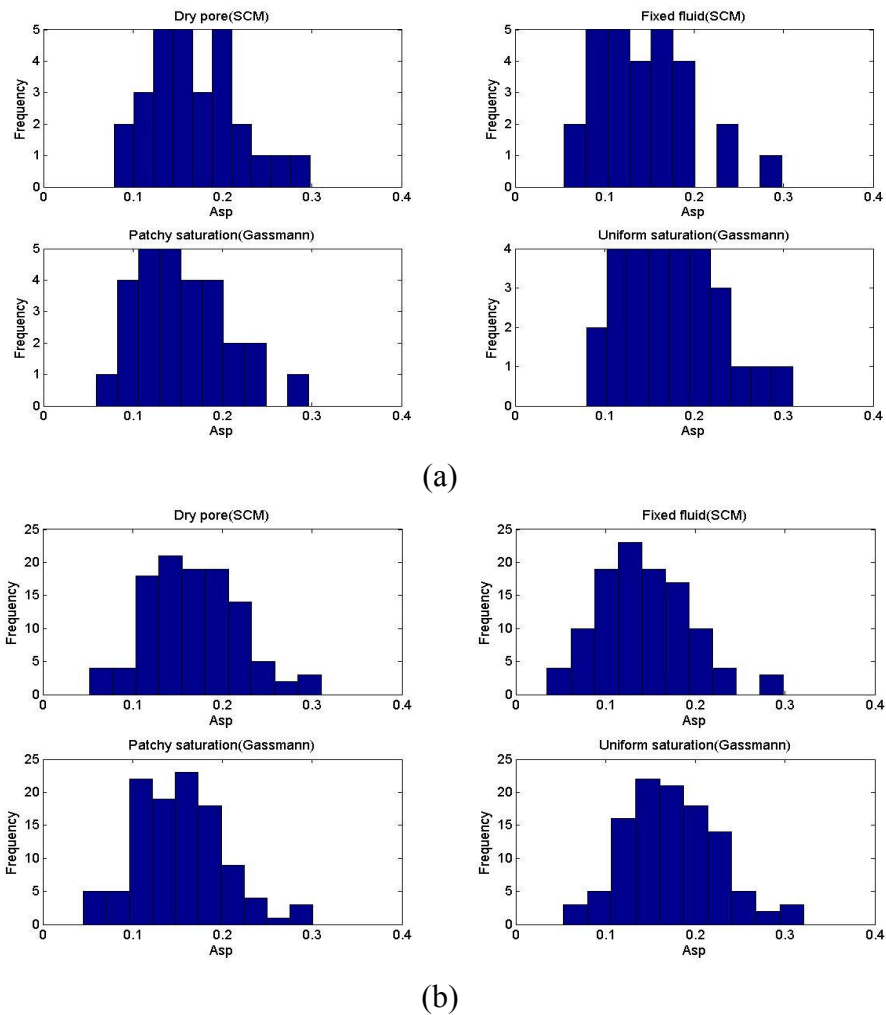


Figure 4.20: Comparison of histograms of estimated pore aspect ratios from the Gassmann-derived velocities of (a) the XRD data (b) the interpolated data for dry pores (SCM), fixed fluids (SCM), the patchy and uniform saturation by velocity modeling (for 50 Hz) for the Haynesville Shale.

#### 4.3.2.4 Comparison of results for Gassmann Substitution

Estimated pore aspect ratios from the Gassmann-derived velocities for the patchy and uniform saturation for the XRD data and the interpolated data are compared in Table 4.12. Values from the interpolated data also show specific values and variations of pore aspect ratios compared to those for the XRD data.

Table 4.12: Comparisons of the maximum, minimum and mean values of estimated pore aspect ratios from the Gassmann-derived velocities of (a) the XRD data (b) the interpolated data for dry pores, patchy and uniform saturation by velocity modeling (for 50 Hz) ( $Asp_{patchy} < Asp_{dry} < Asp_{uniform}$ ).

a) XRD data			
Pore aspect ratio	Dry pores(SCM)	Patchy saturation	Uniform Saturation
Max	0.298	0.296	0.310
Min	0.079	0.059	0.080
Mean	0.169	0.155	0.177
b) Interpolated data			
Pore aspect ratio	Dry pores(SCM)	Patchy saturation	Uniform Saturation
Max	0.310	0.301	0.321
Min	0.052	0.045	0.053
Mean	0.168	0.153	0.174

The graphs of estimated values for the patchy and uniform saturation in Figure 4.21 look also very similar, but estimated pore aspect ratios for patchy saturation show the narrower range and smaller values than those of uniform saturation like estimated pore aspect ratios from the self-consistent model (Figure 4.16). In addition, pore aspect ratios of the interpolated data for patchy saturation (mean: 0.153) show a very similar range of values to those of the XRD data for patchy saturation (mean: 0.155). However, estimated pore aspect ratios from the interpolated data show more specific values and variations of versus depth compared to those from the XRD data.

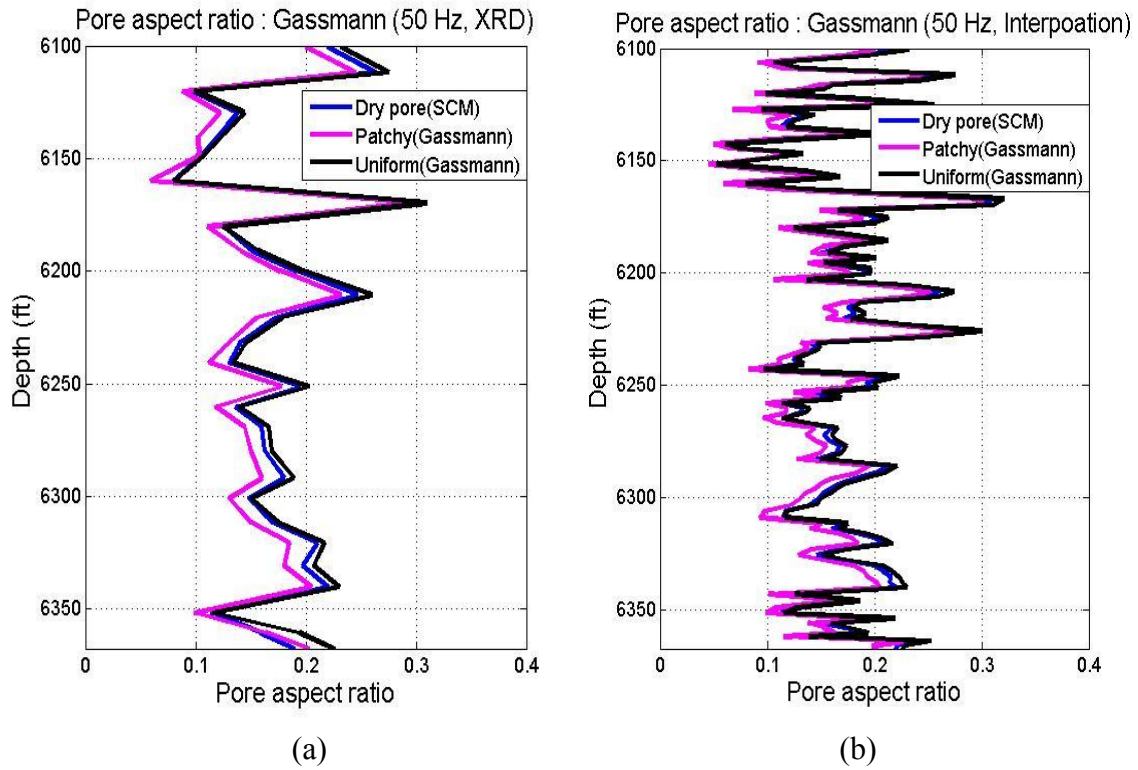
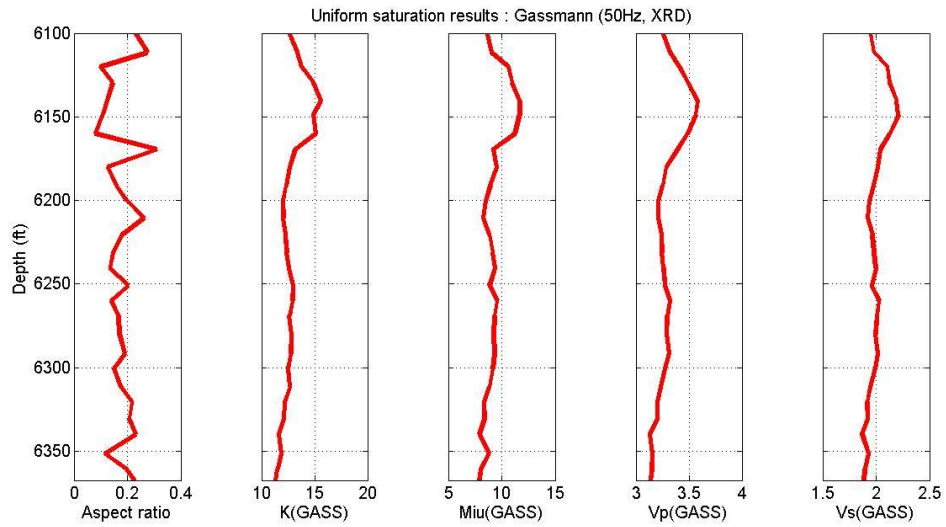
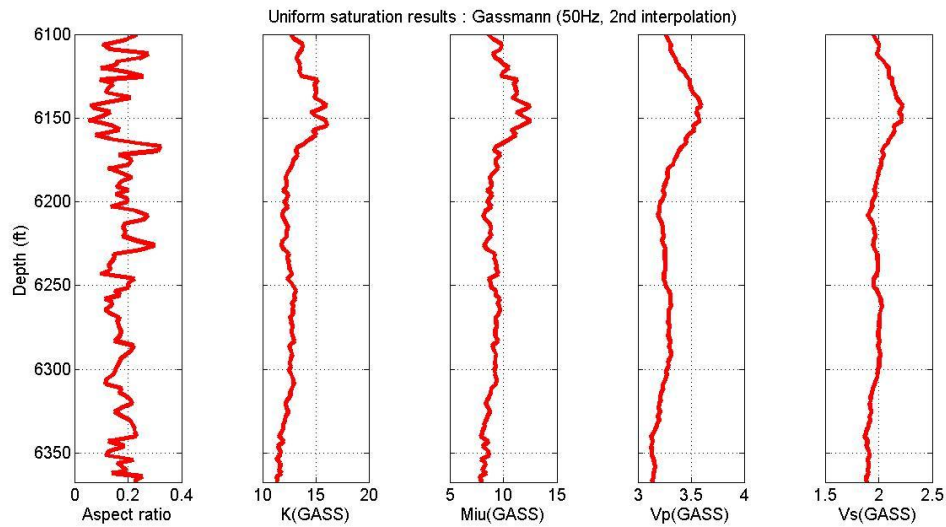


Figure 4.21: Estimated pore aspect ratios from the Gassmann-derived velocities for (a) the XRD data (b) the interpolated data for dry pores (SCM), the patchy and uniform saturation (50 Hz) for the Haynesville Shale.

Estimated pore aspect ratios, effective bulk and shear moduli, effective P-wave and S-wave velocities calculated by Gassmann fluid substitution for the patchy and uniform saturation by velocity modeling for the XRD data and the interpolated data are compared in Figures 4.22, and 4.23. Pore aspect ratios estimated for the interpolated data by Gassmann fluid substitution also show more specific and minute variations versus depth than those of the XRD data. In addition, effective moduli, P-wave and S-wave velocities show more particularized values versus depth compared to those of the XRD data. Estimated pore aspect ratios for patchy saturation show smaller values than those of uniform saturation.

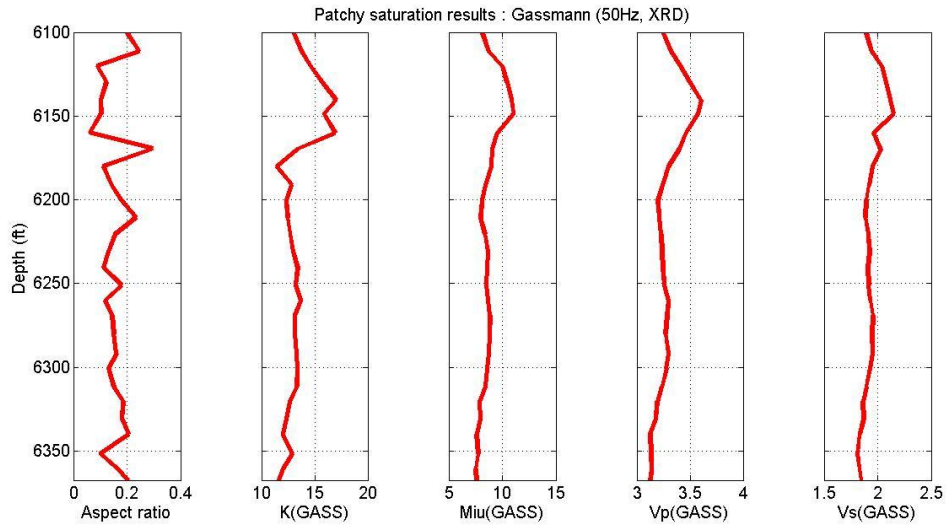


(a)

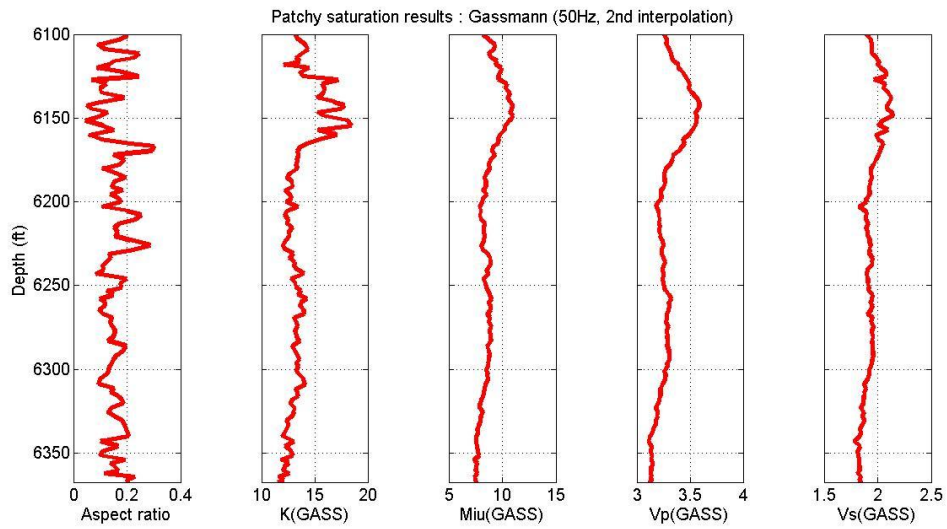


(b)

Figure 4.22: Estimated pore aspect ratios, effective bulk and shear moduli, effective P-wave and S-wave velocities calculated by Gassmann fluid substitution of (a) the XRD data and (b) the interpolated data for the uniform saturation by velocity modeling (for 50 Hz).



(a)



(b)

Figure 4.23: Estimated pore aspect ratios, effective bulk and shear moduli, effective P-wave and S-wave velocities calculated by Gassmann fluid substitution of (a) the XRD data and (b) the interpolated data for the patchy saturation by velocity modeling (for 50 Hz).

### 4.3.3 Comparison of pore aspect ratios between the self-consistent model and Gassmann fluid substitution

As already described in the velocity comparison, the self-consistent model is appropriate for high frequency modeling of data. However, Gassmann fluid substitution makes it possible to calculate the bulk and shear moduli of the fluid-saturated rock from the dry rock mineral moduli at low frequency. For both the patchy and uniform saturation cases, estimated pore aspect ratios by Gassmann fluid substitution are larger than values from the self-consistent model where the fluid was placed directly in the pores (Table 4.13, Figures 4.24 and 4.25.).

Table 4.13: Comparison of estimated pore aspect ratios of (a) the XRD data (b) the interpolated data for dry pores, the patchy and uniform saturation calculated by the self-consistent model and Gassmann fluid substitution (Patchy(SCM) < Patchy(Gassmann) < Dry pores < Uniform(SCM) < Uniform(Gassmann)).

Depth	SCM			Gassmann	
	Pore Asp (dry)	Pore Asp (patchy)	Pore Asp (Uniform)	Pore Asp (patchy)	Pore Asp (uniform)
Max	0.298	0.298	0.308	0.296	0.310
Min	0.079	0.049	0.077	0.059	0.080
Mean	0.169	0.147	0.174	0.155	0.177

(a)

Depth	SCM			Gassmann	
	Pore Asp (dry)	Pore Asp (patchy)	Pore Asp (Uniform)	Pore Asp (patchy)	Pore Asp (uniform)
Max	0.310	0.296	0.319	0.301	0.321
Min	0.052	0.035	0.051	0.045	0.053
Meane	0.168	0.145	0.171	0.153	0.174

(b)

These different pore shapes result from velocity differences calculated from two methods. Velocity calculated from the self-consistent model is always larger than value

from Gassmann substitution for both the patchy and uniform saturation because of the inherently frequency-dependent velocity dispersion. Therefore, estimated pore aspect ratios from the self-consistent model are smaller than those from Gassmann substitution because the velocity is inversely related to the aspect ratio in this modeling (Figures 4.24 and 4.25). Pore aspect ratios calculated for the patchy saturation are the smallest values, and uniform saturation values are the largest both in the self-consistent model and Gassmann fluid substitution. Estimated pore aspect ratios by Gassmann fluid substitution are larger than values from the self-consistent model for both the patchy and uniform saturation cases.

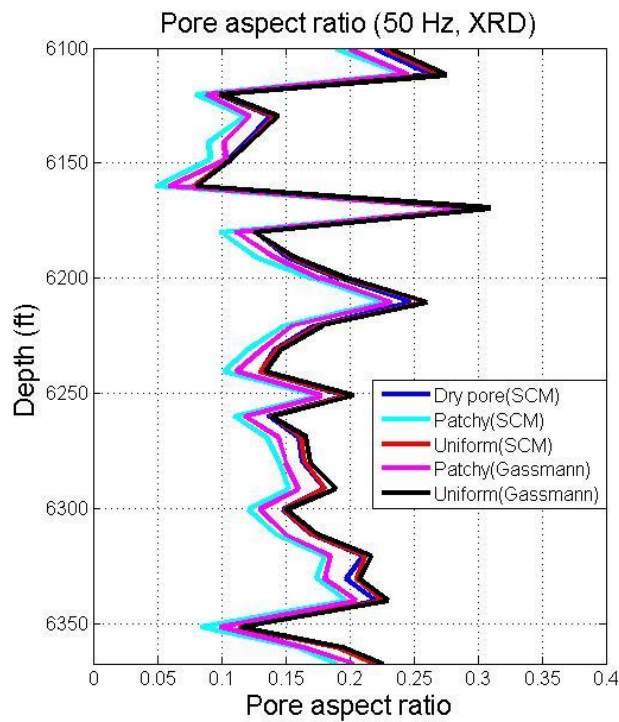


Figure 4.24: Comparison of graphs of estimated pore aspect ratios of the XRD data for dry pores, the patchy and uniform saturation calculated by the self-consistent model and Gassmann fluid substitution for the Haynesville.

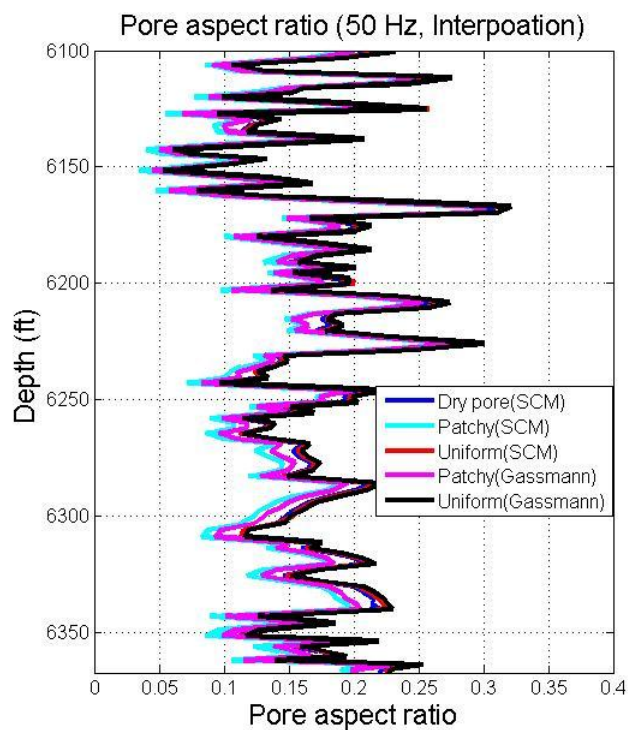
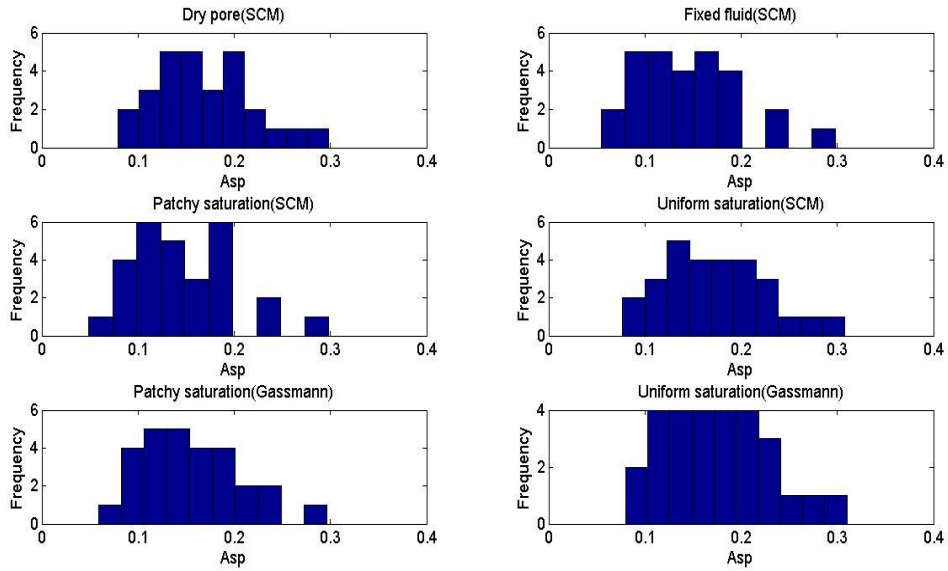
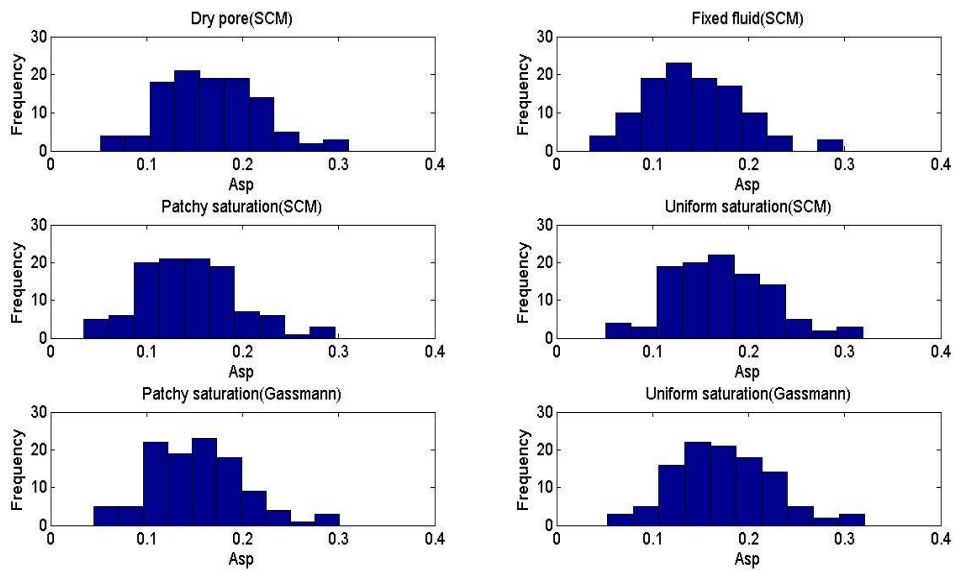


Figure 4.25: Comparison of graphs of estimated pore aspect ratios of the interpolated data for dry pores, the patchy and uniform saturation calculated by the self-consistent model and Gassmann fluid substitution for the Haynesville.

The histograms in Figure 4.26 compare the range of the pore aspect ratios calculated by both the self-consistent model and Gassmann fluid substitution for the various types of fluid mixtures for the XRD data and the interpolated data. Uniform saturation cases have the largest values, then, dry pore values, and patchy saturation values are the smallest for both the self-consistent model and Gassmann fluid substitution. In addition, pore aspect ratios calculated by Gassmann fluid substitution are larger than values from the self-consistent model for two fluid saturations. The histograms for the interpolated data appear to be normally distributed. However, some of the histograms for the XRD data appear uniformly distributed.



(a)



(b)

Figure 4.26: Comparison of histograms of estimated pore aspect ratios of (a) the XRD data and (b) the interpolated data for dry pores, the patchy and uniform saturation calculated by the self-consistent model and Gassmann fluid substitution for the Haynesville.

#### **4.3.4 Discussion**

##### **4.3.4.1 Determination of pore aspect ratios for pore fluid distributions**

Estimated pore aspect ratios for dry pores, for the patchy saturation and uniform saturation cases by velocity modeling (for 50 Hz), show that these estimates are strongly affected by the pore fluid distribution. Hence, in order to accurately interpret reservoir characteristics from the unsaturated zone such as the Haynesville Shale, the dependence of estimated pore shapes on fluid distribution needs to be fully understood.

Knight and Nolen-Hoeksema (1990) indicated that laboratory data during a continuous imbibition/drainage experiment showed dependences of elastic wave velocities on the pore fluid distribution of water and air in the rock. In the shale formation, gas that originated from organic content in grains of the shale formation moved to the pore space. Clay-bound water is already saturated inside pores that are not in communication with one another. Due to large differences (orders of magnitude) in elastic properties between water and gas, the mixing procedure would be considered as a patchy saturation process for water and gas. Knight (1991) also indicated that partially saturated samples can be attributed to the presence of mixing effect at the air/water interface. Therefore, it is reasonable to assume that the mixing saturation in the Haynesville formation would be heterogeneous. The most reasonable pore aspect ratios for the Haynesville Shale vary from 0.035 to 0.296 with a mean of 0.145 such as determined values for patchy saturation case using the self-consistent model in this study. Compared to other rock types such as carbonates, this is a rather narrow range, about one order of magnitude. Velocity calculated from Gassmann substitution is always smaller than value from the self-consistent model both the patchy and uniform saturation because

of the inherently frequency-controlled velocity dispersion. Therefore, estimated pore aspect ratios from Gassmann substitution both for the patchy and uniform saturation are larger than values of the self-consistent model because the estimated aspect ratio is inversely related to the modeled (calculated) velocity in this modeling as described in Chapter 4.3.4.2.

#### **4.3.4.2 Difference of velocity modeling for P-wave velocities and pore aspect ratios**

These results show quite different effects of fluid property types to pore aspect ratio determination and P-wave velocity calculation. It means fluid mixing affects differently the calculations for pore aspect ratios and P-wave velocities in this modeling. This is because of the particular modeling procedure used to determine pore aspect ratios in this study. For example, P-wave velocities calculated for the patchy saturation were higher than the uniform saturation and dry pores. In the modeling to determine aspect ratios of the pores, these P-wave velocities were used as one input variable. When these P-wave velocities calculated from the self-consistent model were compared to the Backus average, the differences of P-wave velocities between them increased because P-wave velocities for patchy saturation were higher than the other fluid velocities. To make this difference meet the criterion (0.5% P-wave velocity difference, Figure 3.4), the next estimated aspect ratio value had to be smaller than the current estimated value. Therefore, calculated aspect ratios for the patchy saturation were smaller than those of the uniform saturation and dry pores. It means that the calculation of velocities and pore aspect ratios are inversely related in the self-consistent model.

#### 4.3.4.3 Relationship between parameters

To determine the pore aspect ratios, composition data and elastic moduli from the pore fluid distribution of water and gas in the rock are needed. Mineral compositions of the formation more significantly affect the elastic properties than does saturation due to the large elastic moduli values of solid minerals over the fluids. In order to accurately interpret formation characteristics for the partially saturated zone, however, the dependence of elastic data on fluid distribution needs to be fully understood as well.

In Figure 4.27, XRD composition data, estimated pore aspect ratios of patchy saturation cases by the self-consistent model, porosity, and measured P-wave velocities for the Haynesville are compared. When the components of quartz and calcite increase, pore aspect ratios also increase, and as the fraction of clay components increase, pore aspect ratios decrease in Figure 4.27. This is mainly because elastic moduli of quartz and calcite are larger than those of clay components. Figures 4.28, 4.29, and 4.30 show the relationships between seismic velocities, porosity, and determined pore aspect ratios of patchy saturation cases from the self-consistent model. Those are cross plots for measured P-wave velocities versus porosity colored by determined pore aspect ratios in Figure 4.28, determined pore aspect ratios versus porosity colored by measured P-wave velocities in Figure 4.29, and measured P-wave velocities versus determined pore aspect ratios colored by porosity in Figure 4.30, respectively. When comparing pore aspect ratios and porosity in Figures 4.27, 4.28, 4.29, and 4.30, those show that there is a direct relationship between pore aspect ratios and porosity. Typically, the larger pore aspect ratios are, the larger the porosity is. However, I observed an inverse relationship between pore aspect ratios and P-wave velocities. As pore aspect ratios and porosities increase, P-wave velocities decrease and vice versa because elastic moduli of fluids in the porosities are much smaller than those of the grains.

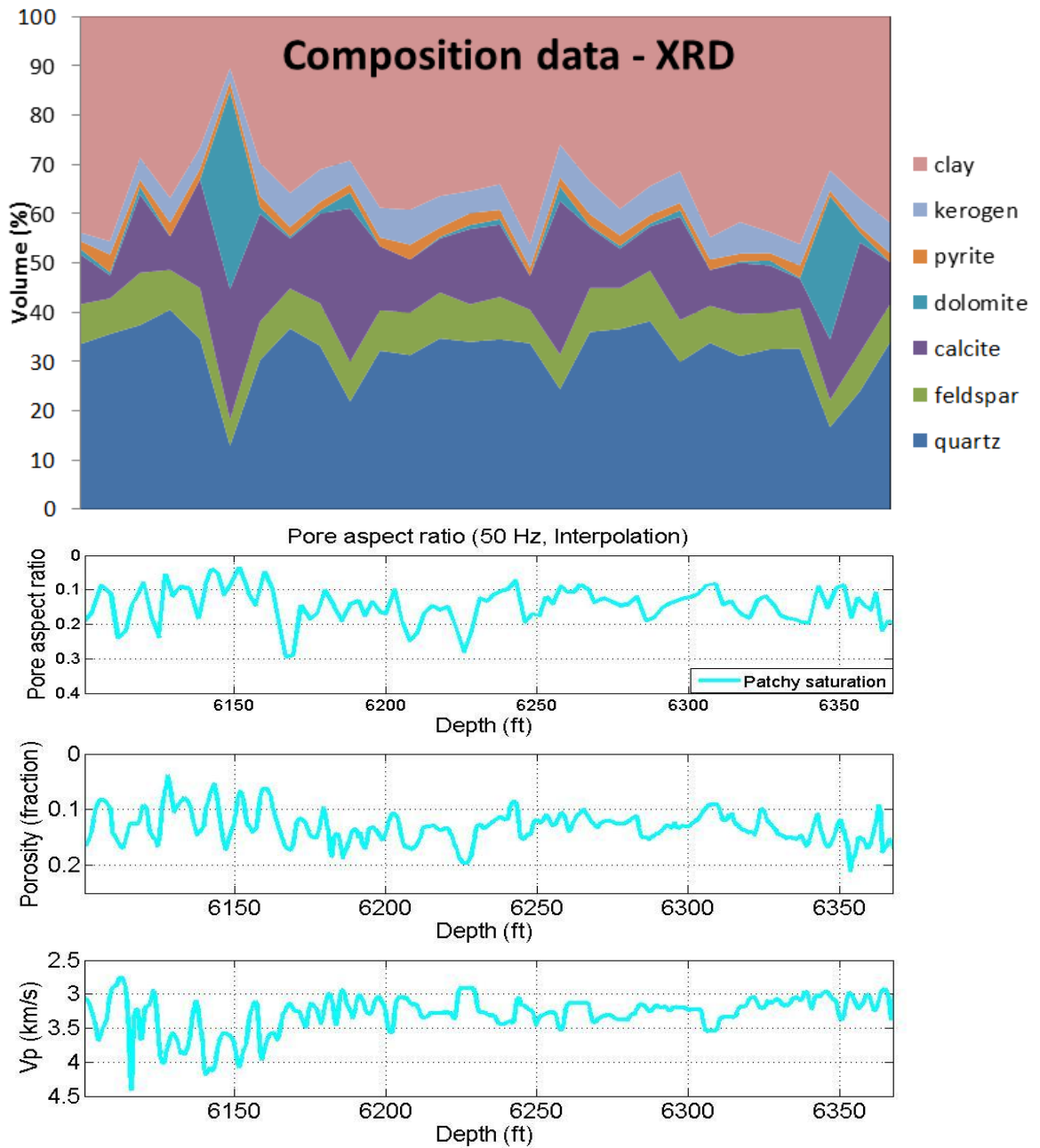


Figure 4.27: The relationship between XRD composition data, determined pore aspect ratios of the patchy saturation (SCM), porosity, and measured P-wave velocities for the Haynesville.

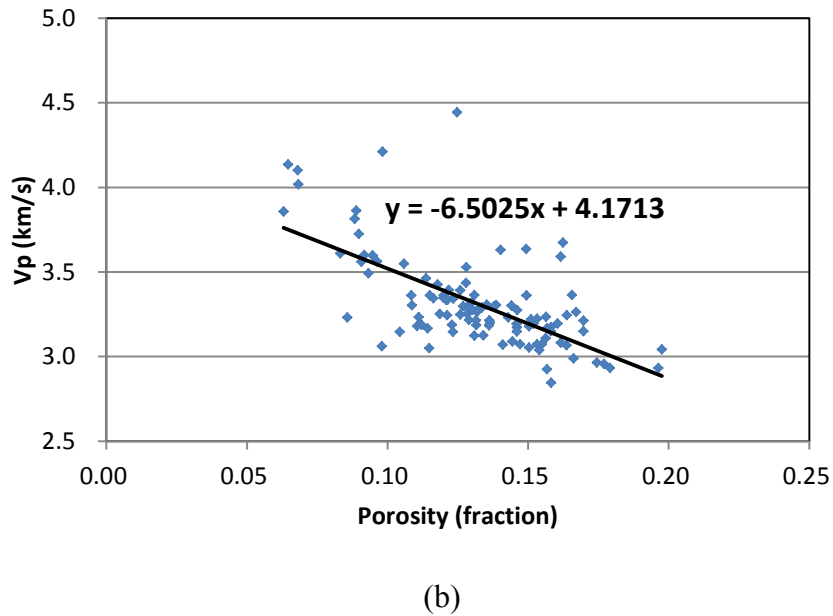
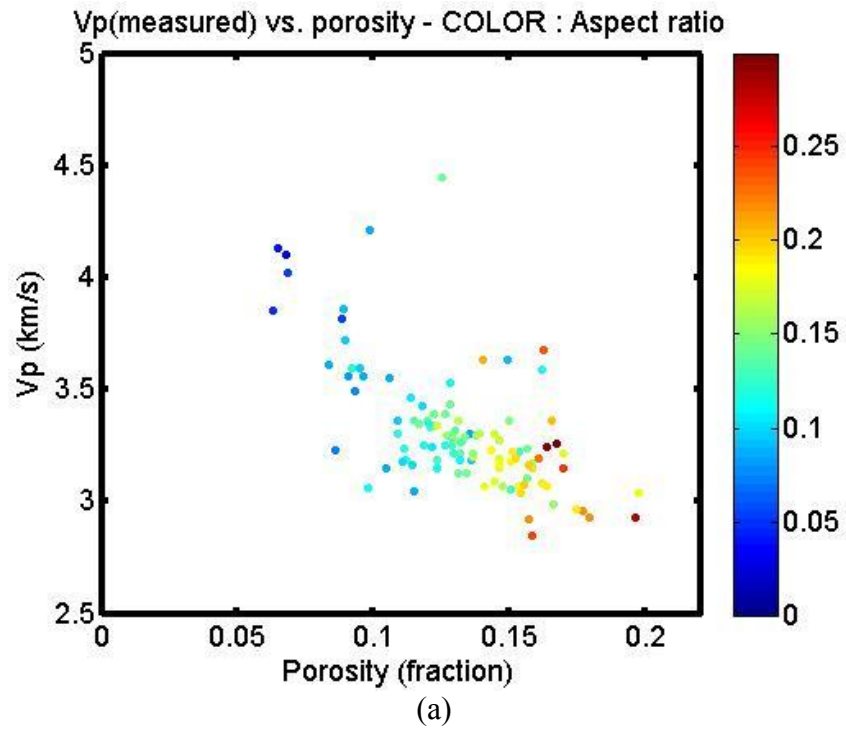


Figure 4.28: Cross plots of (a) measured P-wave velocities versus porosity colored by determined pore aspect ratios of the patchy saturation (SCM) and (b) trend line between P-wave velocity and porosity. There is an inverse relationship between P-wave velocities and porosity.

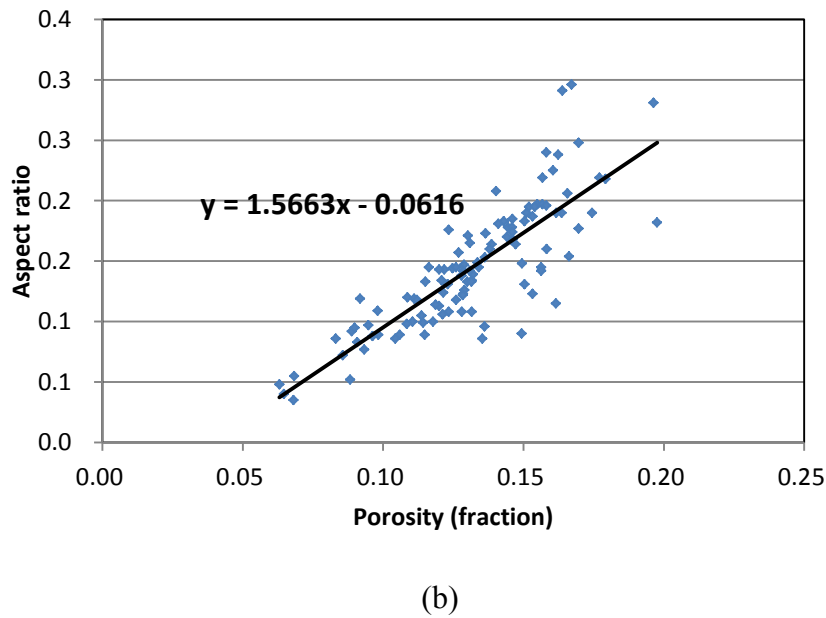
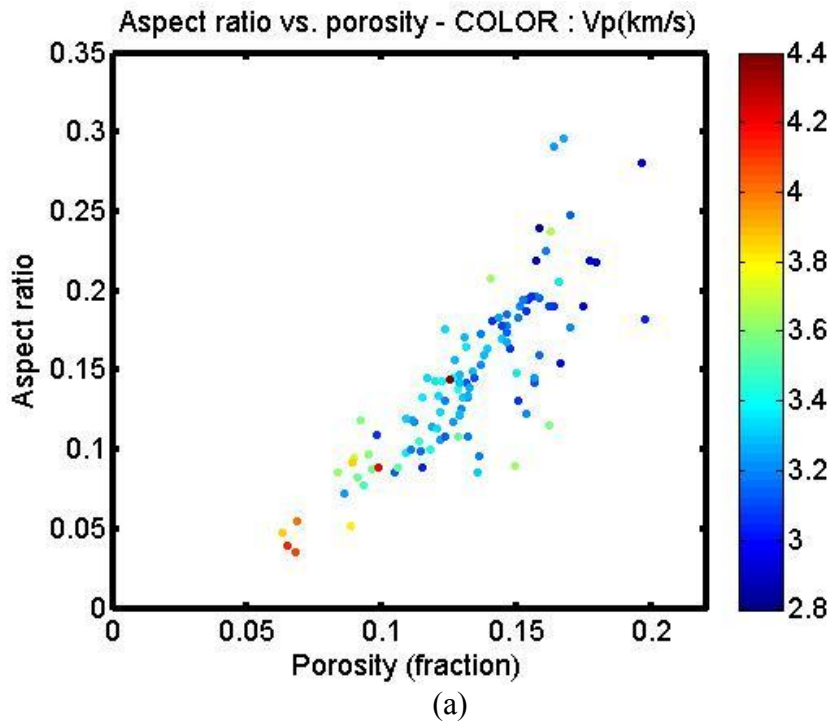
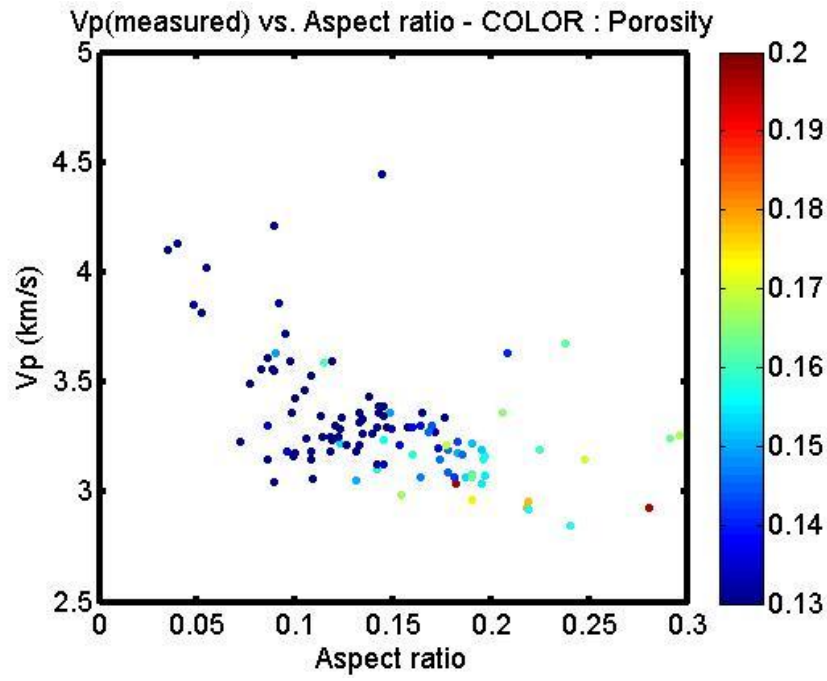
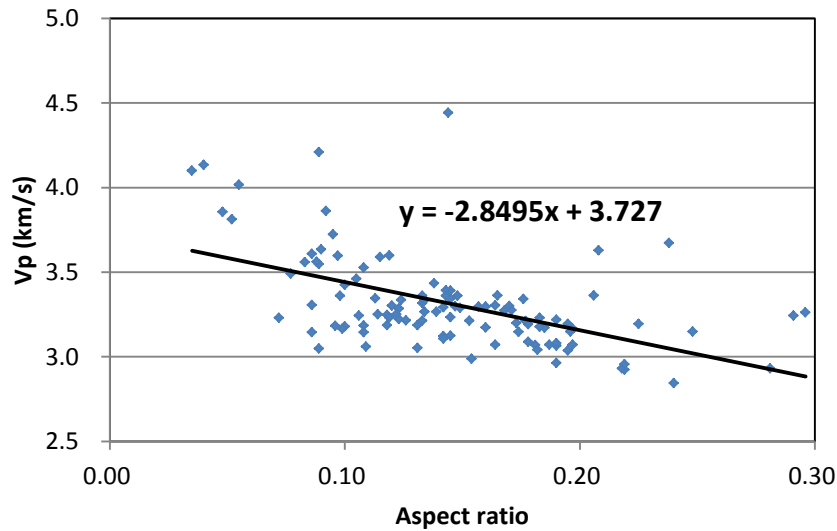


Figure 4.29: Cross plots of (a) determined pore aspect ratios of the patchy saturation (SCM) versus porosity colored by measured P-wave velocities and (b) trend line between aspect ratio and porosity. There is a direct relationship between pore aspect ratios and porosity. However, pore aspect ratio and porosity are inversely related to P-wave velocities.



(a)



(b)

Figure 4.30: Cross plots of (a) measured P-wave velocities versus determined pore aspect ratios of the patchy saturation (SCM) colored by porosity and (b) trend line between P-wave velocity and aspect ratio. There is an inverse relationship between pore aspect ratio and P-wave velocity.

#### 4.4 REFERENCES

- Adam, L., Batzle, M., and Brevik, I., 2006, Gassmann's fluid substitution and shear modulus variability in carbonates at laboratory seismic and ultrasonic frequencies, *Geophysics*, **71**, 173–183.
- Archie, G. E., 1942, The electrical resistivity log as an aid in determining some reservoir characteristics, *Petroleum Transactions of AIME*, **146**, 54–62.
- Hill, R., 1963, Elastic properties of reinforced solids: some theoretical principles. *J. Mech. Phys.Solids*, **11**, 357–372.
- Jensen, E. H., Andersen, C. F., and Johansen, T. A., 2011, Estimation of elastic moduli of mixed porous clay composites, *Geophysics*, **76**, E9-E20
- Knight, R., and Nolen-Hoeksema, R., 1990, A laboratory study of the dependence of elastic wave velocities on pore scale fluid distribution, *Geophysics*, **17**, 1529-1532.
- Knight, R., 1991, Hysteresis in the electrical resistivity of partially saturated sandstones, *Geophysics*, **56**, 2139-2147.
- Knight, R., Dvorkin, J., and Nur, A., 1998, Acoustic signatures of partial saturation, *Geophysics*, **63**, 132–138.
- Wilks, D. S., 2011, *Statistical methods in the atmospheric sciences* (3rd Edn), Elsevier Inc., Oxford, England.

## Chapter 5: Conclusion

### 5.1 SUMMARY AND CONCLUSIONS

This thesis has dealt with several practical topics to characterize reservoir properties of the Haynesville Shale. These include velocity modeling to determine pore aspect ratios and the effect of pore fluid properties on changes of P-wave and S-wave velocities. To determine pore aspect ratios, P-wave velocities were compared from the self-consistent model and observed well-log data upscaled to the seismic scale.

Velocity comparisons between the self-consistent model and Gassmann fluid substitution for dry pores, the patchy saturation and uniform saturation cases show that the scale and distribution of fluids do affect the velocities. The relationship between elastic wave velocities and water saturation in a water/gas saturated shale depends strongly on whether the saturation is heterogeneous (patchy) or homogeneous (uniform). Especially for P-wave velocities, patchy saturation cases using the self-consistent model have the largest values compared to P-wave velocities calculated from Gassmann fluid substitution. In the case of uniform saturation, the differences of P-wave and S-wave velocities between the two methods are much smaller than P-wave velocities for patchy saturation. From these comparisons, we can understand that elastic properties are strongly influenced by the fluid phase distributions in the pore space of the rock. As a result, the estimating pore shapes depends on the fluid distribution.

These comparisons also show frequency-dependent characteristics. When going from a dry- to fluid-saturated rock, the elastic bulk modulus and bulk density increase. On the other hand, the shear modulus of rock depends on the frequency-dependence of

the model used to calculate it. S-wave velocities calculated by the self-consistent model increase due to the frequency-related velocity dispersion and are different between the patchy and uniform saturation. However, S-wave velocities of the rock in Gassmann fluid substitution are the same regardless of fluid mixture for the saturated rock because Gassmann substitution assumes that the shear modulus remains unchanged between the dry rock and saturated rock. From these results, the shear moduli and S-wave velocities are sensitive to fluids at high frequencies whereas those at low frequencies are insensitive to the distribution of fluids.

Estimated pore aspect ratios for various fluid mixtures were also calculated by both the self-consistent model and Gassmann fluid substitution. Contrary to velocity comparisons, pore aspect ratios estimated for patchy saturation cases are the smallest and those for uniform saturation cases are the largest. These results are counterintuitive. These results show quite different effects of fluid property types to pore aspect ratio determination and P-wave velocity calculation. It means fluid property types affect differently the calculations for pore aspect ratios and P-wave velocities in the self-consistent model due to the modeling procedure used in this study. More specifically, the initial P-wave velocity calculation for patchy saturation was greater than the measured (observed) value. To match the computed and observed data, for patchy saturation cases to fall within the acceptance criterion (0.5% P-wave velocity difference), the next estimated aspect ratio value had to be smaller than the initially estimated value. Therefore, pore aspect ratios for the patchy saturation were smaller than those of other fluids. In addition, estimated pore aspect ratios from Gassmann substitution become large because the estimated aspect ratio is inversely related to the modeled velocity in this modeling procedure.

In the shale formation, gas originates from organic materials and migrates to the pore space. This pore space can be intergranular or within nano-scale pores within the organic materials. Clay-bound water is already present inside pores that are not in communication with one another. Because there are large differences in elastic properties between water and gas, the mixing procedure for water and gas would be considered as a patchy saturation process. In conclusion, the pore aspect ratios determined for the patchy saturation cases are the most reasonable values for the Haynesville Shale.

Pore aspect ratios estimated using the velocity modeling help us to understand elastic properties of the Haynesville Shale, which ultimately need to be linked to the geomechanical properties. The Haynesville Shale is a productive gas shale resource play that produces gas primarily through enhanced permeability resulting from hydraulic fracturing. Estimated pore aspect ratios may help to locate zones that correspond to optimal subsurface locations for fracturing the shale for gas production considering brittleness and in-situ stress of the formation. These methods could be applied to other gas shale formations where pore shape influences seismic velocities.

## **5.2 LIMITATIONS**

The approach described in this thesis has some assumptions and limitations. It was assumed that both pores and grains are idealized ellipsoidal inclusion shapes, and the model did not incorporate pressure variations. Also, the formation was treated as an isotropic elastic media. The self-consistent model does not account for compressional and shear interactions between the pores, which makes the model best suited for low

concentration of pores. As a result, P-waves were probably modeled more correctly than were S-waves. This is why only P-waves were used to estimate pore shapes.

### **5.3 POSSIBLE FUTURE WORKS**

This research could be developed for future work in the field of geomechanics related to rock physics. Analyzing whether the formation is brittle or ductile as well as in-situ stress analysis of the formation is important to better understand the reservoir characteristics of the Haynesville Shale. Typically, brittle materials accommodate strain by breaking along planes into the relatively weak direction. However, ductile materials accommodate strain plastically. Therefore, brittle formations may have a larger breaking strength than that of ductile formations, but brittle formations may stay open longer after fracturing and injecting proppants. Geomechanical properties that control brittle or ductile failure are static elastic moduli. However, elastic moduli discussed in this thesis were dynamic elastic moduli. Generally, dynamic moduli are much larger than static moduli. Dynamic bulk moduli calculated from velocities for dry rocks have approximately  $10^1$  to  $10^2$  GPa in the laboratory experiments. In contrast to that, static bulk moduli for dry rocks have about 100 MPa at 0 (zero) frequency stress. Therefore, analysis of possible relationships between static and dynamic elastic moduli is needed to link geomechanical properties to elastic properties such as pore aspect ratios determined at the seismic scale.

The correlation coefficient between two elastic moduli could be calculated for a sample rock in the laboratory. The problem is that it is difficult to apply this calculated coefficient to the other rocks as well as the overall formation because this value is likely

different from the other rocks even though the experiments were performed under the same conditions. That is because the correlation coefficient is a complex function of lithology, textures, fluids, effective stress, porosity, pore shape, and anisotropy of the formation. Understanding the effects of these rock properties on the dynamic moduli is critical if the dynamic moduli are to be quantitatively linked to the geomechanical properties. Future work should include this link to provide a more comprehensive characterization of the Haynesville Shale.

## References

- Adam, L., Batzle, M., and Brevik, I., 2006, Gassmann's fluid substitution and shear modulus variability in carbonates at laboratory seismic and ultrasonic frequencies, *Geophysics*, **71**, 173–183.
- Archie, G. E., 1942, The electrical resistivity log as an aid in determining some reservoir characteristics, *Petroleum Transactions of AIME*, **146**, 54–62.
- Avseth, P., Mukerji, T., and Mavko, G., 2005, *Quantitative seismic interpretation: applying rock physics tools to reduce interpretation risk*, Cambridge Univ. Press, Cambridge, England.
- Avseth, P., Mukerji, T., Mavko, G., and Dvorkin, J., 2010, Rock-physics diagnostics of depositional texture, diagenetic alterations, and reservoir heterogeneity in high-porosity siliciclastic sediments and rocks - A review of selected models and suggested work flows, *Geophysics*, **75**, 75A31–75A47.
- Backus, G. E., 1962, Long wave elastic anisotropy produced by horizontal layering, *Journal of Geophysical Research*, **67**, 4427-4440.
- Bayuk, I. O., Ammerman, M., and Chesnokov, E. M., 2007, Upscaling of elastic properties of anisotropic sedimentary rocks, *Geophysical Journal International*, **172**, 842-860.
- Berryman, J., 1980, Long-wavelength propagation in composite elastic media I. Spherical inclusions, *Journal of the Acoustical Society of America*, **68**, 1809-1819.
- Berryman, J. G., Berge, P. A., and Bonner, B. P., 1999, Estimating rock porosity and fluid saturation using only seismic velocities, *Stanford Exploration Project*, **102**, 143–157.
- Castagna, J. P. and Backus, M. M., 1993, *Offset dependent reflectivity – theory and practice of AVO analysis*, SEG, Investigations in Geophysics Series No. **8**, Tulsa, OK.
- Carmichael, R.S., 1989. *Practical Handbook of Physical Properties of Rocks and Minerals*, CRC Press, Boca Raton, FL.
- Curtis, M. E., Ambrose, R. J., Sondergeld, C. H., and C. S. Rai, 2010, Structural characterization of gas shales on the micro-and nano-scales: Canadian Society for Unconventional Gas/Society of Petroleum Engineers, DOI: 10.2118/137693-MS.
- Eastwood, R. L., and Hammes, U., 2011, Log model development for the Bossier and Haynesville Shales, SPWLA 52<sup>nd</sup> Annual Logging Symposium, May 14-18, 2011.
- Gassmann, F., 1951, On the elasticity of porous media, *Vier. der Natur. Gesllschft in Zurich*, **96**, 1-23.

- Goldhammer, R. K., 1998a, Second-order accommodation cycles and points of “stratigraphic turnaround”: Implications for high-resolution sequence stratigraphy and facies architecture of the Cotton Valley Lime/Haynesville of the East Texas Salt Basin (abs): AAPG 1998 Annual Convention, Salt Lake City, Utah.
- Goldhammer, R. K., and Johnson, C. A., 2001, Middle Jurassic-Upper Cretaceous paleogeographic evolution and sequence stratigraphic framework of the northwest Gulf of Mexico rim, in C. Bartolini, A. Cantu-Chapa, and R.T. Buffler, eds., The western Gulf of Mexico Basin: Tectonics, sedimentary basins and petroleum systems: AAPG Memoir **75**, p. 45-81.
- Hammes, U., Eastwood, R., Rowe, H. D., and Reed, R. M., 2009, Addressing conventional parameters in unconventional shale-gas systems: depositional environment, petrography, geochemistry, and petrophysics of the Haynesville Shale: 29th Annual GCSSEPM Foundation Bob F. Perkins Research Conference, Houston, 181–202.
- Hammes, U., Hamlin, H. S., and Ewing, T. E., 2011, Geologic analysis of the Upper Jurassic Haynesville Shale in east Texas and west Louisiana, AAPG Bulletin, **95**, 1643-1666.
- Han, D. H., Nur, A., and Morgan, D., 1986, Effects of porosity and clay content on wave velocities in sandstones, *Geophysics*, **51**, 2093-2107.
- Hill, R., 1963, Elastic properties of reinforced solids: some theoretical principles. *J. Mech. Phys.Solids*, **11**, 357–372.
- Jensen, E. H., Andersen, C. F., and Johansen, T. A., 2011, Estimation of elastic moduli of mixed porous clay composites, *Geophysics*, **76**, E9-E20.
- Jiang, M and Spikes, K., 2011, Pore-shape and composition effects on rock-physics modeling in the Haynesville Shale, SEG Expanded Abstracts 30, 2079, doi:10.1190/1.3627618.
- Knight, R., and Nolen-Hoeksema, R., 1990, A laboratory study of the dependence of elastic wave velocities on pore scale fluid distribution, *Geophysics*, **17**, 1529-1532.
- Knight, R., 1991, Hysteresis in the electrical resistivity of partially saturated sandstones, *Geophysics*, **56**, 2139-2147.
- Knight, R., Dvorkin, J., and Nur, A., 1998, Acoustic signatures of partial saturation, *Geophysics*, **63**, 132–138.
- Lindsay, R., and Koughnet, R. V., 2001, Sequential Backus Averaging: Upscaling well logs to seismic wavelengths, *The Leading Edge*, **20**, 188-191.

- Longeron, D. G., Argaud, M. J., and Feraud, J. P., 1989, Effect of overburden pressure and the nature and microscopic distribution of fluids on electrical properties of rock samples, *SPE Format. Eval.*, **4**, 194-202.
- Loucks, R. G., R.M. Reed, S.C. Ruppel, and D. Jarvie, 2009, Morphology, Genesis, and Distribution of Nanometer-Scale Pores in Siliceous Mudstones of the Mississippian Barnett Shale, *Journal of Sedimentary Research*, **79**, 848-861.
- Mavko, G., Mukerji, T. and Dvorkin, J., 2009, *The rock physics handbook (2nd Edn)*, Cambridge Univ. Press, Cambridge, England.
- Mavko, G., and Mukerji, T., 1998, Bounds on low-frequency seismic velocities in partially saturated rocks, *Geophysics*, **63**, 918-924.
- O'Connell, R. and B. Budiansky, 1974, Seismic velocities in dry and saturated crack solids: *Journal of Geophysics Research*, **79**, 5412-5426.
- Simmons, G., and Birch, F., 1963, Elastic constants of pyrite, *J. Appl. Phys.*, **34**, 2736-2738.
- Sondergeld, C. H., Ambrose, R. J., Rai, C. S., and Moncrieff, J., 2010, *Micro-Structural Studies of Gas Shales*, 2010 SPE Unconventional gas Conference, Pittsburgh, Pennsylvania.
- Sun, Y. F., 2004, Pore structure effects on elastic wave propagation in rocks: AVO modeling, *Journal of Geophysics and Engineering*, **1**, 268-276.
- Wang, F. P., and Hammes, U., 2011, Effects of petrophysical factors on Haynesville fluid flow and production, *World Oil*, **231**, pD.79-D.82.
- Wilks, D. S., 2011, *Statistical methods in the atmospheric sciences (3rd Edn)*, Elsevier Inc., Oxford, England.

## **Vita**

Kwon Taek Oh received a B.E. (Bachelor of Engineering) degree in Chemical Engineering from Chungnam National University in South Korea and had worked as a chemical engineer in the fields of LNG receiving terminal, pipeline operation, and Singapore office. He started the graduate study in Dr. Kyle Spikes's research group of The University of Texas at Austin on August 2010 and received an M.S. degree in Geological Sciences (Exploration Geophysics) on May 2012. He is now working in Korea Gas Corporation, 215 Jeongja-dong, Bundang-gu, Seongnam-si, Gyeonggi-do, South Korea (Republic of Korea), 463-754. His email address is kogasokt@gmail.com.

This thesis was typed by Kwon Taek Oh.